



# Optical measurements in disperse two-phase flows: application to rain formation in cumulus clouds

## Dissertation

zur Erlangung des akademischen Grades

**Doktoringenieur**  
**(Dr.-Ing.)**

von Dipl.-Ing. Róbert Bordás

geb. am: 27. Januar 1981

in: Miskolc, Ungarn

genehmigt durch die Fakultät für Verfahrens- und Systemtechnik  
der Otto-von-Guericke-Universität Magdeburg

Gutachter: Prof. Dr.-Ing. Dominique Thévenin

Prof. Dr.-Ing. Raymond A. Shaw

Prof. Dr.-Ing. Martin Sommerfeld

eingereicht am: 5. Juli 2011

Promotionskolloquium am: 19. Dezember 2011

---

**Abstract:** However, reliability of weather and precipitation forecasting has been significantly enhanced recently, there is still need for further improvements. In particular, rain formation in non-glaciated clouds remains a mystery. The physical process underlying collision-induced growth of rain droplets in a turbulent flow is still poorly understood.

To understand this process, experiments in wind tunnels reproducing key meteorological conditions are essential, for instance for a careful investigation of droplet-droplet interactions typical for turbulent cloud flows. Such measurements in wind tunnels are still rare in the literature.

In the present work it is detailed how cumulus clouds are modeled through their most crucial properties in a two-phase wind tunnel. Different configurations are created in order to systematically vary turbulence properties and droplet diameter distributions. It is finally shown that the crucial flow properties are in the required order of magnitude and match those of the cumulus clouds. Therefore, the investigation of droplet interactions in an environment similar to that of a cumulus cloud is possible.

Since a careful and complex experimental characterization of the air flow and the interacting water spray was necessary, the applied optical, non-intrusive measurement techniques had to be adapted or improved through modification of the evaluation software. In this way, the complete experimental characterization of the continuous and disperse phases interacting with each other has been realized. Results are freely available in a database accessible at the following link: <http://www.ovgu.de/isut/lss/metstroem>. The data may be used for validation purposes of numerical simulations.

Finally, concentrating on the growth gap associated to warm rain initiation, a method for the quantifications of droplet collision rates compared with theoretical predictions was developed. Measurements described in the present work show that the measured collision rates are higher than predicted by theory, typically by a factor of 2 to 6. These results support the idea that model modifications are needed to estimate correctly droplet collision probabilities in turbulent flows.

**Keywords:** meteorological flow, two-phase wind tunnel, cumulus cloud, droplet size distribution, droplet number density, collision rate.

---

---

**Kurzfassung:** Obwohl die Zuverlässigkeit der Wetter- und Niederschlagsvorhersage sich in letzter Zeit bemerkenswert verbessert hat, es sind noch weitere Verbesserungen notwendig. Insbesondere die Regenbildung in nicht vereisten Wolken bleibt ein Rätsel. Die physikalischen Prozesse, die dem kollisionsverursachten Wachstum von Tropfen in einer turbulenten Strömung zugrunde liegen, sind bis jetzt unzulänglich verstanden.

Um diese Vorgänge zu verstehen, sind zuverlässige Messdaten unentbehrlich. Dafür eignen sich vor allem Experimente in Windkanälen, in denen die wichtigsten meteorologischen Bedingungen reproduziert werden und somit ungeklärte Phänomene detailliert untersucht werden können, wie z.B. eine sorgfältige Untersuchung der Tropfen-Tropfen Wechselwirkungen, wie sie für turbulente Wolkenströmungen charakteristisch sind. Solche Windkanaluntersuchungen lassen sich immer noch nur sehr vereinzelt in der wissenschaftlichen Literatur finden.

In der vorliegenden Arbeit wird ausführlich darauf eingegangen, wie Kumuluswolken und ihre wesentlichsten Eigenschaften in einem Zweiphasenwindkanal modelliert werden können. Unterschiedliche Messkonfigurationen wurden aufgebaut, um die Turbulenzeigenschaften und die Tropfendurchmesser-Verteilungsfunktionen systematisch zu variieren. Darüber hinaus wird gezeigt, dass die entscheidenden Strömungseigenschaften den erforderlichen Größenordnungen der Kumuluswolken angepasst sind. Folglich sind Untersuchungen von Tropfeninteraktionen in einer den Kumuluswolken vergleichbaren Umgebung möglich.

Die sorgfältige experimentelle Untersuchung einer derart komplexen Luftströmung und des wechselwirkenden Wassersprays stellt eine außerordentliche Herausforderung an die Messmethodik dar. Insofern war es erforderlich, die verwendeten optischen, berührungslosen Messtechniken an diese Bedingungen anzupassen und zusätzlich Verbesserungen durch Änderung der Auswertesoftware vorzunehmen. Auf diese Weise konnte die komplette experimentelle Charakterisierung der aufeinander wirkenden kontinuierlichen und dispersen Phasen realisiert werden. Die Ergebnisse wurden in eine Datenbank übertragen und sind in dieser Form unter der Webadresse <http://www.ovgu.de/isut/lss/metstroem> frei verfügbar. Die Daten können unter anderem für die Validierung numerischer Simulationen verwendet werden.

Abschließend wird auf die Verständnislücke beim Tropfenwachstum verbunden mit "warmer Regenbildung" eingegangen. Dazu wird eine Messmethode, die für die Quantifizierung der Tropfenkollisionsrate geeignet ist, entwickelt, und die Ergebnisse werden mit der Theorie verglichen. Die in dieser Arbeit

beschriebenen experimentellen Ergebnisse zeigen, dass die gemessenen Kollisionsraten größer sind als die durch die Theorie a priori bestimmten, typischerweise um einen Faktor von 2 bis 6. Diese Aussage unterstützt den Gedanken, dass Modelländerungen dringend nötig sind, um Tropfenkollisionswahrscheinlichkeiten in turbulenten Strömungen fehlerfrei vorherzusagen.

**Schlüsselwörter:** Meteorologische Strömung, Zweiphasen-Windkanal, Kumuluswolke, Tropfen-Größenverteilung, Tropfen-Anzahldichte, Kollisionsrate

---

## Acknowledgments

The present work was realized at the Institute of Fluid Dynamics & Thermodynamics at the University of Magdeburg “Otto von Guericke”. I would like to express my appreciation to the major contributors.

Prof. Dominique Thévenin has supported and guided me as a supervisor throughout my PhD work. I would like to express my sincere thanks to him for his constant support. His commitment to the research will continue to motivate me in the future. Furthermore, I would like to thank Professor Raymond A. Shaw and Professor Martin Sommerfeld for accepting the examination of the thesis and also being present in the oral exam.

This work could not have been realized at all without the help of my colleagues, especially Thomas Hagemeyer, Dr. Bernd Wunderlich, Dr. Katharina Zähringer and Dr. Gábor Janiga, who provided me with numerous fruitful and very instructive discussions and invaluable contributions during my whole work. I am grateful for the time they took to provide detailed suggestions.

I am indebted to the workshop of the department, namely Peter Fischer, Christian Kisow, Eckehardt Kagelmann, Dirk Meinecke and Roland Sühning, who contributed to realize improvements and automation processes of the wind tunnel and associated measurement techniques.

An important part of this work was accomplished through discussions with our Metström project partners, Prof. Volker John and Ellen Schmeier. I am also grateful for their close cooperation during the different stages of this study. Here, I would also like to thank the useful discussions with the whole Metström research group.

Furthermore, the support of the student assistants, V. Milkevych, V. Bogatkin, J. Heßenkemper, M. Schulze and M. Zschoyan is also gratefully appreciated concerning measurements and preparing the online database.

I cannot close this section without thanking the members of my family, especially my wife Anikó, who have been providing constant support in every aspect and all the time. And finally, very special thanks to the new members of the family: to Rudolf and Roland.

This work was supported by the DFG (German Research Foundation) and was part of the priority programme SPP 1276, MetStröm.

# Nomenclature

## Latin symbols

$A$	Area	$\text{m}^2$
$C_D$	Drag coefficient	-
$c$	Speed of sound	$\text{m/s}$
$c_g$	Correction factor	-
$D$	Diffusion coefficient	$\text{m}^2/\text{s}$
$d$	Diameter	$\text{m}$
$E$	Turbulent energy spectrum	$\text{m}^2/\text{s}^2$
$e$	Vapor pressure	$\text{Pa}$
$e^*$	Saturation vapor pressure	$\text{Pa}$
$F$	Force	$\text{N}$
$f$	Frequency	$\text{Hz}$
$g$	Gravitational acceleration	$\text{m/s}^2$
$K$	Thermal conductivity	$\text{W/K m}$
$k$	Turbulent kinetic energy	$\text{m}^2/\text{s}^2$
$k_c$	Mass transfer coefficient	$\text{m/s}$
$L$	Latent heat of condensation	$\text{kJ/kg}$
$l$	Length scale	$\text{m}$
$l_k$	Burst length of class $k$	$\text{m}$
$l_r$	Residence length	$\text{m}$
$l_s$	Width of the projected slit	$\text{m}$
$M$	Mesh size of grid	$\text{m}$
$M_w$	Molecular weight of water	$\text{kg/mol}$
$m$	Mass	$\text{kg}$
$N_S$	Stokes number of the fluid oscillations	-

$N_k$	Number of drops of the diameter class $k$	-
$N_{sv}$	Number of validated signals	-
$N_\lambda$	Wave number	1/m
$n$	Droplet number density	1/m <sup>3</sup>
$p$	Pressure	Pa
$p_\lambda$	Droplet occurrence probability	-
$\dot{Q}$	Volume flow rate	m <sup>3</sup> /s
$R$	Specific gas constant	J/kg K
$\mathfrak{R}$	Gas constant	J/K mol
$S$	Supersaturation	-
$s$	Density ratio	-
$T$	Temperature	K
$t$	Time	s
$U$	Mean velocity	m/s
$u$	Instantaneous velocity	m/s
$u'$	RMS velocity	m/s
$w$	Relative velocity	m/s
$x_d$	distance downstream the grid	m

### Greek symbols

$\alpha_{j,i}$	Index of refraction	-
$\beta$	Phase angle	-
$\gamma$	Particle trajectory angle	rad
$\epsilon$	Relative signal presence	-
$\varepsilon$	Dissipation rate (of TKE)	m <sup>2</sup> /s <sup>3</sup>
$\eta$	Amplitude ratio	-
$\eta_{vi}$	Average number of drops corresponding to a given validated signal	-

---

$\theta$	Angle of incidence	°
$\theta'$	Angle of refraction	°
$\vartheta$	Temperature	°C
$\lambda$	Taylor length scale	m
$\mu$	Dynamic viscosity	Pa s
$\nu$	Kinematic viscosity	m <sup>2</sup> /s
$\rho$	Density	kg/m <sup>3</sup>
$\sigma$	Surface tension	N/m
$\sigma_s$	Signal duration	s
$\sigma_{f(x)}$	Standard deviation of the function $f(x)$	$[f(x)]$
$\tau$	Time scale	s
$\tau_i$	Residence time	s
$\phi$	Volume fraction	-
$\phi_{oa}$	Off axis angle	rad
$\varphi$	Relative humidity	-

## Indices

$a$	Air
$d$	droplet
$E$	External
$e$	Effective
$f$	Fluid
$g$	Grid
$H$	Hydraulic
$h$	Humid air
$K$	Kolmogorov
$k$	Size class
$M$	Measurement



<i>o</i>	Observation
<i>p</i>	Particle
<i>r</i>	Rod
<i>sv</i>	Validated signal
<i>T</i>	Terminal
<i>t</i>	Turbulence
<i>tk</i>	Detection volume
<i>v</i>	Vapor
<i>vort</i>	Vorticity

### Abbreviations

AMB	Acrylonitrile microbubbles	
DSD	Droplet size distribution	
EMS	Expanded microspheres	
HGB	Hollow glass bubbles	
LDV	Laser-Doppler Velocimetry	
LWC	Liquid Water Content	g/m <sup>3</sup>
PDA	Phase-Doppler Velocimetry	
PDF	Probability density function	
PEG	Fog of polyethylene glycol	
PIV	Particle Image Velocimetry	
PTV	Particle Tracking Velocimetry	
REF	Fog of vegetable oil	
TKE	Turbulent Kinetic Energy	m <sup>2</sup> /s <sup>2</sup>
WDR	Water droplets	

### Non-dimensional numbers

Fr	Froude number	-
Re	Reynolds number	-

Sc	Schmidt number	-
Sh	Sherwood number	-
St	Strouhal number	-
Stk	Stokes number	-
We	Weber number	-



# Contents

<b>Nomenclature</b>	<b>v</b>
<b>Contents</b>	<b>xi</b>
<b>1 Introduction</b>	<b>1</b>
1.1 Rain formation . . . . .	1
1.1.1 Warm rain initiation . . . . .	4
1.2 Two-phase wind tunnels: state of the art . . . . .	5
1.3 Properties of humid air . . . . .	9
1.3.1 Viscosity . . . . .	9
1.3.2 Density . . . . .	10
1.3.3 Vapor pressure . . . . .	10
1.3.4 Relative humidity . . . . .	11
1.3.5 Condensational droplet growth . . . . .	11
1.4 Theory of droplet collisions . . . . .	13
1.5 Conclusions and summary of goals . . . . .	18
<b>2 Fundamental considerations concerning optical flow measurements and tracers</b>	<b>21</b>
2.1 Problem of light refraction . . . . .	21
2.1.1 Refraction index matching . . . . .	23
2.1.2 Image correction . . . . .	24
2.2 Tracer particles for fluid measurement . . . . .	25
2.2.1 Flow response . . . . .	25
2.2.2 Equation of motion for spherical particles . . . . .	30
2.2.3 Computational comparison . . . . .	36
<b>3 Experimental setup</b>	<b>41</b>
3.1 Two-phase wind tunnel . . . . .	41
3.1.1 Injection system . . . . .	42
3.1.2 Control system . . . . .	46
3.2 Generation of controlled structures and turbulence properties . . . . .	49
3.2.1 Configuration <b>M1</b> – Without turbulence modification . . . . .	50
3.2.2 Configuration <b>M2</b> – Passive grid . . . . .	52
3.2.3 Configuration <b>M3</b> – Bluff body . . . . .	59
3.2.4 Configuration <b>M4</b> – Double injection . . . . .	61
3.3 Measurement techniques . . . . .	62

3.3.1	LDV/PDA system for velocity and droplet diameter measurements . . . . .	62
3.3.2	PIV system for velocity field measurements of both phases . . . . .	66
3.3.3	Shadowgraphy system for the detection of droplet collision rates . . . . .	69
<b>4</b>	<b>Specific adaption of measurement methods</b>	<b>73</b>
4.1	Laser-Doppler methods . . . . .	73
4.1.1	Laser-Doppler Velocimetry . . . . .	73
4.1.2	Phase-Doppler Velocimetry . . . . .	79
4.2	Imaging methods . . . . .	83
4.2.1	Shadowgraphy . . . . .	83
4.2.2	Particle Image Velocimetry . . . . .	85
<b>5</b>	<b>Experimental results and analysis</b>	<b>91</b>
5.1	Measurement uncertainty and repeatability . . . . .	91
5.1.1	Measurement uncertainty of LDV/PDA . . . . .	91
5.1.2	Measurement repeatability of LDV/PDA . . . . .	92
5.2	Measurements of the continuous (air) phase . . . . .	93
5.2.1	Velocity measurements . . . . .	94
5.2.2	Derived values . . . . .	95
5.3	Measurements of the disperse (droplet) phase . . . . .	100
5.3.1	Velocity and diameter measurements . . . . .	101
5.3.2	Derived values . . . . .	102
5.4	Consequences for rain formation in clouds . . . . .	108
5.4.1	Reproducing cloud turbulence at small scales . . . . .	109
5.4.2	Passive grid . . . . .	110
5.4.3	Bluff body . . . . .	110
5.4.4	Conclusions . . . . .	110
5.5	Online experimental database . . . . .	112
5.6	Companion numerical simulations . . . . .	114
5.6.1	Numerical models . . . . .	114
5.6.2	Numerical results . . . . .	117
<b>6</b>	<b>Conclusions and outlook</b>	<b>119</b>
6.1	Conclusions . . . . .	119
6.2	Outlook . . . . .	121
<b>A</b>	<b>Wind tunnel specifications</b>	<b>123</b>
<b>B</b>	<b>Selected experimental results, Configuration M1</b>	<b>127</b>

<b>Contents</b>	<b>xiii</b>
<b>C Selected experimental results, Configuration M2</b>	<b>129</b>
<b>D Selected experimental results, Configuration M3</b>	<b>131</b>
<b>E Selected experimental results, Configuration M4</b>	<b>133</b>
<b>List of Figures</b>	<b>135</b>
<b>List of Tables</b>	<b>141</b>
<b>Bibliography</b>	<b>143</b>



# Introduction

## 1.1 Rain formation

The mechanism of rain formation remained a great mystery for a long time. Insufficient knowledge about rain formation, dangers due to drought and the need for rain at specific moments related rain primarily to religion (rain-gods, thunder-gods or the rain dances of the Native Americans: Fig. 1.1).

Understanding the mechanism of rain formation led to the capability of weather prediction. Weather forecasting is based on the diagnosis of three-dimensional atmospheric conditions in a given time instance, relying on geographical properties and other additional information such as radar or satellite data. Different meteorological models are available with an input from the observation stations (e.g., temperature, humidity).

Weather forecasting can be defined as a prediction of 3D flow and thermodynamic fields. It is particularly important that the applied procedures use adequate boundary conditions, include all relevant physical models and correctly describe real physics. However, reliability of weather and precipitation forecasting has been significantly enhanced recently, there is still need for further developments (Kisi and Shiri, 2011). The main problem is the droplet growth time in non-glaciated clouds. That is why the deviation between predicted and observed duration of cloud droplet growth (factor of 2 or more under certain circumstances (Xue et al., 2008)) is investigated. In this work the discussed discrepancy will be explained to improve existing models.



**Figure 1.1:** The rain dance is out of date...<sup>1</sup>

<sup>1</sup>Image from <http://de.toonpool.com>



The invention of the meteorological radar techniques made a contribution to the scientific explanation for different stages of rain formation (Fig. 1.2). Formation of cloud droplets occurs on micrometer to millimeter scales. Now, it is well known that on the surface of natural water storage (mostly in oceans: 97% of Earth's water) liquid water evaporates due to the heating effect of the sun. Then the humid air rises upwards, until the wind takes it over the land. Warm updrafts coming from the heated land surface take water vapor even higher, where the air is colder (temperature decrease of  $\sim 1$  K/100 m).

Cloud droplets of radii less than  $10\ \mu\text{m}$  grow efficiently through diffusion of water vapor (Kogan, 1993). When the temperature of water vapor decreases (actual vapor pressure = saturation vapor pressure), it condensates on solid particles (dust, salt or pollution particles) and water droplets come into existence (first with a size  $< 10\ \mu\text{m}$ ). These droplets act as water traps, and form cloud drops (up to  $20\ \mu\text{m}$  in size) by collecting water. These droplets are still too small to fall as precipitation, because their fall speed is not large enough to overcome updrafts.

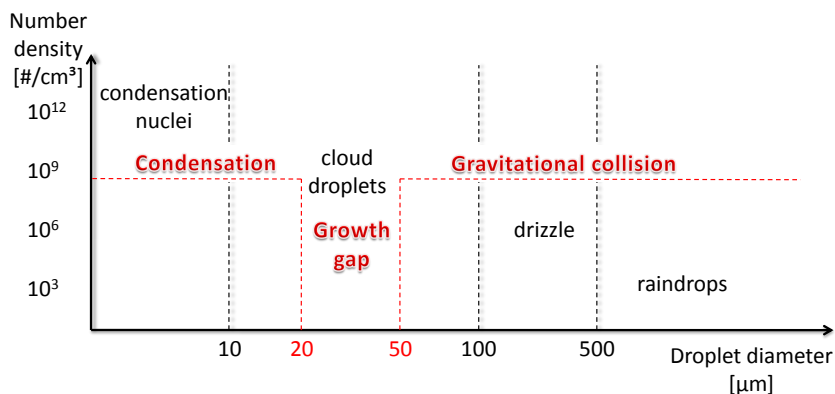


**Figure 1.2:** Typical number density values belonging to different droplet sizes and the **dominating processes** of cloud droplet size development.

Water droplets, in addition to the condensation of water vapor, grow also when particles collide, which gets significant for droplets  $> 20\ \mu\text{m}$  (Fig. 1.2). Droplets larger than  $50\ \mu\text{m}$  grow efficiently through gravitational collisions (Langmuir, 1948). If enough collisions occur to produce a droplet with a fall velocity exceeding the cloud updraft speed (approximately associated with a size  $> 500\ \mu\text{m}$ ), it will fall out of the cloud as precipitation. In the end, falling droplets return into the ocean. From there it will again continue its cycle (see Fig. 1.3) into and then out of the clouds.

Summarizing, there are two decisive causes for droplet growth (see also Fig. 1.4):

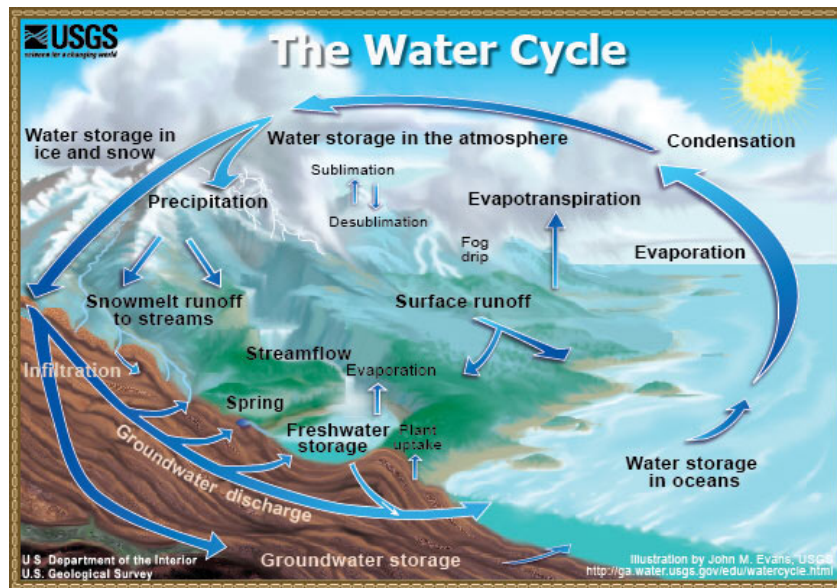


**Figure 1.3:** Water cycle. Image from the U.S. Geological Survey's (USGS) <http://ga.water.usgs.gov/edu>.

1. condensation for smaller droplets
2. collision and coalescence for larger drops (Shaw, 2003).

Condensation takes a relatively long time, and is irrelevant for the later investigations in our wind tunnel.

Droplets larger than approximately  $25 \mu\text{m}$  grow by collision-/-coalescence at a much shorter time scale than by condensation (Fig. 1.4) and can be enhanced by turbulence-particle interactions. This sudden increase in size is further accelerated when the droplets

- have a broad size distribution,
- are large enough to be noticeably influenced by gravity (typically  $> 50 \mu\text{m}$ ).

This regime between a droplet size of  $20$  and of  $50 \mu\text{m}$  in warm rain initiation is also called the growth gap, where droplet size distribution (DSD) and turbulence have a noticeable influence on droplet size development. This is the most complex region. Therefore, it is of central importance in this thesis.

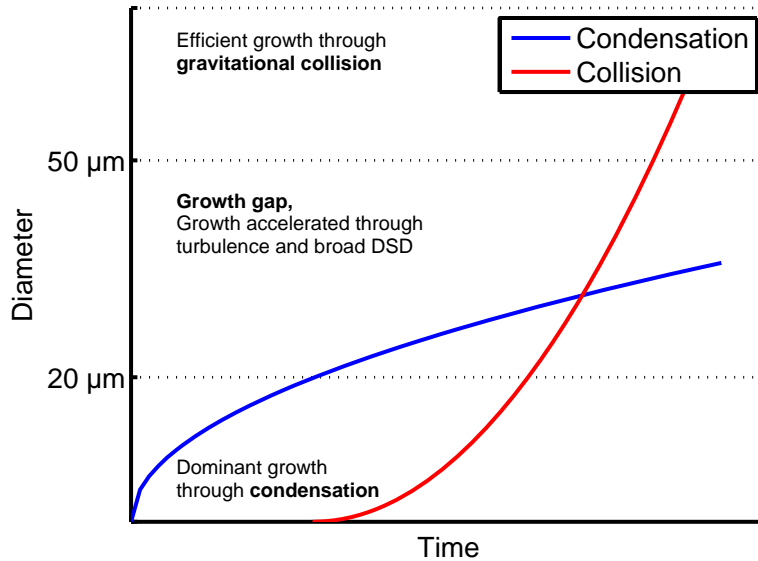


**Figure 1.4:** Schematic curves of droplet growth time. Regions with dominant mechanisms are also indicated.

### 1.1.1 Warm rain initiation

The mechanism of warm (i.e., ice free) rain initiation in cumulus clouds is a very important and one of the unsolved problems of cloud physics (Xue et al., 2008; Wang and Grabowski, 2009; Khain, 2009). It is associated with the so-called growth gap between the condensational growth of the small droplets and gravity driven collisional growth of larger droplets. To overcome the gap in the theory between the growth of smaller and larger droplets (20...50  $\mu\text{m}$ ) discussed in this section, the effects of turbulence on warm rain initiation should be considered. De Almeida (1979) found that collision efficiency for smaller cloud droplets may be significantly increased by the small-scale turbulent motions. Pinsky et al. (1999) concluded that coalescence starts being effective even at a drop diameter of 30  $\mu\text{m}$ . Another aspect that has not yet been satisfactorily explained by theory is the presence of the broad droplet spectra in cumulus clouds (Warner, 1969). The theory of the broadening of cloud droplet spectra was reviewed by Beard and Ochs III (1993), who concluded that the process of warm rain initiation due to turbulence remains largely unanswered:

- the time scale for collision-coalescence is much shorter than that of condensation and

- it is generally accepted that condensation by itself is unable to produce such large droplets that can fall as rain (Johnson, 1993).

There is a lack of agreement between theory and experiments (Shaw et al., 1998) and experiments show that the droplet spectra is broader than it would be predicted by theory. Further on, there appears to be a factor of 2 or more difference between the predicted growth time of cloud droplets and the observed growth time (Xue et al., 2008). This problem is assumed to be related to the growth gap in the droplet size range of 20 – 50  $\mu\text{m}$ , separating the two main processes of droplet growth. In this region not only the broad droplet spectra but even turbulence by itself enhances growth rates. Pinsky and Khain (1996, 1997) showed that preferential concentration significantly increases the collision–coalescence rate and possibly increases the collection (coalescence) efficiency of smaller drops. Pinsky et al. (2008) showed that an increase in the collision rate between cloud droplets may serve as a triggering mechanism for raindrop formation. In this work tables for collision efficiencies are also presented, with the hint of the authors that the turbulent effect on drop collision is probably underestimated. This corroborates the statement of Xue et al. (2008). Therefore, systematic and reproducible experimental investigation of droplet–droplet interactions in turbulent flows is necessary. The most suitable way to carry out such measurements is to apply a two–phase wind tunnel with flow conditions similar to that of clouds.

## 1.2 Two-phase wind tunnels: state of the art

In the following, a literature overview is presented, where two–phase wind tunnels have been used for cloud physics investigations.

In Fessler et al. (1994) the distributions of solid particles are investigated in a turbulent channel flow. This is particularly important for the investigation of atmospheric pollutant transport. The particle concentration is measured by means of an imaging method with laser illumination and individual particle identification. Several hints are given about the preferential concentration of particles larger than the viscous length scales of the flow. The Reynolds number in the channel of 40 mm width and with an aspect ratio of 11.4 is  $\text{Re} = 13\,800$ , based on the half width of the channel and on the mean velocity (10.5 m/s).

Korczyk et al. (2006) attempted to quantify the influence of turbulence in an unsaturated air/water-mixture using Particle–Image Velocimetry (PIV). Water mist of drop diameters below 10  $\mu\text{m}$  is generated in a chamber of

$1 \times 1 \times 1.8 \text{ m}^3$ , where the liquid water content (LWC) is found to be  $20 \text{ g/kg}$ . During these PIV measurements only the properties of the disperse phase has been measured, the continuous phase has not been considered.

Probably the first wind tunnel for cloud physics research has been established at the Swiss Federal Institute for Snow and Avalanche Research (List, 1959). It is a vertical wind tunnel used to study suspended particles. The velocity can be varied up to  $25 \text{ m/s}$ , and water droplets can be generated between 1 and  $200 \text{ }\mu\text{m}$ . LWC can be set up to  $10 \text{ g/m}^3$  and the temperature down to  $-40^\circ\text{C}$ . Experiments conducted in this facility are mainly dedicated to the growth of ice particles as relevant to environmental conditions.

The UCLA wind tunnel (Pruppacher and Neiburger, 1968) is probably the most well-known wind tunnel specifically employed for cloud physics research. Within this wind tunnel, it is possible to suspend water droplets for a long time. Many investigations have been carried out with this setup: water droplets falling at terminal velocity, drag measurements as a function of the Reynolds number (Beard and Pruppacher, 1969), internal circulation and shape of falling droplets (Pruppacher and Beard, 1970) and evaporation rate (Beard and Pruppacher, 1971). In this installation, the air humidity can be varied from 0% up to saturation and droplets have been investigated with a diameter from 20 to  $900 \text{ }\mu\text{m}$ . During the experiments the air can also be temperature-controlled within a relatively broad region. Using this setup it is possible to deliver first-class information for a variety of meteorological processes. However, all the employed measurement methods at that time have been intrusive, possibly impacting flow behavior. The interaction between droplet behavior and turbulent flow is not investigated systematically. As a consequence, these seminal measurements do not really allow a validation of today's numerical models and simulations.

The I.C.E. wind tunnel (Gabriels et al., 1997) in Belgium is a closed circuit, low-speed wind tunnel. Different velocities can be adjusted by changing the pitch angle of 16 adjustable blades, while the fan is constantly driven by a  $150 \text{ kW}$  electric motor. The measurement section is  $12 \text{ m}$  long,  $1.2 \text{ m}$  wide and the height can be varied from  $1.8 \dots 3.2 \text{ m}$ . The effect of simulated rainfall, soil erosion and transport processes in wind-driven rain was studied by Erpul et al. (1998, 2002, 2004, 2005). The investigated rain drop size is in the range of  $0.2 \dots 3 \text{ mm}$ . The wind speeds are set in the region of  $0 \dots 15 \text{ m/s}$  and measured in the center of the wind tunnel by means of a vane-type anemometer. The nozzles are placed on the top of the tunnel and inject water droplets downwards. The experiments in this wind tunnel do not specifically

consider rain initiation. The employed droplets are too large and hence outside the relevant range for rain initiation.

In the DeFrees Hydraulics Laboratory at Cornell University a tilting wind–water tunnel with a test–section of  $20 \times 1 \times 0.9$  m is applied for air–water interface experiments. Here, Lagrangian particle acceleration measurements in active grid–generated turbulence (Ayyalasomayajula et al., 2006) are carried out and spatial particle clustering at high Re–numbers is experimentally investigated (Saw et al., 2008) by means of a Phase–Doppler Anemometry (PDA) system. Dilute water droplets with a Stokes number of approximately 0.1 are generated by means of several water spray injectors, downstream of the active grid. These experiments are very important for an initial understanding of droplet evolution controlled by cloud turbulence. However, only a single set of conditions has been considered, highlighting the need for systematic parameter variations.

For the issues considered in the present work the measurements presented by Vohl et al. (1999) are also particularly interesting. Collision and coalescence processes of droplets have been investigated in the vertical wind tunnel of Mainz (an improved model of the UCLA tunnel in Los Angeles) both for laminar and turbulent flows. In this study, the global properties of turbulence and droplets are examined. It is established that there is a tendency toward faster droplet growth under turbulent conditions. A good agreement is found, compared to theoretical calculations using collision efficiencies, in the literature. As a consequence, these measurements cannot explain the discrepancies found between theory and observations concerning warm rain initiation. This might be due to the fact that the flow velocity is only measured at selected locations and using hot wire anemometry, an intrusive technique difficult to employ with a high accuracy in two–phase flows. The authors of this work underline in the conclusions that further, systematic wind tunnel experiments are clearly required.

In the recent times, numerical simulations for meteorological problems (Seifert, 2008; Woittiez et al., 2009; Stevens and Seifert, 2008) including relevant theoretical models (Seifert and Stevens, 2010), become increasingly essential and play already an enormous role in weather forecasting. Such numerical simulations can deliver proper predictions only when the boundary conditions of the system are known in space and time; when the accuracy of the numerical procedure is sufficient; and if all relevant physical models are implemented and describe correctly real physics.

**Table 1.1:** Summary of the wind tunnels described in the present section, including the wind tunnel of the University of Magdeburg, described later in Chapter 3.

Wind tunnel location	Velocity [m/s]	Investigated diameters [μm]	Orientation of the test-section	Main research area
SFI/ISAR <sup>a</sup>	up to 25	1 ... 200	horizontal	growth of ice particles
UCLA <sup>b</sup>	levitation at terminal velocities	20 ... 900	vertical	cloud physics
I.C.E. <sup>c</sup>	0 ... 15	200 ... 3 000	horizontal	<ul style="list-style-type: none"> <li>• rainfall,</li> <li>• soil erosion,</li> <li>• transport processes</li> </ul>
DeFrees <sup>d</sup>	up to 15	up to 100	horizontal	<ul style="list-style-type: none"> <li>• air-water interface,</li> <li>• droplet growth controlled by turbulence</li> </ul>
Mainz <sup>e</sup>	levitation at terminal velocities	60 ... 1 000	vertical	droplet growth at turbulent conditions
Magdeburg <sup>f</sup>	0.3 ... 50	up to 170	horizontal	cloud physics

<sup>a</sup>Swiss Federal Institute (WSL) Institute for Snow and Avalanche Research (SLF)

<sup>b</sup>University of California, Los Angeles

<sup>c</sup>University of Ghent, Belgium

<sup>d</sup>DeFrees Hydraulics Laboratory, Cornell University

<sup>e</sup>Institute for Atmospheric Physics, University Mainz

<sup>f</sup>Laboratory of Fluid Dynamics & Technical Flows, University of Magdeburg “Otto von Guericke”

The boundary conditions should be experimentally determined to generate conditions according to reality. For experimental investigations, there is a possibility to carry out airborne measurements (Glantz et al., 2003; Fugal et al., 2004; Siebert et al., 2006, 2007), but it should be noted that they are limited by lack of control over boundary conditions and reproducibility. Ground-based measurements (Paluch et al., 1996; Calbó and Sabburg, 2008) are good alternatives to avoid intrusion into the cloud and its environment, but the large distances do not allow an investigation with an appropriate resolution of all turbulent scales. The complementary use of both methods (Protat et al., 2009) is also possible, but highly complex and costly. Though there are numerous promising calculations in the literature (Grabowski, 2001; Siebesma et al., 2003; Fan et al., 2007), there is a lack of experimental validation data. Warhaft (2009) reviewed the recent developments in the study of droplet motion in turbulent flows, and pointed out that there are several key questions in this field, which constitute the main experimental challenges in this work as well:

- a) “The particle concentrations need to be systematically varied so that collisions can be introduced into the experiments”;
- b) “Experiments in inhomogeneous flows are also needed. We have no evidence of how the inertial particle acceleration PDF and the radial distribution vary in inhomogeneous flows”;
- c) “Classical theory is unable to explain the rapid rain initiation time observed in clouds”.

Using controlled experiments in a two-phase wind tunnel, we will try to contribute to all of these open questions with useful information. In order to carry out meaningful experiments, several basic concepts of meteorology are needed. The next section summarizes first the most important properties of humid air.

## 1.3 Properties of humid air

### 1.3.1 Viscosity

The viscosity of suspensions has been predicted by Einstein (Landau and Lifschitz, 1966) for the case of spherical particles. If the dimensions of the particles involved are small compared with the characteristic length of the fluid flow, the suspension may be regarded as a homogeneous medium and



its effective viscosity  $\nu_e$ , which is different from the viscosity  $\nu$  of the original fluid, is given by

$$\nu_e = \nu(1 + 2.5\phi), \quad (1.1)$$

In clouds,  $\phi$  can be given by the ratio of the liquid water content (LWC) to the particle density  $\rho_p$ ; thus Einstein's effective viscosity can be written as

$$\nu_e = \nu \left( 1 + 2.5 \frac{\text{LWC}}{\rho_p} \right), \quad (1.2)$$

according to [De Almeida \(1979\)](#). Since the value of water volume fraction  $\phi$  in clouds is about  $10^{-6}$ , the correction for the effective viscosity is very small and the added mechanism of energy dissipation is negligible. In further calculations the viscosity of air will hence be directly used.

### 1.3.2 Density

The density of the flow medium is a fundamental property for further calculations, as it is a required input parameter for e.g., the calculation of the equation of motion or the velocity calculation in the wind tunnel. An accurate determination of the density of the air in the wind tunnel requires the consideration of the humidity, as the specific gas constant is influenced by the latter. After adapting the specific gas constant, the equation

$$\rho = \frac{p}{R_h T} \quad (1.3)$$

is used further. The specific gas constant of humid air can be calculated by the following equation:

$$R_h = \frac{R_a}{(1 - \varphi \frac{e^*}{p})(1 - \frac{R_a}{R_v})}, \quad (1.4)$$

where  $R_a = 287.1 \text{ J/kg K}$  is the specific gas constant of dry air,  $R_v = 461.5 \text{ J/kg K}$  is the specific gas constant of vapor,  $e^*$  is the saturation vapor pressure of water in air empirically calculated with the help of the Magnus formula, Eq. (1.6).

### 1.3.3 Vapor pressure

Vapor pressure  $e_v$  is the partial pressure of the water vapor. In the atmosphere, the range for  $e_v$  is from slightly over 0 up to approximately 40 hPa ([Kraus](#),

2004). As the concentration of water vapor is quite low, it can be handled as an ideal gas:

$$e_v = \rho_v R_v T, \quad (1.5)$$

where  $R_v = \frac{R}{M_v} = 461.5 \text{ J/kg K}$ , with  $R = 8.314472 \text{ J/mol K}$  (Mohr et al., 2008) and  $M_v = 18.016 \cdot 10^{-3} \text{ kg/mol}$ . The vapor pressure cannot exceed the saturation vapor pressure  $e^*$ , which can be expressed as a function of temperature.

To compute the saturation vapor pressure, the empirical formula of Magnus was retained:

$$e^* = 6.1078 \exp\left(\frac{17.08085\vartheta}{234.175 + \vartheta}\right) \text{ hPa}, \quad (1.6)$$

which is simpler than that of the World Meteorological Organization (Goff and Gratch, 1946), internationally accepted in 1947. Since the deviation is minimal in the region relevant for meteorological experiments (max. 0.22% for 0 – 100°C, compared to the values of a saturated vapor table), Eq. (1.6) is applied for all calculations in the following.

### 1.3.4 Relative humidity

This is a relative quantity, defined as the ratio of the actual vapor pressure  $e_v$  to the saturation vapor pressure of water  $e_w^*$  at the ambient air temperature  $T_a$ :

$$\varphi = \frac{e_v}{e_w^*(T_a)}. \quad (1.7)$$

Thus,  $\varphi$  is not an absolute measure for the water vapor content but it measures the degree of saturation. Airplane experiments showed that in most cases the relative humidity in clouds is between 95 and 100% (Pruppacher and Klett, 1997), though the lower end of the range can be sometimes as low as 81%. Warner (1969) showed as well that the observed range in small to moderate cumuli is rarely outside 98 – 102%.

### 1.3.5 Condensational droplet growth

Condensation is the change from the gaseous phase of an element (here: water vapor) into liquid droplets of the same element. Since the condensing water molecules suffer from reduced degrees of freedom and ranges of motion, their prior kinetic energy must be lost or transferred to adsorbing colder water molecules or centers of condensation within the gas volume. Under realistic atmospheric conditions, condensation takes place on preexisting, soluble

aerosol particles. Absorption into the surface of a liquid is reversible, like evaporation (McNaught and Wilkinson, 1997). Condensation commonly occurs when a vapor is cooled to its saturation limit and when the molecular density in the gas phase reaches its maximal threshold.

To quantify condensation and express the results in terms of droplet growth, the mass transfer between water vapor and water droplets should be characterized. This can be deduced from Fick's law, as described in Pruppacher and Klett (1997):

$$\frac{dm}{dt} = \frac{2\pi d D_v M_w}{\Re} \left( \frac{e_\infty}{T_\infty} - \frac{e_a}{T_a} \right). \quad (1.8)$$

Since it is not the temperature of the droplets that is directly measured, but the relative humidity of the flow in the wind tunnel, the above equation can be expressed in terms of the supersaturation (Fukuta and Walter, 1970):

$$\frac{dm}{dt} = \frac{2\pi d(S-1)}{\frac{L_v^2 M_w}{K_a \Re T_\infty^2} + \frac{\Re T_\infty}{D_v M_w p_{\infty, sat}}}, \quad (1.9)$$

where  $S = p_\infty/p_{\infty, sat}$  is the saturation ratio. The differential equation is solved with the help of a Matlab<sup>®</sup> script and the diameter vs. time diagram is presented in Fig. 1.5, for  $d_0 = 12.5 \mu\text{m}$  and 1% supersaturation ( $S = 1.01$ ), which is obviously an overestimation. The resulting volume increase of 8% over 400 mm of the wind measurement section (axial length) corresponds to the one found also in Celani et al. (2005).

However, the droplets considered by Celani et al. (2005) do not move. That is why the equations are extended following Tokar' et al. (1981), where the mass transfer coefficient is corrected. Thus, the influence of the relative velocity between the continuous and disperse phase is taken into account and the corrected mass transfer coefficient is calculated by means of the Sherwood number:

$$k_c = \frac{\text{Sh } D_v}{d}, \quad (1.10)$$

where the Sherwood number itself can be calculated from the Schmidt and Reynolds numbers:

$$\text{Sh} = 2 + 0.6\text{Re}^{1/2}\text{Sc}^{1/3} \quad (1.11)$$

The difference in volume increase between stationary and moving droplets is visible in Fig. 1.5. Result of the calculations shows that after 0.133 s, which is necessary for a droplet with a velocity of 3 m/s to transit through the measurement section of the wind tunnel (400 mm) the mass or volume increase of a droplet is around 7%. It will be shown later in Chapter 5 that the

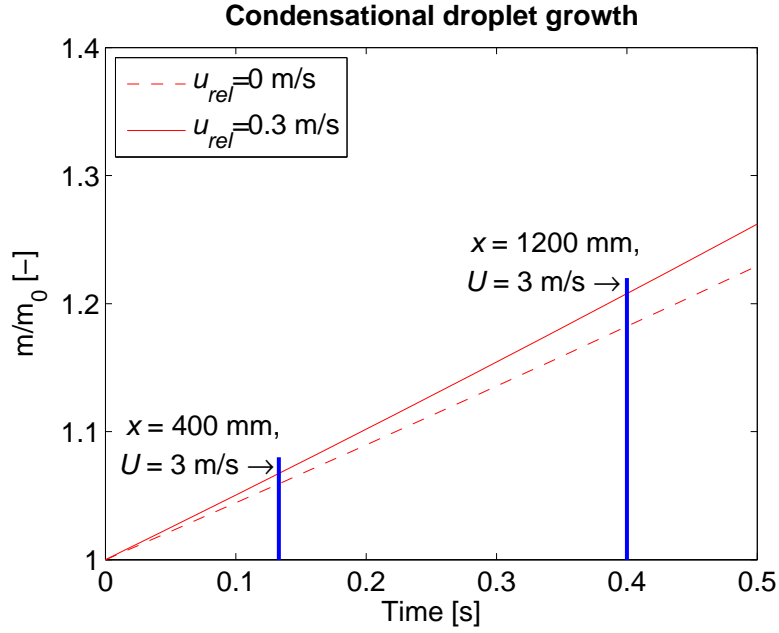


**Figure 1.5:** Condensational water droplet volume growth with  $S = 101\%$  and  $d_0 = 12.5 \mu\text{m}$ .

droplet volume increase in the test section is around 60%, thus confirming that growth through condensation is not the dominant mechanism in the present measurement configuration, as expected.

The following section deals with the calculation of theoretical droplet collision rates, since one of the main objectives of this thesis is the experimental investigation of droplet collision rates in turbulent flows.

## 1.4 Theory of droplet collisions

In order to compare experimental collision rates to theoretical ones, the most suitable approach will be selected in this section after an overview about the collision theory of small droplets in turbulent flows.

In the article of [Kruis and Kusters \(1997\)](#) an overview is presented about the development of collision theory in turbulent flows. Limits of the theoretical approaches are discussed and a general derivation is given, containing the inertia of particles and the density differences between continuous and disperse phases. A universal solution for the relative velocity of two particles caused by the turbulent acceleration is also introduced. [Camp and Stein \(1943\)](#) were the first, who applied the concept of the simple shear flow ([von Smoluchowski](#),

1917) from the turbulent coagulation process to this problem. They argued that the shear field causes a relative motion between the particles leading to collisions. In the article of [Saffman and Turner \(1956\)](#) the collision theory is presented for small particles in a turbulent flow. Nevertheless, only droplets of the same diameter are regarded. The considered droplets must be smaller by at least one order of magnitude compared to the length scale of the small turbulent eddies. When the scales of motions are sufficiently small compared to the energy-containing eddies, the motion is isotropic and the mean values will depend only on the kinematic viscosity and on the rate of the energy dissipation per unit mass. Therefore, in order to use this theory, the energy dissipation rate must be known. Taylor ([Saffman and Turner, 1956](#)) deduced a value for that quantity of  $0.1 \text{ m}^2/\text{s}^3$  in clouds. Laboratory experiments by [Batchelor and Townsend \(1948\)](#) showed that the dissipation rate is in the order of  $u'^3/l$ . Considering the subsequent discussion in Chapter 5 and the values in Table 5.1 on page 100, this would lead to typical values around  $0.01 \text{ m}^2/\text{s}^3$ . According to the literature, a larger value of up to  $0.1 \text{ m}^2/\text{s}^3$  appears to be a better estimation for conditions in turbulent cumulus clouds.

There are two ways in which turbulence causes collisions between neighboring droplets:

1. collisions due to the motion of the droplets **with** the air;
2. due to the motion **relative** to the air.

The formula giving the collision rate of two drops with different size and number density moving with the air according to [Saffman and Turner \(1956\)](#) reads:

$$N = 1.30(r_1 + r_2)^3 n_1 n_2 \left( \frac{\varepsilon}{\nu} \right)^{1/2}, \quad (1.12)$$

where  $r_i$  is the radius of the interacting droplets [m] and  $n_i$  is the number density [ $\#/m^3$ ] of droplets of a given radius.

The authors of this publication also discuss that “the motion of the drops with the air will affect the mean properties of a cloud rather slowly, except under conditions of vigorous turbulence”. Hence, a further model is presented to quantify collision, where the motion of the drops with and relative to the

air are considered together with the relative motion due to gravity. After integration, the resulting equation can be written:

$$N = \left(\frac{8\pi}{3}\right)^{\frac{1}{2}} (r_1 + r_2)^2 n_1 n_2 \cdot \left[ 3 \left(1 - \frac{\rho_f}{\rho_p}\right)^2 (\tau_1 - \tau_2)^2 \overline{\left(\frac{Dv_f}{Dt}\right)^2} + \frac{1}{3} (r_1 + r_2)^2 \frac{\varepsilon}{\nu} \right]^{\frac{1}{2}} \quad (1.13)$$

This equation can be simplified using the assumption that the drops are identical (radius  $R$ ), leading to:

$$N = 1.67R^3 n_1 n_2 \left(\frac{\varepsilon}{\nu}\right)^{1/2}. \quad (1.14)$$

It can be seen that the difference with Eq. (1.12) is only in the constant. Note that the collision frequency depends only on particle size and concentration apart from dissipation and viscosity. For this equation to be valid, the particles should be smaller than the Kolmogorov microscale of turbulence,  $l_K$  and their relaxation times need to be smaller than the characteristic time scale of the dissipating eddies,  $\tau_K$ . In a more vigorous turbulence the approaching particles may no longer be entrained completely by the smallest eddies and they will have less-correlated velocities. If the particles are assumed to be randomly positioned with an independent, Maxwellian velocity distribution, it can be shown that the relative velocity is Maxwellian, too (Sundaram and Collins, 1997). If the variance of the velocity distribution is considered, the following form of the collision rate can be written following Abrahamson (1975). However, it is valid for larger particles ( $\text{Stk}_p > 1$ ), or for flows with high energy dissipation rates:

$$N = n_1 n_2 (r_1 + r_2)^2 \pi (u_{T,2} - u_{T,1}). \quad (1.15)$$

Since collision efficiency is a function of droplet size and more importantly of droplet relative velocity, Williams and Crane (1983) took into account more precisely the difference between gas and particle velocities. A universal solution was found, where isotropy is assumed and the collision frequency can finally be determined from:

$$N = \sqrt{\frac{8\pi}{3}} (r_1 + r_2)^2 n_1 n_2 \sqrt{3w^2}, \quad (1.16)$$

where  $w^2$  is the RMS relative velocity between air and particles due to the accelerative mechanism (inertia). Independently, Yuu (1984) also derived an equation, where the relative velocity was defined by two separate terms:

$$N = \sqrt{\frac{8\pi}{3}}(r_1 + r_2)^2 n_1 n_2 \sqrt{w_{inertia}^2 + w_{shear}^2}. \quad (1.17)$$

The relative RMS-velocities can be obtained by:

$$\begin{aligned} w_{inertia}^2 &= (A_1 - 2B + A_2)u_f^2 \\ w_{shear}^2 &= (A_1 r_1^2 + 2B r_1 r_2 + A_2 r_2^2) \left( \frac{\varepsilon}{3\nu} \right), \end{aligned} \quad (1.18)$$

with:

$$\begin{aligned} A_i &= \frac{\alpha_i T_L + b^2}{\alpha_i T_L + 1} \\ B &= \frac{C}{(\alpha_1 + \alpha_2)(1 - \alpha_1^2 T_L^2)(1 - \alpha_2^2 T_L^2)} \\ C &= \alpha_1 \alpha_2 T_L (2 - (\alpha_1 + \alpha_2) T_L - (\alpha_1^2 + \alpha_2^2) T_L^2 + \alpha_1 \alpha_2 (\alpha_1 + \alpha_2) T_L^3 \\ &\quad + b(\alpha_1 - \alpha_2)^2 T_L (1 - (\alpha_1 + \alpha_2) T_L + \alpha_1 \alpha_2 T_L^2) \\ &\quad + b^2((\alpha_1 + \alpha_2) - (\alpha_1^2 + \alpha_2^2) T_L - \alpha_1 \alpha_2 (\alpha_1 + \alpha_2) T_L^2 + 2\alpha_1^2 \alpha_2^2 T_L^3) \end{aligned} \quad (1.19)$$

The added mass coefficient  $b$ , which is called buoyancy coefficient by [Yuu \(1984\)](#), was defined as

$$b = \frac{3\rho_f}{2\rho_p + \rho_f} \quad (1.20)$$

and the reciprocal particle relaxation time  $\alpha_i$  is:

$$\alpha_i = 1/\tau_{p,i}. \quad (1.21)$$

All the above equations take into account only collisions induced by the local differences in fluid velocities. [Kruis and Kusters \(1997\)](#) stated that calculations based on the local difference in fluid velocities lead to an overestimation of the relative velocity of the two colliding particles and to unrealistic values of the collision frequencies. They proposed instead for the RMS relative velocity of two particles a dimensionless equation divided by the air flow velocity and considering dimensionless particle relaxation times:

$$\begin{aligned} \frac{w_{inertia}^2}{u_f^2} &= (1 - b)^2 \frac{\gamma}{\gamma - 1} \left( \frac{(\theta_1 + \theta_2)^2 - 4\theta_1 \theta_2 \sqrt{\frac{1 + \theta_1 + \theta_2}{(1 + \theta_1)(1 + \theta_2)}}}{\theta_1 + \theta_2} \right) \\ &\quad \times \left\{ \frac{1}{(1 + \theta_1)(1 + \theta_2)} - \frac{1}{(1 + \gamma\theta_1)(1 + \gamma\theta_2)} \right\}, \end{aligned} \quad (1.22)$$

where  $\gamma \approx 0.183 \text{ Re}_l^{1/2}$  is the turbulence constant, in which the Reynolds number corresponding to the large scale eddies is defined as usual:

$$\text{Re}_l = \frac{u' l}{\nu}. \quad (1.23)$$

The longitudinal integral length scale is  $l = u' t_l$ . The dimensionless particle relaxation time is  $\theta_i = \tau_{p,i}/t_l$ , which is the ratio between the particle relaxation time and the Lagrangian integral time scale, while  $u'$  is the RMS fluid velocity. It is also shown in [Kruis and Kusters \(1997\)](#) that for particles in the viscous subrange of turbulence, the universal equation reduces to the solution originally derived by [Saffman and Turner \(1956\)](#). It is similar to the case of turbulent cumulus clouds, where the viscous effects are preponderant, since the droplet diameter is well below the Kolmogorov length scale.

[Pinsky et al. \(1999\)](#) suggested a mathematical approach to the calculation of the collision efficiency between droplets within a turbulent flow and also confirmed that turbulence enhances droplet collision efficiencies. They also showed that the maximum values of collision efficiency can be several times larger than the mean values.

Table 1.2 summarizes the introduced equations and the associated assumptions. Finally, Eq. (1.12) is rejected, because it is only valid for very small particles, moving together with the air. This is not the case for cloud droplets which are large enough ( $> 20 \mu\text{m}$ ) to grow efficiently through collision/coalescence. As discussed earlier in this section, relative velocities between air and drops play an enormous role in the development of intense collision efficiencies. Therefore relative velocities should be included in any case, thus Eqs. (1.13) and (1.14) are also excluded. Equation (1.15) by [Abrahamson \(1975\)](#) is, on the other hand valid for high energy dissipation rates typical in cumulus clouds. Nevertheless, the condition of larger particles is not fulfilled in the range of the growth gap, shaping the primary focus of this work.

In the equation by [Williams and Crane \(1983\)](#), the collision rate is calculated based on the RMS of local relative velocities between air and droplets. This leads to overestimation of collision rates according to [Kruis and Kusters \(1997\)](#). Independently, [Yuu \(1984\)](#) derived a similar equation defining the RMS relative velocity separately for inertia and shear. Later [Kruis and Kusters \(1997\)](#) improved the theory and stated that the equations considering local differences in the fluid overestimate collision rates. These both equations (1.17) and (1.22) require the energy dissipation rate, which is challenging to measure. It is only available as a global mean value in the measurement section of the wind tunnel in our measurements. Therefore, Eq. (1.16)



**Table 1.2:** Summary and hints for the equations of the collision theory based on those of [Mersmann \(2001\)](#).

Validity	Assumptions	Equation
Droplets moving with the air	<ul style="list-style-type: none"> <li>• Particles follow fluid motion completely,</li> <li>• Relaxation time <math>\ll</math> smallest time scale,</li> <li>• <math>(r_1 + r_2)</math> is small compared to smallest turbulent eddies.</li> </ul>	1.12
Relative motion to the air	Only turbulent flow and gravity.	1.13
	Only turbulent flow and gravity, identical particles.	1.14
	Turbulent flow with high energy dissipation or large particles.	1.15
	<b>Collisions described by local differences in fluid velocities, isotropy assumed.</b>	<b>1.16</b>
	RMS relative velocity defined by separate terms for inertia and shear processes.	1.17
	RMS relative velocity defined depending on flow velocity and dimensionless particle relaxation time.	1.22

from [Williams and Crane \(1983\)](#) is used later in Chapter 5, where the experimentally determined collision rates are compared with those of the theory. The equation is applied in a form, allowing the calculation of collision rate of droplets belonging to different size classes. This is particularly important in the context of broad droplet size distributions as in our case. Note finally:

- that all terms of the selected equation are measured or can be directly derived and
- that this equation should overestimate collision rates, according to the statement of [Kruis and Kusters \(1997\)](#).

## 1.5 Conclusions and summary of goals

Scientific literature reports about the underestimation of collision rates by theory, especially in the range of 20...50  $\mu\text{m}$  droplets, the so-called growth

gap. This is the transition regime between the two main processes of droplet growth: condensation and gravity-driven collision. In order to investigate droplet-droplet interactions in the growth gap, careful measurements at laboratory conditions are required.

There are numerous experimental investigations concerning two-phase, air/water flows in the literature, also regarding meteorological aspects, but many important questions have not been answered in a satisfactory way yet. The aim of this work is to reproduce all important properties in a two-phase wind tunnel, where exact and non-intrusive investigations of droplet-droplet interactions with conditions similar to that in cumulus clouds are possible.

Properties of humid air have been introduced, corresponding calculations are included in the control software of the wind tunnel so that the flow can be characterized in a suitable way. The condensational droplet growth has been quantified and it is shown that growth through condensation is not the dominant mechanism in present measurement configurations, as expected.

Flow properties as well as particle concentrations will be systematically varied, so that their influence on collisions can be examined experimentally. The theory of droplet collisions has been reviewed and a suitable equation has been selected for comparison with experimental results. The influence of the probability density function (PDF) and of the number distribution can also be assessed in this manner. All experimental data are made freely available in a structured database at <http://www.ovgu.de/isut/lss/metstroem> for different flow configurations. In this way, boundary conditions can be delivered for numerical simulations and those can be validated by comparisons with high quality and structured experimental data.

The thesis is organized as follows. Fundamental considerations are first discussed in Chapter 2, followed by the details of experimental setup and measurement configurations in Chapter 3. Chapter 4 describes the improvements of different experimental techniques in order to adapt them for the challenging measurement conditions in the two-phase wind tunnel. The experimental results are then discussed in Chapter 5 including consequences for rain formation models. Finally conclusions and an outlook are proposed. At the end of this work the specifications of the wind tunnel and selected experimental results are presented.



# Fundamental considerations concerning optical flow measurements and tracers

---

In this chapter the basics of light refraction will be introduced. Furthermore, two possibilities will be considered to eliminate or avoid the limitation due to this phenomenon. Another common problem, the selection of suitable tracer particles will also be discussed and the flow response of different tracers will be quantified and compared. The suitability of water droplets as tracer particles will be analyzed as well.

## 2.1 Problem of light refraction

Light refraction is a physical phenomenon that often limits the quality or even the practicability of optical measurements. This is the reason why it is considered here. Some possibilities are shown to avoid or to correct its effect.

Objects become visible through the reflected or emitted light from their surface. When a ray of light reaches the boundary of two media with different optical density, it is either reflected or enters the new medium and is refracted. The cause for the refraction is the different light speed in the two media. A normal should be placed onto the boundary of the two media into the point of the incident ray of light (Fig. 2.1). The angle between the incident ray and the normal is the angle of incidence  $\theta$ , the angle between the refracted and the normal is the angle of refraction  $\theta'$  (see Fig. 2.1). The Snell–Descartes law states that the opposite ratio of the indices of refraction is a constant that depends on the media and is equivalent to the ratio of velocities in the two media

$$\alpha_{2,1} = \frac{c_1}{c_2} \quad (2.1)$$

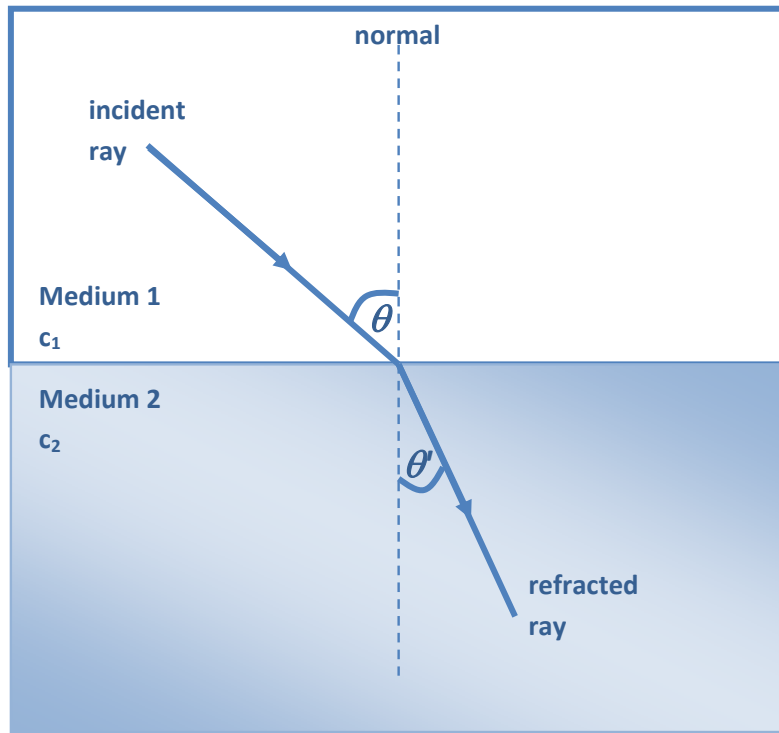


**Figure 2.1:** Representation of light refraction.

or equivalently to the sines of the angles of incidence and of refraction:

$$\alpha_{2,1} = \frac{\sin \theta}{\sin \theta'}. \quad (2.2)$$

The following statements should be considered:

- The incident and the reflected rays and the placed normal lie in the same plane.
- The two rays pass along different sides of the normal.
- The direction of the ray is reversible, i.e., the ray arriving to the boundary from the second medium with the angle  $\theta'$  passes with the angle  $\theta$  into the first medium.
- Rays of different wavelengths with the same angle of incidence refract with different angles. A prism decomposing white light into its components works in this way.

- A ray of light arriving normal to the boundary of the media passes without refraction through the plane.
- When the ray of light enters a medium of higher optical density, the angle of incidence is greater than that of the refraction ( $\theta > \theta'$ ). When the ray enters a medium of lower optical density, the angle of refraction is greater than that of incidence ( $\theta' > \theta$ ).

The index of refraction of a medium can be obtained from the ratio of the light speed in vacuum to that of the given medium.

The fact that a light ray refracts on the boundary of different media, causes errors during optical measurements, such as Laser–Doppler Velocimetry (LDV), Phase–Doppler Anemometry (PDA) or Particle Image Velocimetry (PIV). Therefore, these errors should be considered and if necessary, corrected. This is not always possible. E.g., when laser beams are extremely refracted, the measurement volume cannot be created at all (LDV/PDA). A further limitation is the critical angle. If it is reached by the incident beam, it is not refracted any more, but reflected. However, in case of LDV and PDA the correction is simple: the position of the measurement volume can be calculated in most cases and the receiving optics can also be adjusted so that the scattered light in the measurement volume can be recorded. Nevertheless, this correction is only useful if the position of the measurement volume is not influenced by the geometrical conditions when traversing the measurement volume. In case of PIV it is more complicated, as it is a planar measurement method and the distortion is not always regular as in the case of single ray refraction. There are then two possible methods to solve the latter problem, as explained next.

### 2.1.1 Refraction index matching

One solution method is to match the index of refraction of the flowing medium to that of the surrounding material. In this way the incident and refracting angles are the same, there is no refraction, as shown in Fig. 2.2. The limitation here is that it is not always possible to match the index of the flowing medium to that of the surroundings. Further on, mostly salts or oils are applied to modify the index of refraction, which can be harmful to the environment. As temperature influences the index of refraction as well, small differences in the index of refraction may be corrected by changing the temperature. Then, the set temperature should remain constant during the measurements (Wunderlich et al., 2007).

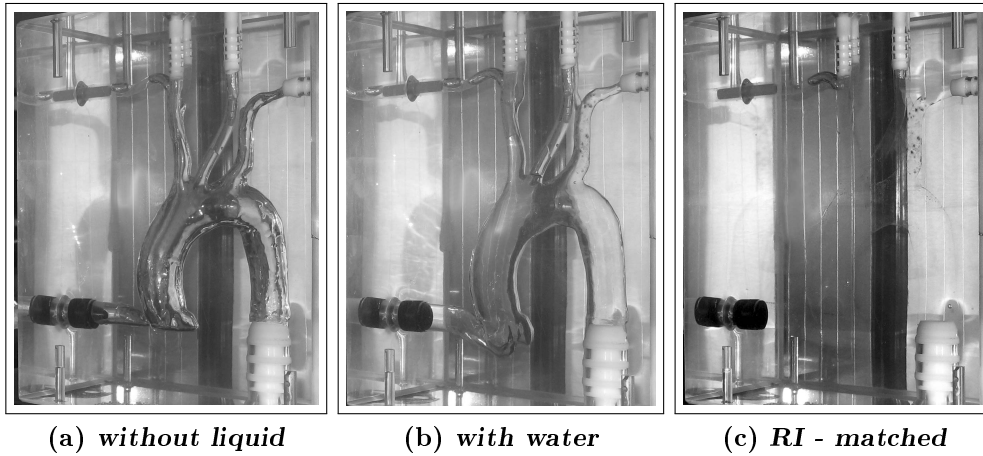


**Figure 2.2:** Image of an aorta model, in which the refractive index of the liquid has been matched to that of the silicon block in order to carry out LDV measurements. Left, without liquid filling, in the middle filled with water and on the right when filling with refractive index matched liquid (Wunderlich et al., 2007).

### 2.1.2 Image correction

The other solution is to apply image correction, which is a post processing tool, where the geometrical path of light rays is calculated a posteriori and a computational correction is then executed. In the work of Pap et al. (2009), an overview was presented about image correction methods and a practical solution (see Fig. 2.3) was introduced for a non-linear transformation using digital image processing.

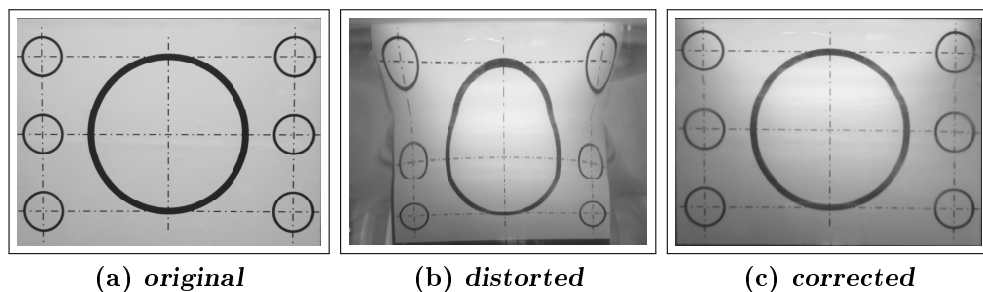


**Figure 2.3:** Left: original calibration pattern; middle: distorted image behind a curved surface; right: corrected image reconstructed from that in the middle (Pap et al., 2009).

In the present work, during PIV measurements of the velocity vectors lying in the plane normal to the flow direction in the two phase wind tunnel, such a correction is needed, as the camera axis and the normal of the measurement plane show an extremely large angle. Thus, dewarping the raw images by a commercial PIV software is insufficient to get proper results. The solution for this problem was presented in [Bordás et al. \(2009\)](#) and will be discussed later in Chapter 4.

## 2.2 Tracer particles for fluid measurement

The main problem when selecting proper tracer particles for optical measurement techniques, is that they should follow the flow accurately and be large enough to be detected by the cameras, or give sufficient signal for the photomultiplier of a LDV/PDA system. The latter problem appears especially in the application of the Particle Tracking Velocimetry (PTV) technique, since the particles might be illuminated by simple halogen lamps instead of a laser. In addition to the reduced illumination intensity, the tracers should be at least a few pixels large on the camera image, since the correspondence problem should be minimized by using colored tracer particles, and the cameras equipped with a Bayer pattern need at least 5 pixels to recognize the color of a particle in a reliable way ([Tarlet et al., 2009, 2010](#)).

### 2.2.1 Flow response

In an extensive theoretical and experimental investigation, the flow response of different tracer particles was compared with a conventional oil fog. Water droplets (WDR) of 10  $\mu\text{m}$  are also selected in this comparison to investigate their response to changes in the flow of the continuous phase.

Note that the diameter of tracer particles is larger than the oil or water droplets but their density is approximately one order of magnitude smaller. Both quantities have a decisive influence on the flow response of the particles, as will be shown later. The properties of all investigated tracers are collected in Table 2.1. [Melling \(1997\)](#) showed that oil droplets applied as tracer particles should have a diameter smaller than 3  $\mu\text{m}$  to be suitable. This value can be found as a reference value for polyethylene glycol (PEG)-droplets as well (e.g., von Dantec Dynamics). However, our own measurements by means of PDA showed a real mean diameter of 6.89  $\mu\text{m}$  when using commercial particle generators (see Fig. 2.4). Corresponding properties are included in Table 2.1



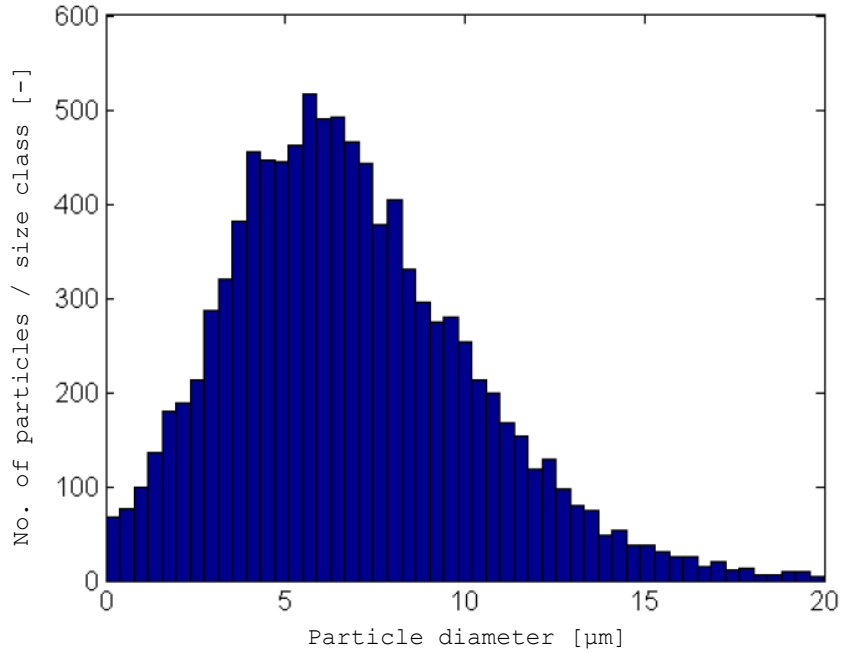


**Figure 2.4:** Droplet size distribution of the PEG fog, measured in the wind tunnel by means of PDA.

(PEG), together with ideal values of fog of vegetable oil, used as reference (REF).

For optical measurements of the flow velocity, tracer particles are needed. As the velocity of the tracer particles is measured instead of that of the flow field, it is most important that the particles follow the flow very accurately. The flow response of these particles is discussed in what follows.

### Settling velocity

One measure of the particle response in a fluid flow is the sinking velocity of the particle in the gravity field. The motion of the particle depends on the forces acting on it. The equation of motion for a single tracer can be given as (Ruck and Makiola, 1990):

$$\frac{du}{dt} = \left(1 - \frac{\rho_f}{\rho_p}\right) g - \frac{3 C_D \rho_f}{4 d \rho_p} \cdot u^2. \quad (2.3)$$

The force balance equation in Eq. (2.3) considers gravity, lift, drag and inertia. As the relative velocity should be the smallest possible, we can assure a laminar flow around the tracer and the drag coefficient can hence be written:

**Table 2.1:** Properties of potential tracer particles for gas flows. Both theoretically available and practically **considered**.

Material	Density [kg/m <sup>3</sup> ]	Diameter [μm]
EMS (Expancel <sup>®</sup> )	24...70 / <b>70</b>	15...120 / 15...25 ( <b>20</b> )
HGB (3M <sup>®</sup> )	>100 / <b>125</b>	30...120 / 30...40 ( <b>35</b> )
AMB <sup>a</sup>	40	35 / <b>35</b>
WDR	1000	1...2000 / <b>10</b>
PEG	1130	2...9 / <b>6.89</b>
REF	970	2...9 / <b>3<sup>b</sup></b>

<sup>a</sup>see Reeves et al. (2000)<sup>b</sup>according to theoretical calculations by Melling (1997) for a frequency limit of 1 kHz.

$$C_D = \frac{24}{\text{Re}}. \quad (2.4)$$

Substituting Eq. (2.4) in Eq. (2.3), we get

$$\frac{du}{dt} = \left(1 - \frac{\rho_f}{\rho_p}\right)g - 18\frac{\rho_f \nu}{\rho_p d^2}u. \quad (2.5)$$

It is a linear differential equation, which can be written after integration:

$$u(t) = \frac{1}{18} \frac{\rho_p d^2}{\rho_f \nu} \left(1 - \frac{\rho_f}{\rho_p}\right)g \left[1 - \exp\left(-18\frac{\rho_f \nu}{\rho_p d^2}t\right)\right]. \quad (2.6)$$

The forces acting on the particle are in equilibrium, when the initial acceleration is finished. The terminal velocity  $u_T$  in case of a laminar flow around a spherical body can be written:

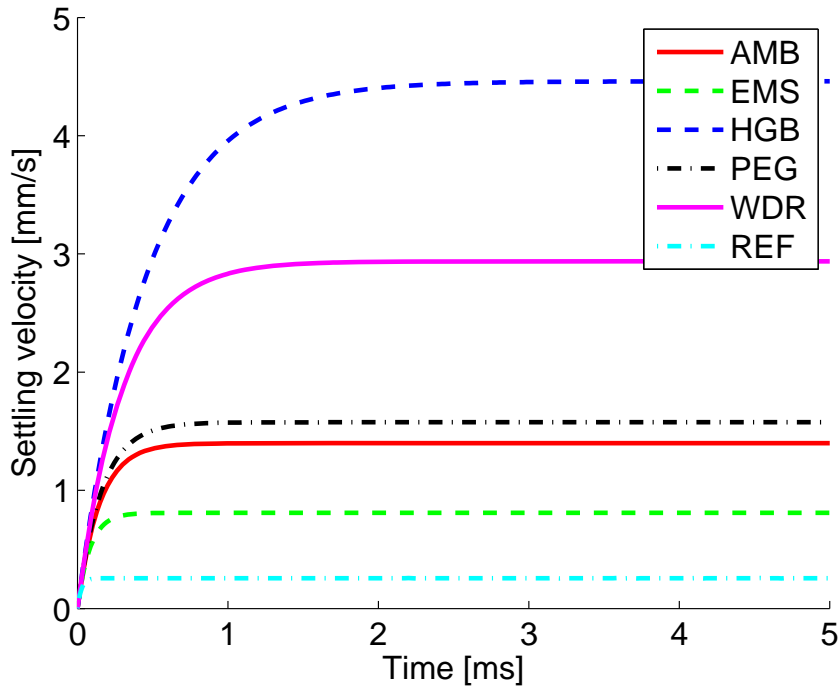
$$u_T = \frac{1}{18} \frac{\rho_p d^2}{\rho_f \nu} \left(1 - \frac{\rho_f}{\rho_p}\right)g. \quad (2.7)$$

Table 2.2 contains the calculated terminal velocity values  $u_T$  of all tracer particles listed in Table 2.1. The time values  $t_T$ , needed to reach 99.9% of the terminal velocity are also given. The calculation of these values is based on the differential equation Eq. (2.5), integrated with the help of a Matlab<sup>®</sup> script. The temporal course of the velocities is presented graphically in Fig. 2.6.

**Table 2.2:** Terminal velocity values for different tracer particles ( $\vartheta = 20^\circ\text{C}$ ,  $p = 1 \text{ bar}$ ).

	AMB	EMS	HGB	PEG	WDR	REF
$\rho_f [\text{kg/m}^3]$	1.188					
$\nu [\text{m}^2/\text{s}]$	$1.535 \cdot 10^{-5}$					
$\rho_p [\text{kg/m}^3]$	40	70	125	1130	1000	970
$d_p [\mu\text{m}]$	35	20	35	6.89	10	3
$v_T [\text{mm/s}]$	1.40	0.81	4.46	1.58	2.94	0.257
$t_T [\text{ms}]$	0.745	0.458	1.770	0.791	1.290	0.152

As already shown, the settling velocity of particles depends on the density of both media, on the diameter of the particles and on the viscosity of the fluid. The application of the previous equations is only valid for a density ratio of  $\frac{\rho_p}{\rho_f} > 1$  (e.g., particles in air flow), otherwise the direction of the forces should be checked.



**Figure 2.5:** Settling velocity of the considered particles in air as a function of time.

The oil droplets, selected as reference (REF) have the smallest terminal velocity and reach it fastest. After REF, with a diameter of  $3 \mu\text{m}$ , the expanded microspheres (EMS)–particles with a diameter of  $20 \mu\text{m}$  have the best flow response. The PEG–droplets with the measured mean diameter of  $6.89 \mu\text{m}$

have approximately the same flow response as the acrylonitrile microbubbles (AMB)–particles with 35  $\mu\text{m}$  diameter. The worst particles are the water droplets with a diameter of 10  $\mu\text{m}$  and the hollow glass bubbles, illustrating the quadratic influence of the diameter on the settling velocity. Thus, water droplets cannot be used directly as tracer particles of the air flow; additional tracers are needed for the measurement of the continuous phase.

### Relaxation time

The first part of Eq. (2.7) is a characteristic time and can be used to measure, how fast the particles react to changes in flow velocity (Crowe, 2006):

$$\tau_p = \frac{1}{18} \frac{\rho_p d^2}{\rho_f \nu} . \quad (2.8)$$

The relaxation time  $\tau_p$  corresponds to the time, which is needed for a particle to reach 63% of its terminal velocity (Kussin, 2004) after a sudden acceleration of the fluid.

Inserting Eq. (2.8) in Eq. (2.7):

$$u(t) = u_T \left[ 1 - \exp\left(-\frac{t}{\tau_p}\right) \right] . \quad (2.9)$$

Both Fig. 2.6 and Eq. (2.9) show that the particle velocities approach exponentially their terminal velocities, i.e., a particle with a good flow response has got a low relative velocity compared to the continuous flow and reaches it rapidly as well. This corresponds to a small relaxation time  $\tau_p$  (see calculated values in Table 2.3).

### Stokes number

The Stokes number is the ratio of the particle relaxation time,  $\tau_p$  (see Eq. (2.8)) and of the Kolmogorov time scale  $\tau_K$  (see Eq. (3.8) later in Chapter 3). It measures the flow response of particles in a turbulent flow in case of a Stokes flow around the particle:

$$\text{Stk} = \frac{\tau_p}{\tau_K} . \quad (2.10)$$

If  $\text{Stk} \ll 1$  the particle reacts with a small time lag to the changes in the flow velocities – it follows the pathlines of the fluid. If  $\text{Stk} \gg 1$ , the particle velocity is no more influenced by the changes in flow velocities, i.e., the pathlines deviate from each other (Crowe et al., 1998).

Shaw (2003) deduces the divergence of the droplet velocity

$$\nabla u_p = -(\tau_p/4)(4e_{ij}e_{ij} - r_{ij}r_{ij}) \quad (2.11)$$

from the solution of a simplified form of the droplet equation of motion. Here,  $e_{ij}$  is the strain rate tensor and  $r_{ij}$  the rotation tensor. The droplet velocity field is divergent for large vorticity and is convergent for large strain rate. This allows to understand Maxey’s conclusion (Maxey, 1987): “particles will tend to accumulate in regions of high strain rate or low vorticity”. Qualitatively, it can be said that particles with very small  $\text{Stk}$  tend to follow fluid streamlines and particles with very large  $\text{Stk}$  do not respond to the fluid significantly during the lifetime of an eddy. Therefore, particles with Stokes numbers  $\simeq 1$  are effectively resonant with dissipation-scale eddies in turbulent flows.

**Table 2.3:** Characteristic timescale of the flow and calculated relaxation times and Stokes numbers.

	AMB	EMS	HGB	PEG	WDR	REF
$\tau_p$ [ms]	0.152	0.088	0.458	0.163	0.307	0.027
$\tau_K$ [ms]			7.313			
$\text{Stk} (\times 10^{-2})$	2.08	1.20	6.26	2.23	4.20	0.37

Table 2.3 contains the calculated Stokes numbers, based on the values in Table 2.1 and in Table 3.6 on page 62. The values in Table 2.3 are suitable to compare the flow response of different particles. The order of the flow responses is consistent with that of the settling velocities (Table 2.2): REF, EMS, PEG, AMB, water droplets (WDR) and finally the hollow glass bubbles (HGB). All values are in the order of magnitude of  $10^{-2}$ . Nevertheless, HGB and WDR have the largest values and thus are the worst passive tracers (Ouellette et al., 2006). This means that the water droplets are not small enough to follow the air flow properly and cannot be used directly as tracer particles.

## 2.2.2 Equation of motion for spherical particles

Originally Basset (1888) and later Boussinesq (1903) and Oseen (1927) investigated the motion of a sinking sphere in a steady gravitational flow field. Tchen (1947) extended this work for unsteady inhomogeneous flow fields:

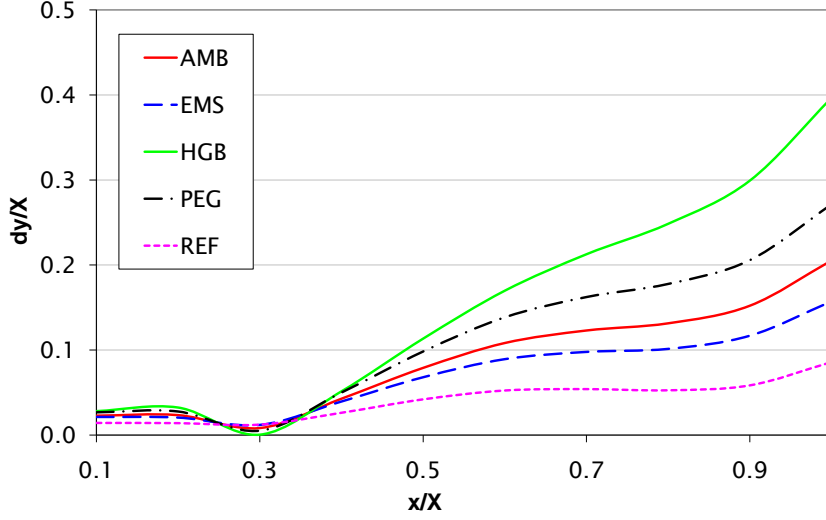


**Figure 2.6:** Illustration of the normalized deviation between different particle and fluid trajectories (Bordás et al., 2008).

$$\begin{aligned} \frac{\pi}{6} d_p^3 \rho_p \frac{du_p}{dt} = & 3\pi\mu_f d_p (u_f - u_p) + \frac{\pi}{6} d_p^3 \rho_f \frac{du_f}{dt} + \frac{\pi}{12} d_p^3 \rho_f \frac{d(u_f - u_p)}{dt} + \\ & \frac{3}{2} d_p^2 \sqrt{\pi\rho_f\mu_f} \int_{t_0}^t \frac{d}{dt'} (du_f - du_p) \frac{1}{(t-t')^{\frac{1}{2}}} dt' \quad (2.12) \end{aligned}$$

The resultant force acting on a particle consists of following components: Stokes drag, acceleration due to unsteady fluid motion, acceleration due to pressure and virtual mass and the Basset time history force. The Basset–Boussinesq–Oseen (BBO) equation, based on the terms in Eq. (2.12) and extended with the external forces ( $F_E$ ) such as gravity or lift force, was described in details by Hinze (1975):

$$\begin{aligned} \frac{du_p}{dt} = & \frac{18\nu}{(\frac{\rho_p}{\rho_f} + \frac{1}{2})d_p^2} (u_f - u_p) + \frac{3}{2(\frac{\rho_p}{\rho_f} + \frac{1}{2})} \frac{du_f}{dt} + \\ & \frac{9}{(\frac{\rho_p}{\rho_f} + \frac{1}{2})d_p} \sqrt{\frac{u_f}{\pi}} \int_{t_0}^t \frac{d}{dt'} (du_f - du_p) \frac{1}{(t-t')^{\frac{1}{2}}} dt' + F_E \quad (2.13) \end{aligned}$$

Later, Tchen extended the equation for application in inhomogeneous turbulent flows. Since then, several works correcting or modifying single terms of the equation have been published. These are discussed in great detail by Maxey and Riley (1983) and the up to date motion equation can be written:

$$\begin{aligned}
 m_p \frac{du_p}{dt} &= (m_p - m_f)g + m_f \frac{du_f}{dt} - \frac{1}{2} m_f \frac{d}{dt} \left( u_p - u_f - \frac{1}{10} d_p^2 \nabla^2 u_f \right) \\
 &- 6\pi d_p \mu_f \left( u_p - u_f - \frac{1}{6} d_p^2 \nabla^2 u_f \right) - 6\pi d_p^2 \mu \int_0^t \frac{\frac{d}{dt'} (u_p - u_f - \frac{1}{6} d_p^2 \nabla^2 u_f)}{[\pi \nu (t - t')]^{\frac{1}{2}}} dt'
 \end{aligned} \tag{2.14}$$

This equation is valid in turbulent clouds as well, including interaction between particles. The influence of collision-coalescence should be considered, but the typical drop volume fraction in clouds ( $\phi = n \frac{d^3 \pi}{6} \approx 10^{-6}$ ) is sufficiently small, so that these interactions can first be neglected. To understand the origin of particle clustering in turbulent flows, it is especially interesting to deal with the terms containing the relative particle-fluid velocity.

**Shaw (2003)** defined the relative velocity by  $w = u_p - u_f$  and divided the equation of motion by the droplet mass:

$$\begin{aligned}
 \frac{dw}{dt} &= -\frac{w}{\tau_p} - \frac{\rho_f \dot{w}}{\rho_p 2} - \left( \frac{9}{2\pi \tau_p} \frac{\rho_f}{\rho_p} \right)^{1/2} \int_0^t \frac{\dot{w}(t')}{\sqrt{t - t'}} dt' \\
 &+ \left( 1 - \frac{\rho_f}{\rho_p} \right) g - \left( 1 - \frac{\rho_f}{\rho_p} \right) \dot{u}, \tag{2.15}
 \end{aligned}$$

where the dotted symbols are the derivatives of the variables with respect to time  $t$ .

He pointed out that the terms without the relative velocities are only the non-homogeneous terms in the differential equation and can therefore be considered as the external driver for droplet motion.

Further on it is necessary to introduce characteristic scales  $\tau_K$  and  $u_0$  for the fluid and  $w_0$  for the relative velocity. Then, the droplet acceleration can be written in a dimensionless form (unknowns marked with a “\*”). The relative droplet acceleration scale  $\dot{w} = (w_0/\tau_K)\dot{w}_0^*$ , the fluid acceleration scale  $\dot{u} = (u_0/\tau_K)\dot{u}_0^*$  and the gravitational acceleration can be written:  $g = |g|g^*$ . In this form three natural, dimensionless parameters arise from the equation of motion:

- The density ratio  $s = \rho_f/\rho_d$ ,
- The droplet Stokes number  $\text{Stk}_d = \tau_p/\tau_K$ ,

- and the acceleration ratio (Froude number)  $\text{Fr} = g\tau_K/u_0$ .

Using these definitions and neglecting terms of order  $10^{-3}$  and smaller, Eq. (2.15) can be rewritten (Manton, 1977):

$$w^* + \text{Stk}_d \dot{w}^* + \left(\frac{9s}{2\pi} \text{Stk}_d\right)^{1/2} \int_0^{t^*} \frac{\dot{w}}{\sqrt{t^* - t'}} dt' = -\text{Stk}_d \frac{u_0}{w_0} (\dot{w}^* - \text{Fr}g^*). \quad (2.16)$$

Assuming that the acceleration ratio  $\text{Fr} \gg 1$ , the solution of the equation represents a simple relaxation of the relative velocity to the terminal fall speed. However, it has been pointed out that even in moderately turbulent clouds the Lagrangian fluid acceleration  $\dot{w}$  can be of the same order of magnitude as  $g$ . In localized regions it can even greatly exceed it (La Porta et al., 2001). As a consequence, the full equation must be used, but clearly much of the physics of droplet motion in a turbulent cloud is included in the Stokes number  $\text{Stk}_d$  and the acceleration ratio  $\text{Fr}$ .

### Response frequency

Hjelmfelt and Mockros (1966) solved the BBO differential equation by means of the Fourier integral method according to Hinze (1975). Then, the amplitude ratio between particle and fluid velocity can be defined as

$$\eta = \sqrt{(1 + f_1)^2 + f_2^2}. \quad (2.17)$$

The phase angle of both velocities is

$$\beta = \arctan\left(\frac{f_2}{1 + f_1}\right). \quad (2.18)$$

Here,  $f_1$  and  $f_2$  are written in dimensionless form, for easier handling

$$f_1 = \frac{\left[1 + \frac{9}{\sqrt{2}(s+\frac{1}{2})} N_S\right] \left[\frac{1-s}{s+\frac{1}{2}}\right]}{\frac{81}{(s+\frac{1}{2})^2} \left[2N_S^2 + \frac{N_S}{\sqrt{2}}\right]^2 + \left[1 + \frac{9}{\sqrt{2}(s+\frac{1}{2})} N_S\right]^2} \quad (2.19)$$

and



$$f_2 = \frac{\frac{9(1-s)}{(s+\frac{1}{2})^2} \left[ 2N_S^2 + \frac{N_S}{\sqrt{2}} \right]}{\frac{81}{(s+\frac{1}{2})^2} \left[ 2N_S^2 + \frac{N_S}{\sqrt{2}} \right]^2 + \left[ 1 + \frac{9}{\sqrt{2}(s+\frac{1}{2})} N_S \right]^2}, \quad (2.20)$$

where

$$s = \frac{\rho_p}{\rho_f} \quad (2.21)$$

is the density ratio and

$$N_S = \sqrt{\frac{\nu}{\omega d_p^2}} \quad (2.22)$$

is the Stokes number of the fluid oscillations (not identical with that of Eq. (2.10)).

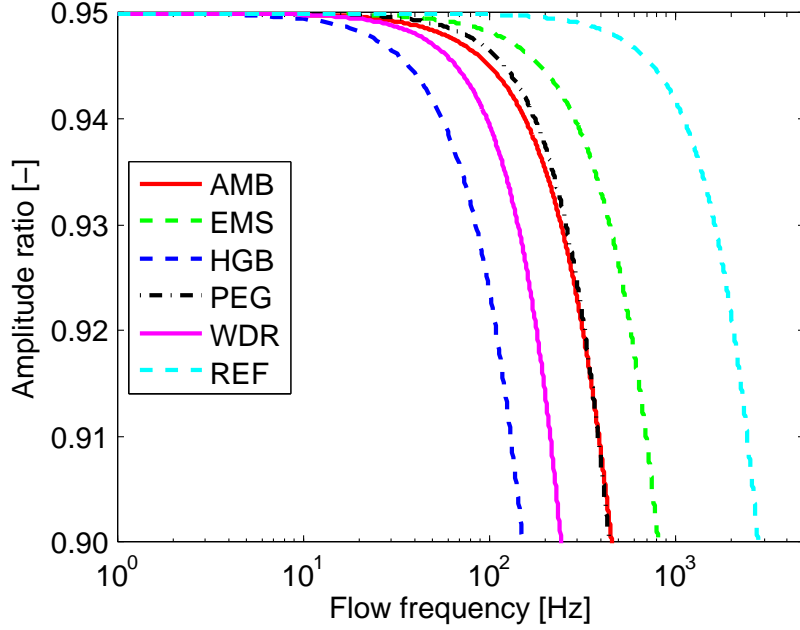


**Figure 2.7:** Amplitude ratio  $\eta$  between particle and fluid velocity against oscillation frequency of the flow.

The relation between  $\eta$  and the oscillation frequency of the flow for the considered tracer particles is presented in Fig. 2.7. The dependency of the frequency limit on diameter is shown in Fig. 2.8, where the calculated frequency limits for

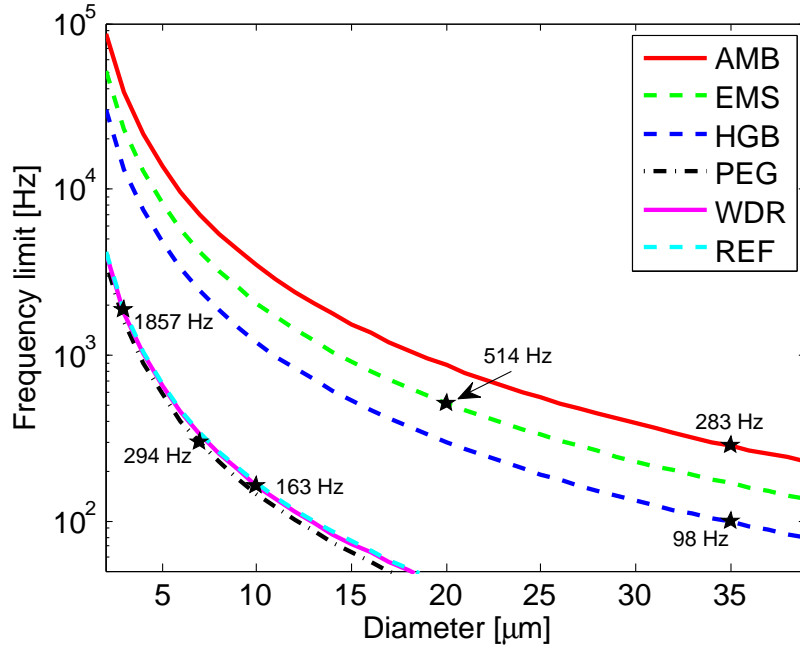


**Figure 2.8:** Limit frequency versus particle diameter. The amplitude ratio  $\eta$  is fixed to a value of 95% .

the applied diameters are marked in the diagram with a “ $\star$ ” and summarized in Table 2.4.

**Table 2.4:** Frequency limits of a flow, in which the particles can react to changes with an amplitude ratio of 95% .

	Diameter [ $\mu\text{m}$ ]	$f_{limit}$ [Hz]
AMB	35	283
EMS	20	514
HGB	35	98
PEG	6.89	294
WDR	10	163
REF	3	1 857

In Table 2.4, it can be seen that the oil fog with a diameter of 3  $\mu\text{m}$  has got the best flow response. The second best particles are EMS-particles, even if they have a diameter one order of magnitude larger. EMS-particles are able to follow flow oscillations of over 500 Hz. The real oil fog tracer particles are the second worst particles in the comparison. Only HGB and WDR are even worse and are hence non-suitable as tracer particles for the gas flow.

### 2.2.3 Computational comparison

Beyond solving transport equations for a continuous phase, CFD softwares are also capable of simulating a discrete, second phase by means of Lagrangian particle tracking, dispersed in the continuous flow medium. In the present case, the particle trajectories are computed by means of the CFD software Fluent<sup>®</sup>. Drag, virtual mass and gravity are considered. In addition the acceleration due to unsteady motion of the fluid is also taken into account for the dispersion of the particles.

The Lagrangian discrete phase model in Fluent<sup>®</sup> follows the Euler–Lagrange approach. The fluid phase is treated as a continuum, for which the time averaged Navier–Stokes equations are solved. Whereas the disperse phase in form of particles, bubbles or droplets is tracked in the already computed flow field. The disperse phase can exchange momentum, mass and energy with the fluid phase.

A Fluent<sup>®</sup> simulation was started to numerically investigate the flow response of the considered tracer particles. The steady air flow was first computed using a standard  $k - \varepsilon$  turbulence model. The different tracer particles were then injected at the same position (0, 0, 90) mm, with an initial velocity of the air flow at that position. Inlet boundary condition was defined by the measured  $x$ -velocities and the corresponding turbulent kinetic energy at each measurement point. Outlet boundary condition was a fixed pressure. The remaining four sides of the rectangular volume were defined as slip walls, since only the measurement section was modeled, without any influence of the walls of the test section. After convergence the resulting velocity field is presented in Fig. 2.9.

Trajectories of individual particles are then calculated on top of the continuous phase. The applied model is suitable for the current case as long as the number density of the particles is so low that there is no interaction among the particles and no influence of the particles on the gas phase.

#### Motion equation for the particles

Fluent<sup>®</sup> computes the trajectory of a particle of the disperse phase by integration of the force equilibrium on the particle considering a Lagrangian frame of reference. This force equilibrium equates particle impulse with the forces acting on the particle and can be written (for instance in the  $x$ -direction) as:

$$\frac{du_p}{dt} = F_D(u_f - u_p) + \frac{g_x(\rho_p - \rho_f)}{\rho_p} + F_x, \quad (2.23)$$

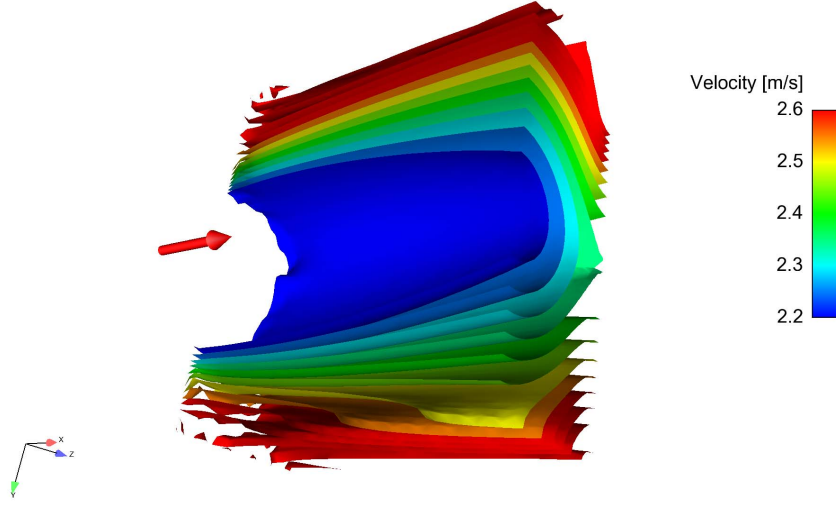


**Figure 2.9:** Iso-surfaces of the simulated flow field in the test section of the wind tunnel.

where  $F_x$  is an additional acceleration term and  $F_D(u_f - u_p)$  is the drag force acting on the particle per unit mass.

$$F_D = \frac{18\mu}{\rho_p d_p^2} \frac{C_D \text{Re}}{24}. \quad (2.24)$$

Here  $\text{Re}$  is the relative Reynolds number, defined by

$$\text{Re} \equiv \frac{\rho_f d_p |u_f - u_p|}{\mu}. \quad (2.25)$$

Equation (2.23) includes gravity as well as external forces ( $F_x$ ), which might be significant for special conditions.

$$F_x = \left( \frac{\rho_f}{\rho_p} \right) u_p \frac{\partial u_f}{\partial x} \quad (2.26)$$

Further forces may be important in the case of submicron particles, rotating reference frames or strong thermal effects. [Hjelmfelt and Mockros \(1966\)](#) investigated the influence of neglecting the history term. For the present Stokes numbers, calculated from particle properties and frequency limit (Table 2.4), the difference between the original and the simplified model is negligible. Therefore, the history term can be safely neglected in the equation of motion. The simplified BBO-equation (without the time history term) can be written

$$\frac{du_p}{dt} = a(u_f - u_p) + b \frac{du_f}{dt}, \quad (2.27)$$

where

$$a = \frac{18\nu}{d_p^2 \left( \frac{\rho_p}{\rho_f} + \frac{1}{2} \right)} \quad (2.28)$$

$$b = \frac{3}{2 \left( \frac{\rho_p}{\rho_f} + \frac{1}{2} \right)}. \quad (2.29)$$

Only a part of this equation (see Eq. (2.26)) can be activated by default in Fluent®. The remaining part, which reads

$$F_x = \frac{3}{2(s+1)} \frac{du_f}{dt} - \frac{9\nu}{s(s+1)d_p^2} (u_f - u_p), \quad (2.30)$$

has been additionally implemented in form of a user defined function (UDF), so that an accurate computation of the particle trajectories becomes possible.

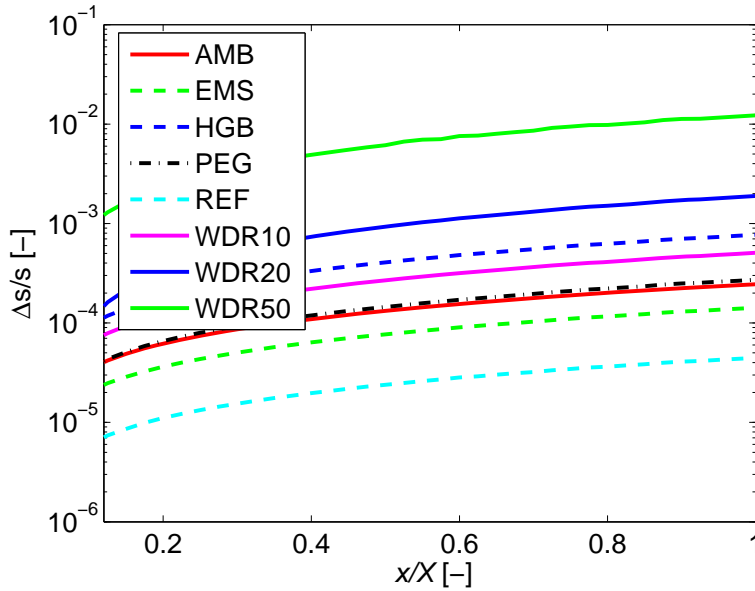


**Figure 2.10:** Dimensionless deviation of trajectories from the ideal one for the considered tracer particles.

Figure 2.10 depicts the dimensionless deviation of particle trajectories from the ideal, gas flow pathline.  $x$  values are normalized by the length of the measurement section (0.4 m) and the deviation from the ideal trajectory by the length of the already covered path. Simulation results are in agreement with the previously found order of flow response, showing the large deviations of water droplets and HGB particles.

Final conclusions from this section, with regard to future wind tunnel experiments, are that water droplets with a mean diameter of  $\geq 10 \mu\text{m}$  are clearly

unsuitable to measure any flow property of the continuous gas phase. Flow velocities should be measured separately by means of dedicated tracer particles with good flow response.

## Conclusions

In this chapter basics of light refraction and two possible solutions for its correction or elimination have been presented, including practical applications as well. Another important topic, the selection of suitable tracer particles has also been discussed. Flow response of several tracer materials has been quantified and it can be concluded that

- the Stokes number is useful for a first comparison, but not enough for a quantitative statement concerning flow response;
- the flow frequency defines whether a particle is a suitable tracer or not;
- water droplets larger than 10  $\mu\text{m}$  are not suitable tracers. Therefore, the velocity of the continuous phase should be measured with separate tracer particles;
- most suitable tracers would be the REF particles used as reference in the comparison presented in this chapter. However, own measurements showed that the actually generated particles (PEG) have larger diameter. Considering cost, cleaning and disposal problems, the PEG tracers (with the smallest possible diameter) are found to be the most suitable as tracer particles and are still appropriate for the present conditions. Therefore, these tracers are used for both PIV and LDV measurements during further measurements.

Chapter 3 now describes the wind tunnel with the injection system, the four measurement configurations (M1–M4) considered in this work and the applied measurement methods.



# Experimental setup

---

In this chapter the experimental setup is introduced in details:

- the two-phase wind tunnel with its control and injection system including our newly developed software;
- the different configurations used for the generation of controlled flow structures and turbulence
- and the applied optical, non-intrusive measurement techniques.

## 3.1 Two-phase wind tunnel

For the investigation of disperse two-phase (water droplets in air) flows, a special two-phase wind tunnel is available in the laboratory of Fluid Dynamics & Technical Flows (Fig. 3.1). It is a fully computer-controlled, Göttingen-type wind tunnel. Operation with a closed test section enables the investigation of two-phase (air/liquid) mixtures in the test section (see Fig. 3.2) with the following dimensions ( $H \times W \times L$ ):  $500 \times 600 \times 1500$  mm. In the region of the measurement section, the walls of the closed test section are optically transparent ( $450 \times 500$  mm) in the visible spectrum. These windows made non-intrusive measurements possible, which was indispensable for a high quality experimental investigation of such flows.

Air flow velocity can be adjusted from 0.3 to over 50 m/s, with an incremental increase of 0.03 m/s, limited by the electronic regulation. Turbulence intensity of the undisturbed air flow in the measurement section was below 0.5%. Operation with pulsating velocity is also possible up to a frequency of a few Hz. This enables the artificial increase of turbulent kinetic energy through larger fluctuating velocities with a relatively long time scale (several 100 ms up to several seconds). A detailed summary about wind tunnel parameters can be found in Appendix A on page 123.



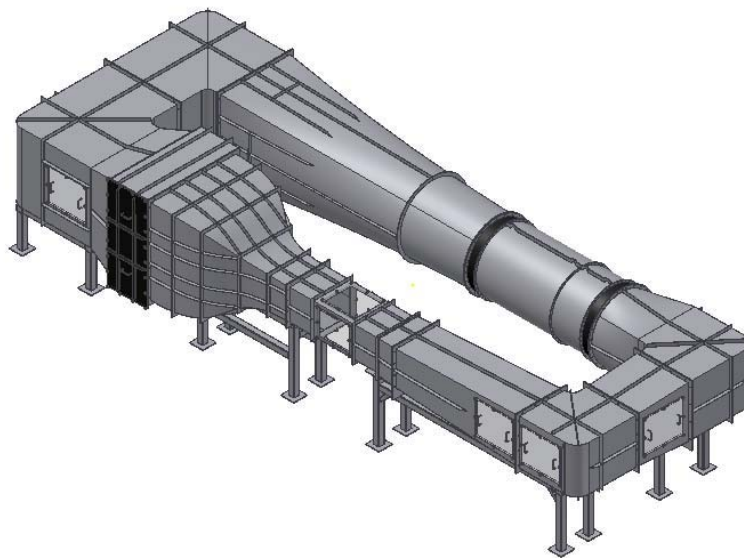


**Figure 3.1:** Göttingen-type two-phase wind tunnel with closed test section. The test section is shown in Fig. 3.2 in detail.

### 3.1.1 Injection system

The disperse phase can be injected as sprays through different nozzles by means of eccentric pumps, type MD 006–24, of which the RPM was set with the help of a frequency regulator. The maximal volume flow rate of the pumps was 50 l/h, which could be reduced by manually adjusting the bypass valves to the required volume flow rate. Finally, the values are electronically set to a certain value with a programmed Proportional–Integral–Differential (PID) regulation in LabView®. Both pressure atomizers for larger drops and air-assisted atomizers for smaller droplets can be used to generate the required droplet spectra. The system can also accommodate a double atomizer configuration. Thus, not only monomodal but also bimodal droplet size distributions may be generated. Air-assisted atomizers are systematically used to investigate cloud droplet interactions.

First measurements showed that placing the nozzle farther from the entrance of the test section leads to a reduced influence of the injection system on the velocity distribution. The farther the nozzle is, the smaller the deviation is from the undisturbed flow velocity. Therefore, to decrease the influence of the injection system (the wake of the supporting cylinder), the farthest hatch was selected, with a distance between nozzle and position  $x = 0$  (inlet of the measurement section) of 630 mm. Since the influence of the support

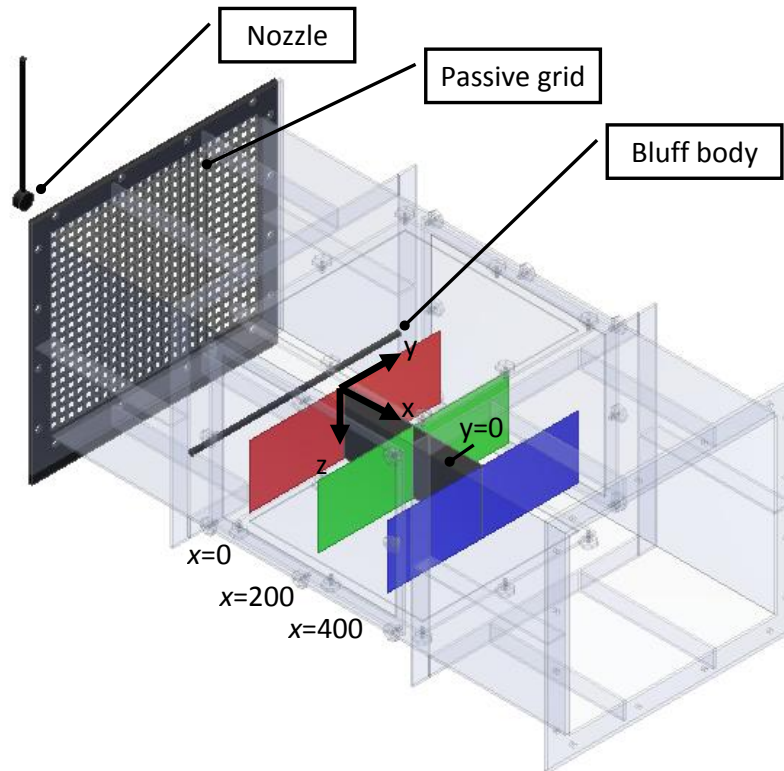


**Figure 3.2:** Transparent test section with optional passive grid and cylindrical bluff body. The coordinate system and measurement planes are marked as well.

of the injection system could be noticed especially in the upper half of the measurement section, the measurement area is finally limited to the lower half of the cross-section (see Fig. 3.4).

Originally, the selected nozzle had got a marked six-hole spray pattern caused by the six orifices (Fig. 3.3). To reduce this effect, the water was injected in counter-flow direction. In this way the droplets were more homogeneously distributed, the relative velocity between continuous and disperse flow was minimized, and the six-hole pattern was reduced before entering the measurement section. Finally, the velocity inhomogeneity of the air flow without droplet injection at the entrance of the measurement section was then below  $\pm 5\%$ , with a turbulence intensity below 7% (mean value of 2.4%).

To create the relatively small droplets found in cumulus clouds, an air-assisted atomizer was required. After several tests, this requirement could be finally realized successfully by means of a full cone pneumatic atomizing nozzle 166.208.16.12 with liquid pressure principle from the co. Lechler, applying

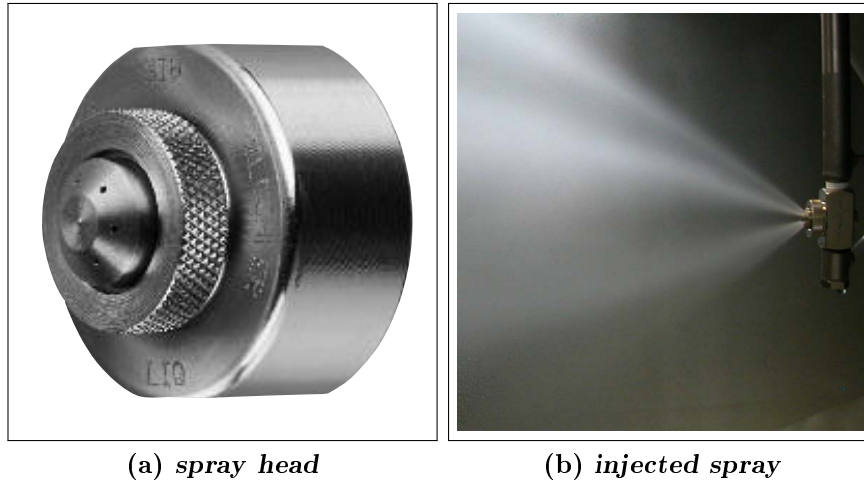


**Figure 3.3:** Close view of the spray head (left) and injected spray (right).

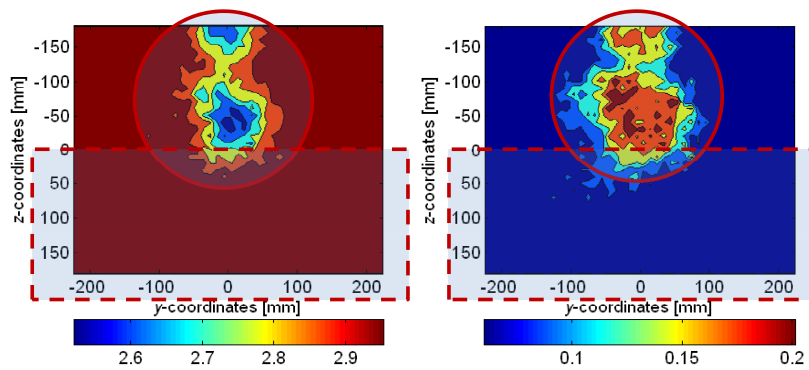


**Figure 3.4:** Mean axial velocity (left) and turbulence intensity (right) distribution of the air flow, without droplet injection at the entrance of the measurement section – 630 mm behind the nozzle ( $x = 0$  mm). The circles show the influence of the injection and the dashed rectangle the selected measurement section, with minimal influence of the injection system.

an air gauge pressure of 1.2 bar. To keep the inlet values constant, a PID-controller was programmed. In this way it was possible to create a steady water volume flow rate, through which the droplet diameter remained constant during full-day measurements.

Measurements by means of PDA showed that the mean droplet diameter ( $d_{10}$ ) of the generated water spray was around  $12.5 \mu\text{m}$  as shown in Fig. 3.5. This is a typical value in cumulus clouds. [Bhatia et al. \(1988\)](#) showed that a log-hyperbolic (LH) distribution is suitable for the characterization of sprays,

though the stability of parameter estimation using the four-parameter-LH distribution was limited. This problem was discussed by Xu et al. (2008), and explanations were given for its causes. It was concluded that the three-parameter-LH distribution circumvents these problems, while yielding a nearly equally good representation of the data for a large variety of applications. For the reconstruction of the present DSD a log-normal distribution function appeared perfectly suitable, as discussed in Hagemeyer et al. (2008) (Fig. 3.5).

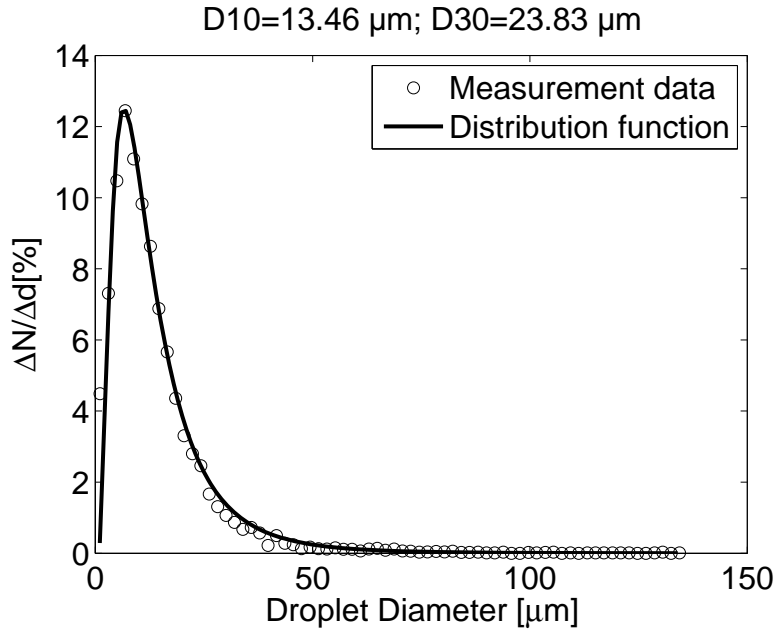


**Figure 3.5:** Droplet size distribution and suitable log-normal distribution function at  $x = 0, y = -5, z = 90$ , measured by PDA.

If one estimates the surface integral of the velocity at the inlet plane of the measurement section (cross-section of the wind tunnel:  $0.3 \text{ m}^2$ ), the volume flow rate of the air phase can be calculated.  $\dot{Q}_{air} = \int_A u dA = U A = 0.75 \text{ m}^3/\text{s}$ . The product of the required LWC ( $2 \text{ g}/\text{m}^3$ ) and the volume flow rate of the air phase in the wind tunnel divided by the water density gives the water amount per unit time that should be injected ( $0.09 \text{ l}/\text{min}$  in this case). As the injection took place in counter flow direction, not all the droplets could turn around with the air flow and some of them deposited on the walls before reaching the measurement section. This fact should also be taken into account in order to inject the right amount of water. During a measurement duration of 10 hours, 6 liters of extracted water could be found in the water vessel right before the test section. This means a water flow of  $0.01 \text{ l}/\text{min}$ . Summing up these two values, the required water amount was  $0.1 \text{ l}$  that should be injected in a minute. This value has been used in practice for all measurements.

### 3.1.2 Control system

The wind tunnel is originally equipped with the measurement instruments listed in the following and with a control software. However, in order to improve flexibility and to take into account our special requirements (two-phase measurements, possibly pulsatile flows) the commercial control software was replaced by our own, programmed in LabView®.

**Table 3.1:** Main properties of the AK4a A/D converter and ADA2 A/D–D/A converter.

<b>AK4a A/D converter</b>	
Voltage source:	24 V
Output:	RS232 port
Connected probes:	Ambient pressure transducer Temperature Relative humidity $\Delta p_{VK}$ (Pressure in stabilization chamber)
<b>ADA2 A/D, D/A converter</b>	
Voltage source:	24 V
Output:	RS232 port
Connected probes:	$p_{diff}$ (Pressure drop in the venturi) Analog out (0...10 V) for the frequency regulator

The A/D–D/A system (see properties in Table 3.1.) read out the probes and controlled the RPM of the fan by means of a frequency regulator through an RS–232 port. Using the probe information, the velocity could be calculated with Eq. (3.1). An additional USB A/D–D/A converter (type NI–6008 USB) was mounted to read the volume flow rate of the injected water and to set the frequency regulator of the water supply pumps of the nozzles. A PID–controller was programmed to continuously control the RPM of the pumps according to the required volume flow rate. The PID–controller of the pumps was a part of the wind tunnel control software, programmed in LabView®. Properties of the electric motor can be found in Table A.1 on page 126.

The ambient pressure  $p_\infty$  was measured by a PTB–100–A pressure transducer (properties are summarized in Table 3.2). It is a Si–capacitive absolute pressure transducer, with high accuracy and durability. The pressure (800...1060 hPA) could be read out through an analog output of 0...5 V.

The converging part before the measurement section of the wind tunnel could be assumed as a venturi. Thus, the mean velocity was determined from the

**Table 3.2:** Main properties of the pressure transducer and the hygro-thermometer.

<b>Pressure transducer – Type 3.1158.00.073</b>	
Measuring range:	800 ... 1 060 hPa
Electric output:	0 ... 5 V
Temperature range:	−40 ... + 60°C
Humidity range:	non-condensing
<b>accuracy</b>	
Linearity:	±0.25 hPa
Hysteresis:	±0.03 hPa
Reproducibility:	±0.03 hPa
Calibration error:	±0.15 hPa
Total accuracy at 20°C:	±0.3 hPa
<b>Hygro-thermometer – Type: 1.1005.54.161</b>	
<b>Humidity</b>	
Electric output:	0 ... 10 V
Measuring range:	0 ... 100% relative humidity
Deviation:	±2% rel. humidity (5 ... 95%)
Setting time:	< 90 s
<b>Temperature</b>	
Electric output:	0 ... 10 V
Measuring range:	−30 ... 70°C
Deviation:	±0.2 K
Setting time:	< 90 s

standard working principles of a venturi, using two pressure transducers (type SETRA) with the parameters presented in Table 3.3:

$$U_a = \sqrt{\frac{2\Delta p_{diff}}{\frac{p_\infty}{T R_h}}}, \quad (3.1)$$

where the specific gas constant of the humid air is calculated using

$$R_h = \frac{R_a}{(1 - \varphi \frac{e^*}{p_\infty})(1 - \frac{R_a}{R_v})}, \quad (3.2)$$

with

$$e^* = 610.78 \exp\left(\frac{17.08085 \vartheta}{234.175 + \vartheta}\right). \quad (3.3)$$

The properties of humid air were computed as already described in Section 1.3. All required values for these equations are measured by means of the previously described sensors of the wind tunnel.

**Table 3.3:** Main properties of the SETRA pressure transducers.

Typ:	SET-D239-2KP-U
Measuring range:	0 ... 2 kPa
Electric output:	0 ... 5 V
Accuracy:	$\pm 0.14\%$

### Pulsating flow

Using the software developed to control the wind tunnel, it was possible to change the velocity in time, using a periodical (e.g., sinusoidal) fluctuation. The response function of the velocity of the wind tunnel was, however, different from that of the input voltage function of the electric motor (see Fig. 3.6). For low frequencies ( $f < 0.1$  Hz), except from the phase shift, a good response function was obtained (Fig. 3.6).

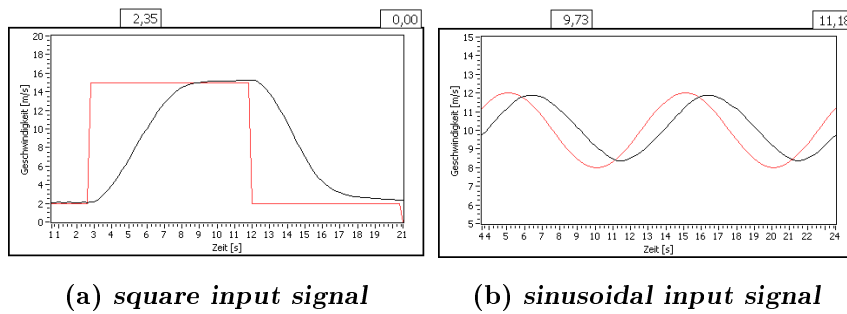


**Figure 3.6:** Measured velocity at the entrance of the wind tunnel test section for different **input voltage** functions vs. time during pulsed operation.

Using this feature, the velocity fluctuation could be increased in a controlled manner, which was useful to reach the targeted values for fluctuations and dissipation rate  $\varepsilon$ . Turbulence levels are characteristically moderate in cumulus clouds, with a turbulent kinetic energy (TKE) in the order of  $1 \text{ m}^2/\text{s}^2$ . This means typical fluctuation velocities around  $0.8 \text{ m/s}$ . The dissipation rate varies by several orders of magnitude in turbulent clouds but is still relatively small ( $\varepsilon = 0.01 \dots 0.1 \text{ m}^2/\text{s}^3$ ) compared to many engineering flows. It would be appropriate to obtain similar properties in the test section of our wind tunnel for the different configurations discussed next.

## 3.2 Generation of controlled structures and turbulence properties

The experiments discussed in this work were based on four different configurations, with various properties: **M1** – without any turbulence modification; **M2** – with a passive grid; **M3** – with a bluff body and **M4** – with both grid and bluff body and a dual spray configuration (see Figs. 3.7 and 3.8). The passive grid applied in **M2** was a rectangular one, with a grid size of 25 mm and rod thickness of 5 mm (Fig. 3.7). The solidity ratio was 36%. The bluff body in **M3** was a cylinder with a diameter of 20 mm (Fig. 3.7), fixed at the height of  $z = +90$  mm perpendicular to the main flow, 150 mm upstream of the measurement section (see also Fig. 3.2 on page 43).

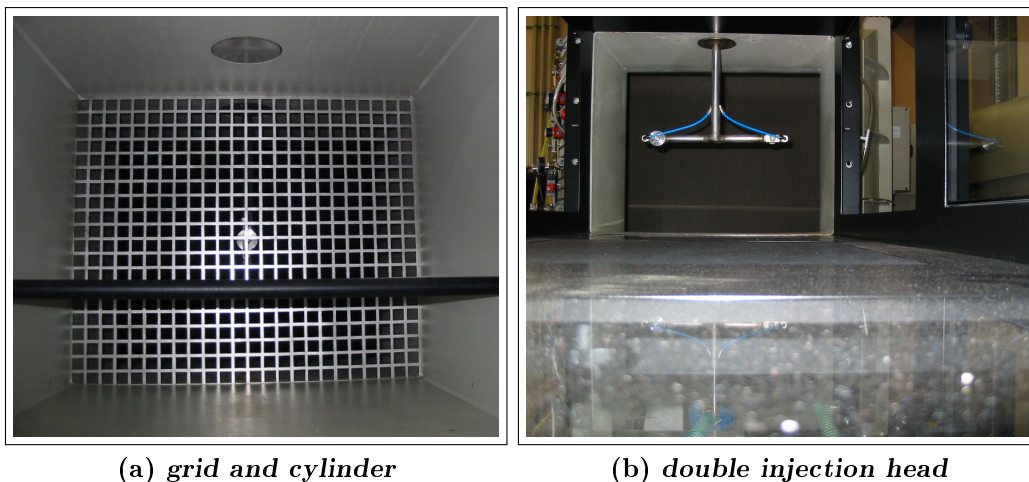


**Figure 3.7:** Photos of the grid, of the cylinder and of the dual spray injection mounted in the test section of the wind tunnel.

All measurements carried out here were optical and non-intrusive so that the flow was not influenced by the measurement instruments.

In the measurement section different measurement planes were investigated: three perpendicular ( $x = 0, 200$  and  $400$  mm) and one parallel ( $y = 0$ ) to the main flow direction, as shown in Fig. 3.2 on page 43. The first plane ( $x = 0, 540$  mm downstream the entrance of the test section) was measured particularly thoroughly, since this is the most important one to set boundary conditions (flow inlet) for associated numerical simulations (Bordás et al., 2011b).



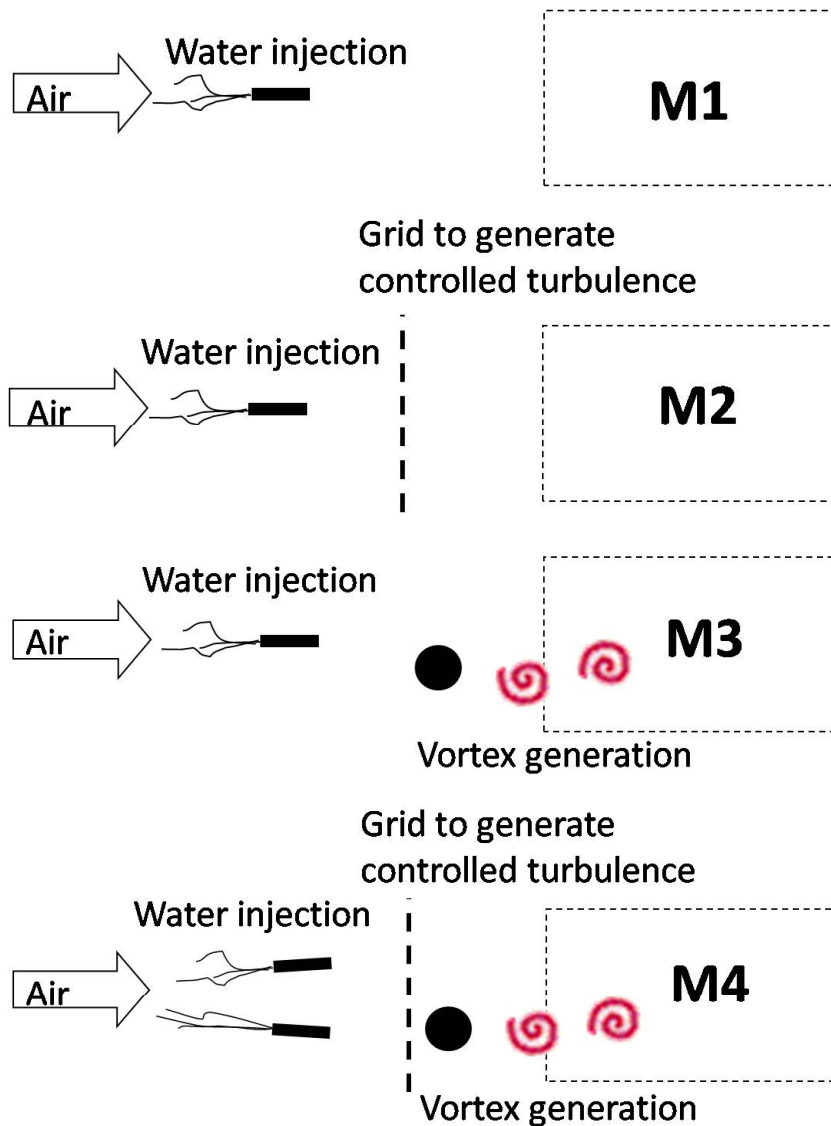
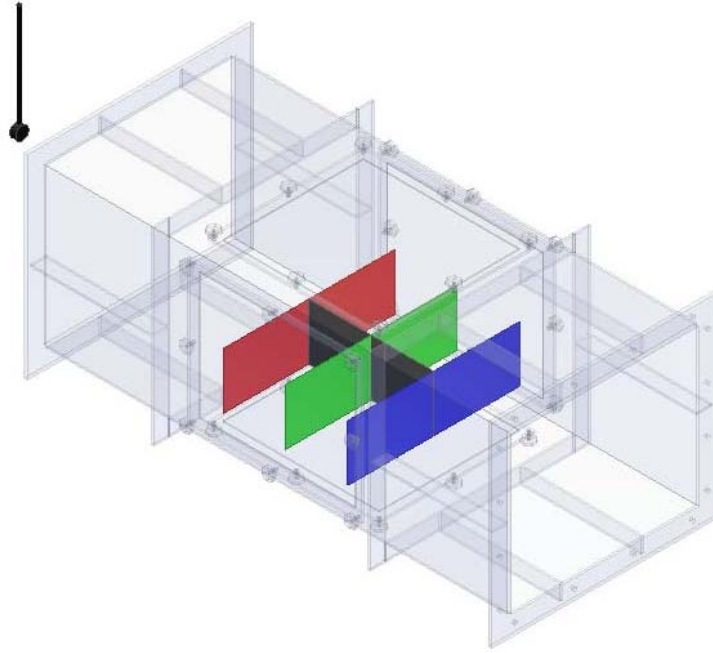


Figure 3.8: Schematics of configurations M1–M4, respectively.

### 3.2.1 Configuration M1 – Without turbulence modification

The configuration **M1** was the basic configuration, without any turbulence modification. However, the spray injection still occurred in counter flow direction, thus generating higher velocity fluctuations compared to a pure air flow. The measured mean velocity of the air flow in this configuration was



**Figure 3.9:** Configuration M1.

$U = 2.45$  m/s. The Reynolds number calculated with the hydraulic diameter of the wind tunnel was

$$\text{Re} = \frac{U d_H}{\nu} = 8.7 \cdot 10^4, \quad (3.4)$$

The measured fluctuation of the air flow velocity in main flow direction is  $u' = 0.25$  m/s. With this, the calculated mean turbulence intensity is 10.9%. The mean kinetic energy of the flow is:

$$k = \frac{3}{2} \overline{u'^2} = 0.09 \text{ m}^2/\text{s}^2, \quad (3.5)$$

assuming isotropy. The length scale characterizing the largest eddies is assumed to be  $l = \frac{1}{6} d_H \cong 0.1$  m, deduced from the boundaries of the energy-containing range of the turbulent cascade (Pope, 2000) and involving the hydraulic diameter  $d_H$  of the wind tunnel. With that, the turbulent Reynolds number can be calculated:

$$\text{Re}_l = \frac{u' l}{\nu} = 2000. \quad (3.6)$$

The dissipation rate of the turbulent kinetic energy can be estimated using theoretical relations (Sreenivasan, 1995):

$$\varepsilon = \frac{k^{3/2}}{l} = 0.287 \text{ m}^2/\text{s}^3 . \quad (3.7)$$

The smallest time scale of the fluid turbulence, the Kolmogorov time scale

$$\tau_K = \left(\frac{\nu}{\varepsilon}\right)^{1/2} = 7.31 \cdot 10^{-3} \text{ s} \quad (3.8)$$

can be defined with the help of the fluid viscosity and of the average rate of turbulent energy dissipation per unit mass. The associated microscale is the Kolmogorov length scale

$$l_K = \left(\frac{\nu^3}{\varepsilon}\right)^{1/4} = 3.35 \cdot 10^{-4} \text{ m} , \quad (3.9)$$

which is the smallest length scale in a turbulent flow.

For the complete characterization of a fluid flow it is important to define further the Taylor length scale and turbulent Reynolds number. The Reynolds number calculated by means of the Taylor scale  $\lambda_g$  can be written according to Voth et al. (2002)

$$\text{Re}_\lambda = \frac{u' \lambda_g}{\nu} = \left(\frac{15u'l}{\nu}\right)^{1/2} = 120 , \quad (3.10)$$

where  $\lambda_g$  could be estimated using (Pope, 2000):

$$\lambda_g = \sqrt{10} l_K^{2/3} l^{1/3} = 7.08 \cdot 10^{-3} \text{ m} . \quad (3.11)$$

The previously calculated values are based on theoretical assumptions. They will be compared later in Chapter 5 with those that could be measured.

### 3.2.2 Configuration M2 – Passive grid

The main objective of the configuration **M2** (Fig. 3.8) was to generate as far as possible homogeneous isotropic turbulence in the test section of the two-phase wind tunnel, with well defined fluctuation velocities, kinetic energy, dissipation rate and turbulent scales, approaching the conditions in clouds.

These typical values could be found in the literature, e.g., in [Shaw \(2003\)](#) or in [Pruppacher and Klett \(1997\)](#).

The most significant variables that also determined the turbulent scales were the turbulent kinetic energy (TKE) and its dissipation rate  $\varepsilon$ . The typical Kolmogorov length ( $l_K \cong 10^{-3}$  m) and time ( $\tau_K \cong 10^{-2}$  s) scales can be calculated from the energy dissipation rate and the kinematic viscosity of air, which is in the order of  $\nu = 10^{-5}$  m<sup>2</sup>/s. To achieve these values a square mesh grid was the most appropriate, which should be mounted upstream the test section of the wind tunnel. In the literature it was found that this kind of grid was an effective tool to create the required flow conditions. However, to plan the proper geometry, a relatively high effort was necessary as discussed next. The results of these estimations remained questionable, as they were based on homogeneous inlet velocity distribution.

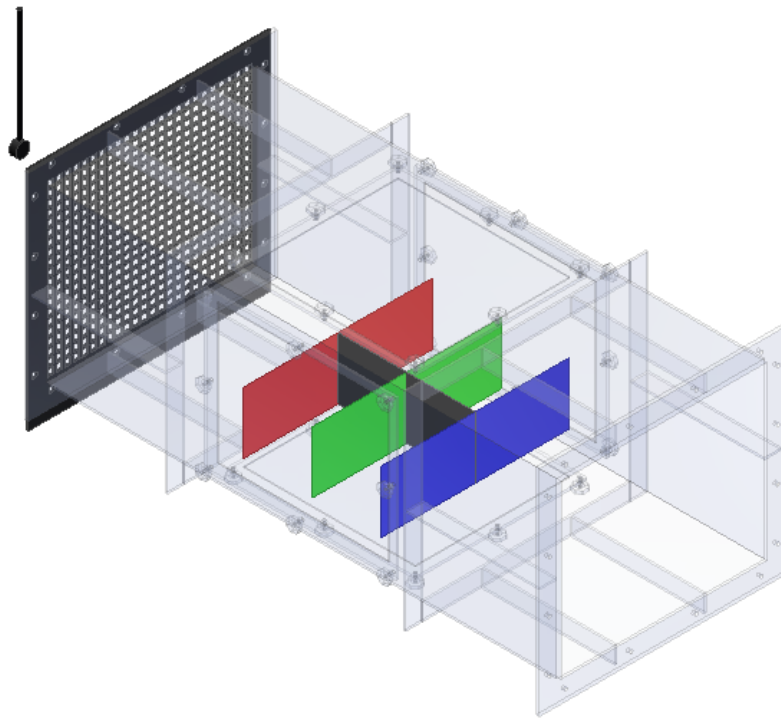


Figure 3.10: Configuration M2.

#### Turbulent kinetic energy and its dissipation

Homogeneous and isotropic turbulence and its decay are regarded as one of the fundamental problems of fluid dynamics and has been the subject of extensive theoretical and experimental studies for most of the last century. Ex-

periments usually studied grid-generated turbulence in wind tunnels as it decayed downstream (e.g., [Mohamed and Larue \(1990\)](#); [Mydlarski and Warhaft \(1996\)](#); [Comte-Bellot and Corrsin \(1966\)](#)). Homogeneous, isotropic turbulence is found when each of the three fluctuating velocity components are invariant during an arbitrary rotation of the principal axis ([McComb, 1992](#)):

$$\overline{u'^2} = \overline{v'^2} = \overline{w'^2}, \text{ while } \overline{u'v'} = \overline{v'w'} = \overline{u'w'} = 0. \quad (3.12)$$

Homogeneity indicates that mean properties do not vary with absolute position in a particular direction. The additional restriction to isotropy implies independence of orientation as well as independence of position in the fluid.

The skewness of the velocity

$$S(u) = \frac{\frac{1}{n} \sum_{i=1}^n (u_i - U)^3}{\left(\frac{1}{n} \sum_{i=1}^n (u_i - U)^2\right)^{3/2}} \quad (3.13)$$

can be used as the main indicator for the homogeneous isotropic turbulence as it was described in the work of [Mohamed and Larue \(1990\)](#). It is the statistical indicator for asymmetry or tendency for a particular fluctuating value to be greater or less than the mean. In theory the value of skewness should approach zero in homogeneous isotropic turbulence.

It is well known that decaying grid turbulence leads to different regimes ([Skrbek et al., 2000](#)). For small wave numbers the turbulent energy spectrum,  $E$  is generally considered as being in the form of

$$E(N_\lambda) = A N_\lambda^2, \quad (3.14)$$

where  $N_\lambda$  is the wave number and  $A$  can be assumed to remain constant ([Stalp et al., 1999](#)). For large wave numbers the relation for the velocity field can be written, according to the Kolmogorov–Obukhov–Corrsin argument ([Warhaft, 2000](#)):

$$E(N_\lambda) = C \varepsilon^{2/3} N_\lambda^{-5/3}, \quad (3.15)$$

where  $C$  is the dimensionless Kolmogorov constant and  $\varepsilon = -dE/dt$  is the energy dissipation rate. The limiting wave number between the two regions is  $N_{\lambda_e}(t) = 2\pi/l_e(t)$ , where  $l_e(t)$  is the energy-containing eddy length scale, around which most of the turbulent energy resides. It is assumed by [Skrbek and Stalp \(2000\)](#) that for homogeneous isotropic turbulence the integral length

scale is equivalent to the energy containing length scale,  $l_e = l$ . As the turbulence decays, the energy containing length scale grows (Von Kármán and Lin, 1987) until it saturates roughly at the size of the channel (Borue and Orszag, 1995) and remains constant thereafter as it was shown by Stalp et al. (1999) as well. Here, it is also proven that the initial energy containing length scale  $l_{e0}$ , is typically much smaller than the size of the channel. The saturation of the energy containing eddies in wind tunnel experiments is unlikely, as the required distance (several meters) is noticeably longer than the test section of most wind tunnels ( $\cong 1$  m). In our case, this can be calculated from the mean velocity in the flow: 2.5 m/s and the saturation time

$$t_s = \frac{11}{5} \left( \frac{d_H}{2\pi} \right)^{5/2} C_{3D}^{3/2} A^{-1/2} \cong 13 \text{ s}, \quad (3.16)$$

using the equation derived from the model described by Stalp et al. (1999). Here  $d_H$  is the hydraulic diameter of the wind tunnel,  $C_{3D} = 1.3$  is the three-dimensional Kolmogorov constant (“prefactor in three-dimensional spectrum” (Sreenivasan, 1995)) and the constant  $A = 3 \cdot 10^{-7} \text{ m}^5/\text{s}^2$ , which is estimated from the energy spectrum, with Eq. (3.14). It comes to  $t_s \cdot 2.5 \text{ m/s} = 33 \text{ m} \gg 1 \text{ m}$ , so that no saturation can be observed in our case.

The turbulent motion is sometimes clearly statistically homogeneous 20 mesh lengths ( $M$ ) downstream of the grid (Hinze, 1975) but a factor of 40 is considered as a safer limit (Corrsin, 1963). In the case of our wind tunnel experiments, it must be assured that the ratio is between 20 and 80, as also chosen by Antonia et al. (1998). The lower limit was also confirmed to be adequate by the measurements of Mohamed and Larue (1990), using the calculated skewness. The downstream length  $x/M$  is the ratio between the axial distance behind the grid  $x$  and the grid mesh  $M$ . The actual measurement section was located between 520 and 1000 mm downstream the grid in the current case. Thus the minimum value of  $x$  is 520 mm. The minimum  $x/M$  value allowed here was 20, with a high probability of homogeneous turbulence, thanks to the selected grid type. The maximum measurement distance was 1000 mm, where the ratio should not be higher than 80. So the grid mesh should be between  $\frac{1000}{80} < M < \frac{520}{20}$ , i.e.,  $12 < M < 26$  mm.

There are standard sizes available on the commercial market, with the following mesh sizes: 25, 20, 15, 14 mm, all in the mentioned region. The Reynolds numbers based on the mesh length  $Re_M$  and the values required to calculate it are summarized in Table 3.4, for a mean velocity of 2.93 m/s, corresponding to the configuration **M2** (Table 3.6).

**Table 3.4:** Main properties of the considered passive grids. The finally selected one is marked as bold.

Grid size $M$ [mm]	Rod thickness $d_r$ [mm]	Solidity ratio $\sigma$ [-]	Mesh Re-number $Re_M$ [-]	Minimum distance $x/M$ [-]	Maximum
14	3.2	0.40	2 672	37	71
15	5.0	0.56	2 863	35	67
20	5.0	0.44	3 818	26	50
<b>25</b>	<b>5.0</b>	<b>0.36</b>	<b>4 772</b>	<b>21</b>	<b>40</b>

The mesh with  $M = 15$  mm was excluded, since its solidity ratio is not in the proposed region of 0.34 to 0.44 (Mohamed and Larue, 1990) and a higher solidity value would possibly lead to instabilities (Comte-Bellot and Corrsin, 1966). The grid with  $M = 25$  mm was finally selected, because it should lead to the highest velocity fluctuation and thus dissipation rate (see Table 3.5).

In the published literature, nearly homogeneous and isotropic flow is usually assumed to be reached behind a grid, where the created wakes merge together after an initial region of high inhomogeneity and anisotropy. The point of separation on the grid is sensitive to very small changes in the geometry of the intersections, or to surface roughness (Grant and Nisbet, 1956). This is probably why the anisotropy of square grids is much lower than that of other types (Comte-Bellot and Corrsin, 1966). Besides that, when the mesh spacing  $M$  multiplied with the solidity ratio  $\sigma$  becomes larger, the turbulence intensity behind the grid is increased. For these reasons a rectangular grid is preferred here.

As described by Tennekes and Lumley (1972), in the homogeneous and isotropic region the equation for the mean turbulent kinetic energy (TKE) can be simplified as follows:

$$U \left( \frac{dq^2}{dx} \right) = -\varepsilon, \quad (3.17)$$

where  $q^2 = \frac{1}{2}(\overline{u'^2} + \overline{v'^2} + \overline{w'^2}) \cong \frac{3}{2}\overline{u'^2}$  is the TKE per unit mass. The equation can also be written using  $U = dx/dt$  (George, 1992):

$$\frac{d}{dt} \left( \frac{3}{2}\overline{u'^2} \right) = -\varepsilon. \quad (3.18)$$

The validity of Eq. (3.18) has also been checked and a very good agreement was found by [Ducci et al. \(2002\)](#). Nevertheless, it is expected that this form of the TKE equation will yield inaccurate estimates of the dissipation rate ([Mohamed and Larue, 1990](#)), owing to the anisotropy and inhomogeneity near the grid. A second and independent estimate of the dissipation rate,  $\varepsilon$  was obtained using the measured time derivative of the downstream velocity, Taylor's hypothesis and the assumption of local isotropy ([Mohamed and Larue, 1990](#); [George, 1992](#)):

$$\varepsilon = \frac{15\nu}{U^2} \overline{\left(\frac{\partial u}{\partial t}\right)^2} = 15\nu \frac{\overline{u^2}}{\lambda_g^2}. \quad (3.19)$$

Since the flow is not locally isotropic near the grid, this estimate is again expected to be inaccurate in the grid region. Varying the Reynolds number by changing the flow velocity or grid size directly affects the dissipation of TKE and ultimately the location where the flow approaches homogeneity and isotropy. For a fixed grid size, higher Reynolds numbers produce eddy sizes with larger characteristic time scales that decay over a greater period of time. In contrast, decreasing the Reynolds number produces smaller characteristic time scales, which require less time to decay. Based on this argument, it may be implied that the onset of homogeneous isotropic flow is related to the dissipation rate of TKE.

In the work of [Ducci et al. \(2002\)](#) a dimensionless dissipation rate  $\varepsilon \frac{M}{U^3}$  also appears, which is presented in a diagram considering previous works as well. From this the dissipation rate can be predicted for different types of grids.

Other approaches, especially for flows behind a grid where the solidity is considered are published in [Özyilmaz et al. \(2009\)](#). Here a porosity-dependent correction factor motivated by [Laws and Livesey \(1978\)](#) can be found:

$$c_g = \frac{\beta^2}{1 - \beta^2}, \quad (3.20)$$

where  $\beta = (1 - d/M)^2$  is the mesh porosity. The solidity ratio can be written, using the porosity:  $\sigma = (1 - \beta)$ . [Özyilmaz \(2010\)](#) presented another correction built with the mesh spacing,  $M$  and rod diameter,  $d_r$ :

$$c_g = \left(1 - \frac{d_r}{M}\right)^{-2.6}. \quad (3.21)$$



These correction factors can be used to correct the predicted energy dissipation rates due to geometrical properties of the considered passive grids. The two equations deliver correction factors of the same order of magnitude. Since Eq. (3.21) has been recently presented, it is used for the calculations in Table 3.5.

**Table 3.5:** Predicted mean values for the considered passive grids at the entrance of the test section.

Grid size $M$ [mm]	Integral length scale		r.m.s. velocity	(3.7)	Energy dissipation rate	
	(3.24)	(3.25)	(3.23)		$\varepsilon$ [m <sup>2</sup> /s <sup>3</sup> ] with ref. <sup>a</sup>	corrected <sup>b</sup>
14	7.5	8.7	$7.0 \cdot 10^{-2}$	$4.0 \cdot 10^{-2}$	$4.1 \cdot 10^{-2}$	$2.0 \cdot 10^{-2}$
15	7.8	11.0	$7.4 \cdot 10^{-2}$	$3.7 \cdot 10^{-2}$	$4.9 \cdot 10^{-2}$	$1.3 \cdot 10^{-2}$
20	9.1	10.0	$8.9 \cdot 10^{-2}$	$7.2 \cdot 10^{-2}$	$7.1 \cdot 10^{-2}$	$3.4 \cdot 10^{-2}$
<b>25</b>	<b>10.0</b>	<b>9.3</b>	<b><math>1.0 \cdot 10^{-1}</math></b>	<b><math>1.2 \cdot 10^{-1}</math></b>	<b><math>9.3 \cdot 10^{-2}</math></b>	<b><math>6.8 \cdot 10^{-2}</math></b>

<sup>a</sup>from Ducci et al. (2002)

<sup>b</sup>with Eq. (3.21)

### Decay of turbulence

To characterize the turbulence and its decay behind the grid as a function of the distance from the grid divided by the mesh spacing, the following equation can be written according to Taylor (1935):

$$\frac{\overline{u'^2}}{U^2} = A \left( \frac{x}{M} - \frac{x_0}{M} \right)^n, \quad (3.22)$$

with  $x_0$  being the so-called virtual origin. The coefficients  $A$  and  $n$  depend on the properties of the grid, and  $n$  defines the decay of turbulence. In the literature, most of the values for  $n$  are around 1.3 (e.g.: Mohamed and Larue (1990); Zhou et al. (2000)) and the virtual origin  $x_0$  can be assumed to be equal to the  $x$ -position of the grid, possibly plus a few times  $M$ . The value of the coefficient  $A$  is mostly between 0.04 and 0.06. A wind tunnel experiment by Sreenivasan et al. (1980), very similar in dimensions to the existing one in our group, identified the following relations for the energy and the longitudinal integral length scale,  $l$ :

$$\frac{\overline{u'^2}}{U^2} = 0.04 \left( \frac{x_d}{M} - 3 \right)^{-1.2} \quad (3.23)$$

and

$$\frac{l}{M} = 0.13 \left( \frac{x_d}{M} - 3 \right)^{0.4} . \quad (3.24)$$

From Eq. (3.23), the value of the fluctuation velocities can be computed and a value below 0.1 m/s is predicted at  $x = 0$ , where  $x_d = 520$  mm. With Eq. (3.24) the length scale can be calculated at the beginning of the measurement section ( $x = 0$ ), which is around  $l \cong 10^{-2}$  m for the meshes considered in Table 3.4. The length scale should be considerably larger than the maximum diameter of the droplets. This condition is fulfilled here. The integral scale of turbulence generated by different grids has been experimentally measured in the work of Mikhailova et al. (2001). Here, a general equation is given for the calculation of the integral scale depending on the mesh properties:

$$\frac{l}{d} = 1.95 \frac{x}{d_r}^{0.5} \text{Re}^{-0.28} . \quad (3.25)$$

Values predicted by these equations for the grids mentioned before can be found in Table 3.5, considering a mean velocity of 2.93 m/s (Case **M2**).

The two approaches for the calculation of the energy dissipation rate showed a relatively high deviation. However, for the finally selected grid ( $M = 25$  mm) both values are approximately in the right order of magnitude, as observed in clouds ( $\varepsilon \cong 0.001 \dots 0.1 \text{ m}^2/\text{s}^3$ ). Note that the measured values are expected to be different, as these theoretical estimations assume a homogeneous inlet flow, which was not the case in the wind tunnel experiments. Further properties based on theoretical assumptions are collected in Table 3.6 on page 62.

### 3.2.3 Configuration M3 – Bluff body

The configuration **M3** contains, additionally to the configuration **M1**, a bluff body. The cylinder, with a diameter of 20 mm is located horizontally at the height of  $z = 90$  mm, and at  $x = -150$  mm perpendicular to the main flow direction (see layout in Fig. 3.11). The eddy length scale is assumed to be 0.1 m, similar to that of the configuration **M1**.

Measurements were carried out with a main flow velocity of  $U = 2.32$  m/s, corresponding to a cylinder-based Reynolds number of

$$\text{Re} = \frac{U D}{\nu} = 2960 . \quad (3.26)$$

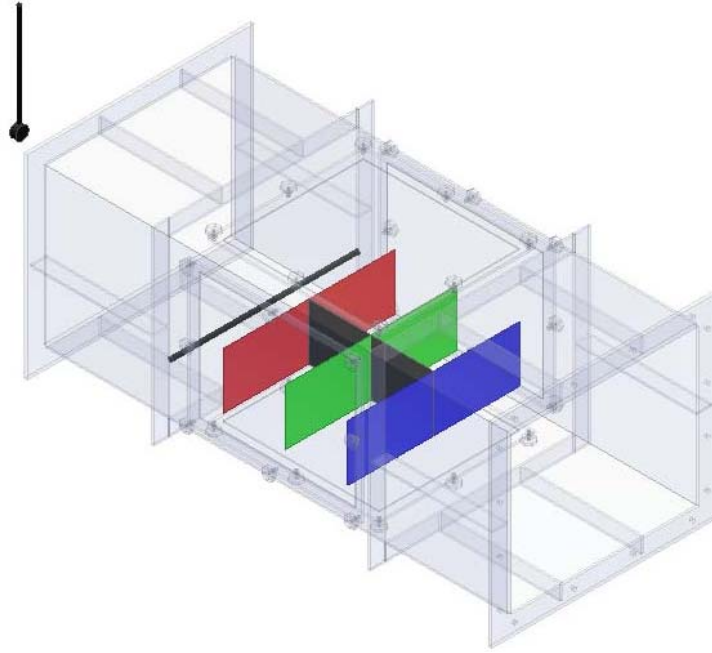


**Figure 3.11:** Configuration M3.

The Strouhal number, or non-dimensional shedding frequency (Norberg, 2001),

$$\text{St} = \frac{f_s D}{U} \quad (3.27)$$

can be used to predict the frequency of the detaching vortices behind the cylinder. The predicted frequency is 24.36 Hz, according to the equation above (using  $\text{St} = 0.21$ , according to Baranyi et al. (2009)). The distance between two shedding vortices is expected to be

$$l_v = \frac{U}{f_s} = 9.52 \text{ cm} . \quad (3.28)$$

The shedding vortices should increase locally the velocity fluctuations and thus may increase the effect of preferential concentration (Shaw et al., 1998). In this way an increased collision rate is expected in the wake of the cylinder.

All calculated properties based on theoretical assumptions are collected in Table 3.6.

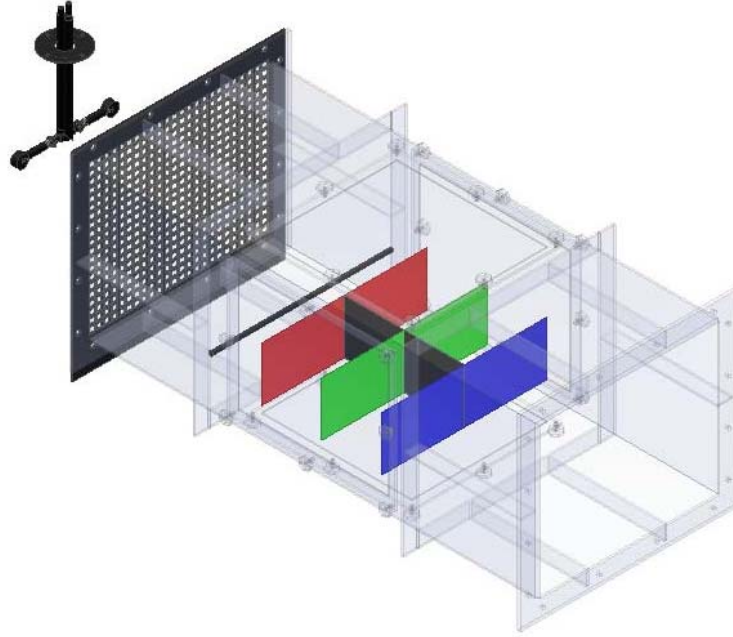


Figure 3.12: Configuration M4.

### 3.2.4 Configuration M4 – Double injection

This configuration contains both the passive grid and the bluff body and additionally an air assisted atomizer in a symmetrical double configuration (both spray heads are installed at the height of  $z = 0$  mm,  $y = -150$  and  $y = +150$  mm, respectively). One atomizer was the same as in case of the configurations **M1**–**M3** and the additional one was a Lechler 154.104.16.14, with  $20^\circ$  cone angle and an orifice diameter of 0.7 mm. The droplets produced by this atomizer are expected to be larger than those of the other atomizer. Each nozzle had an own supply pump allowing to set an individual volume flow rate. The aim of this configuration was besides the simultaneous application of grid and bluff body to create a broader droplet size distribution and increase droplet collision events. The integral length scale is here expected to be smaller than in case of the configurations **M1** and **M3**, because of the smoothing effect of the grid. The eddy length scale is nevertheless chosen to be larger, because of the shedding vortices in the wake of the cylinder. Thus the length scale is assumed to be the diameter of the cylinder  $l = 0.02$  m.

Calculated properties of all configurations are summarized in Table 3.6. Here, the influence of different turbulence modification tools can be noticed.

**Table 3.6:** Summary of theoretically predicted values for the configurations M1–M4.

Property	Cfg. M1	Cfg. M2	Cfg. M3	Cfg. M4
$U$ [m/s]	2.45 <sup>*</sup>	2.93 <sup>*</sup>	2.32 <sup>*</sup>	2.92 <sup>*</sup>
$u'$ [m/s]	0.25 <sup>*</sup>	0.1 <sup>**</sup>	0.33 <sup>*</sup>	0.35 <sup>*</sup>
$k$ [m <sup>2</sup> /s <sup>2</sup> ]	0.09	0.02	0.16	0.18
$l$ [m]	0.1	0.01	0.1	0.02
$\varepsilon$ [m <sup>2</sup> /s <sup>3</sup> ]	0.287	0.068	0.66	3.94
$l_K$ [m]	$3.35 \cdot 10^{-4}$	$4.80 \cdot 10^{-4}$	$2.72 \cdot 10^{-4}$	$1.74 \cdot 10^{-4}$
$\tau_K$ [s]	$7.31 \cdot 10^{-3}$	$1.50 \cdot 10^{-2}$	$4.82 \cdot 10^{-3}$	$1.97 \cdot 10^{-3}$
$\lambda_g$ [m]	$7.08 \cdot 10^{-3}$	$4.18 \cdot 10^{-3}$	$6.16 \cdot 10^{-3}$	$2.68 \cdot 10^{-3}$
$Re_H$	$8.7 \cdot 10^4$	$1.0 \cdot 10^5$	$8.2 \cdot 10^4$	$1.0 \cdot 10^5$
$Re_l$	$2.0 \cdot 10^3$	80	$2.6 \cdot 10^3$	$1.3 \cdot 10^3$
$Re_\lambda$	120	30	130	60

### 3.3 Measurement techniques

#### 3.3.1 LDV/PDA system for velocity and droplet diameter measurements

During this project different non-intrusive optical measurement techniques were applied to determine the properties of both phases. A LDV/PDA system was used to measure the instantaneous velocity of the air and for the instantaneous velocity and the diameter of the disperse phase, respectively. LDV is a well-established technique that gives information about flow velocity. Its non-intrusive principle and directional sensitivity make it very suitable for applications, where sensors with physical contact are difficult or impossible to use. However, it requires tracer particles in the flow. Briefly described, LDV requires that two laser beams cross at their focal point. In the created measurement volume, they interfere and generate a set of fringes. As tracer particles pass through these fringes, they reflect light into a photodetector. By measuring the frequency of the scattered light, the velocity of the tracer particles can be obtained, which is identical with the flow velocity of the fluid in case of suitable tracer particles; fog of PEG, as discussed in Chapter 2.

Main advantages of a LDV/PDA system:

---

<sup>\*</sup> Measured values

<sup>\*\*</sup> from Table 3.5

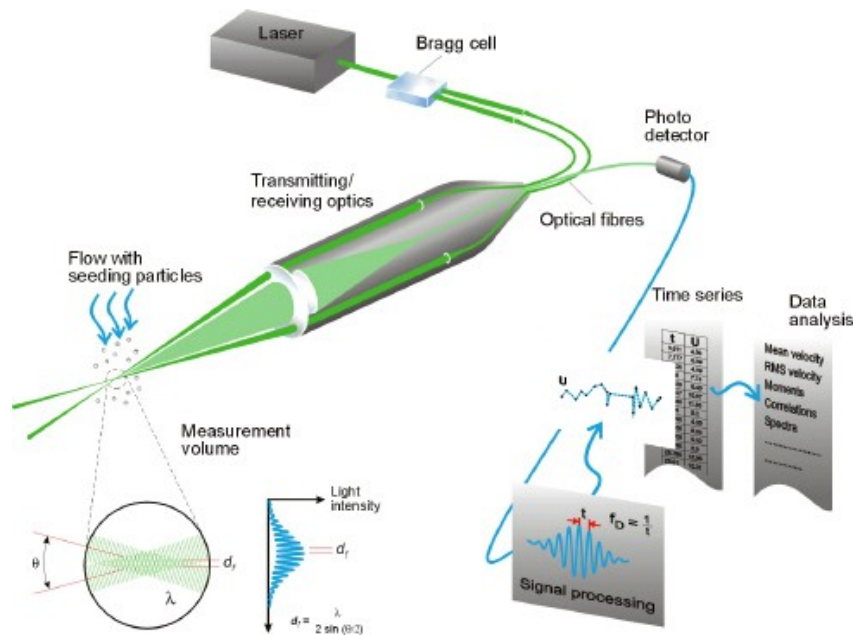


Figure 3.13: Schematic of an LDV system<sup>1</sup>

- non-intrusive measurement,
- high spatial and temporal resolution,
- instantaneous and time-averaged information,
- velocity range from zero to supersonic,
- particle size range from sub-micron up to several millimeters,
- no need for calibration,
- ability to measure in reversing flows.

PDA is an optical technique to measure the size and velocity of spherical particles simultaneously, based on the working principles of LDV. The measurements are performed on single particles, thus allowing detailed analysis of particulate flows. The difference to LDV is in the receiving optics, placed at a well-chosen off-axis location. The scattered light is projected onto multiple detectors. Each detector converts the optical signal into a Doppler burst with

<sup>1</sup>Image from Dantec Dynamics, <http://www.dantecdynamics.com>

a frequency linearly proportional to the particle velocity. The phase shift between the Doppler signals from different detectors is a direct measure of the particle diameter.

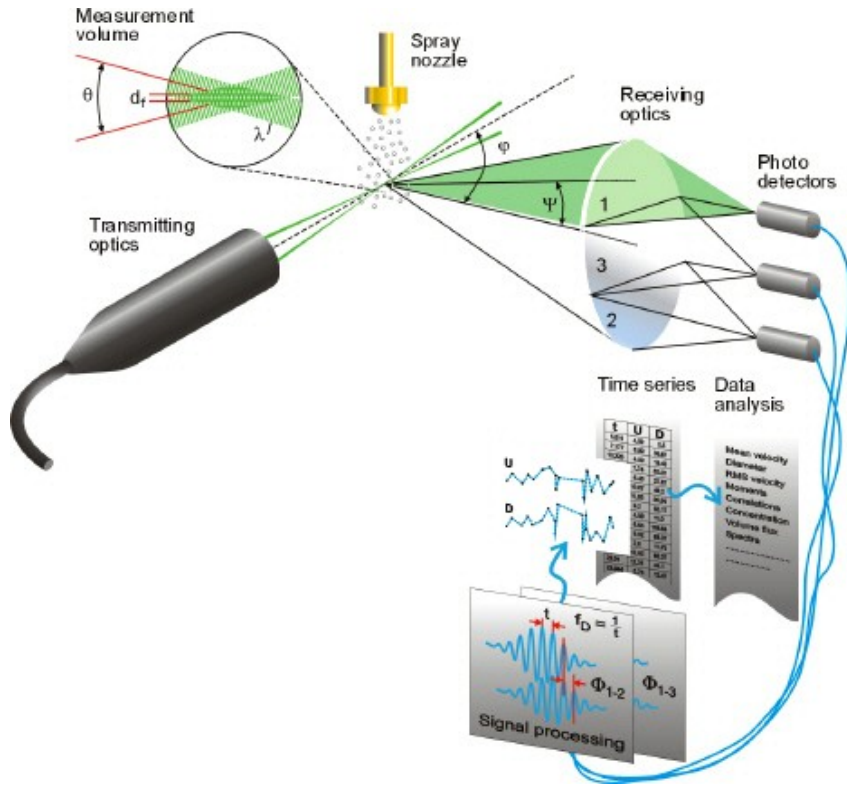


Figure 3.14: Schematic of a PDA system<sup>2</sup>

Working principles of LDV/PDA can be found in detail in the literature (e.g., in Tropea et al. (2007)).

Main properties of the employed LDV/PDA system can be found in Table 3.7. Here, the selected beam power is also listed, which was set according to the hints discussed in Sultan et al. (2000) and in Kapulla and Najera (2006). However, some adaption of the PDA-system was necessary to carry out the measurements in the flows considered in this work.

To improve the measurement quality, the flow and fringe direction should be opposite, where the fringe direction is positive from the shifted to the non-shifted beam. The polarization of the beam pairs were set on the  $U$  (green) channels to parallel, which means that the polarization of the laser beams was parallel with the scattering plane. The scattering plane was defined as the optical axis of the transmitting and receiving optics. In general, the scattering

<sup>2</sup>Image from Dantec Dynamics, <http://www.dantecdynamics.com>

**Table 3.7:** Properties of the LDV/PDA system.

Component	Property	Value
<b>Laser</b>	Type	Ar-Ion, water-cooled
	Output power	6.0 W
	Output wavelength	455 ... 515 nm
	Used wavelength	514.5 nm
	Beam power	$2 \times 250$ mW
<b>Sending Optics</b>	Type	Dantec/2D, 1D used
	Focal length	600 mm
	Beam diameter	1.35 mm
	Expander ratio	2.97
	Beam Spacing	19.5 mm
<b>Receiving Optics</b>	Frequency shift	40 MHz
	Type	Dantec/Fiber PDA
	Focal length	800 mm
	Scattering angle	$160^\circ$
	Scattering mode	2 <sup>nd</sup> order refraction
	Expander ratio	1.00
	Fringe direction	Positive
	Aperture Mask	Mask <b>A</b>
	Phase factor P12	$1.012 \text{ }^\circ/\mu\text{m}$
	Phase factor P13	$0.506 \text{ }^\circ/\mu\text{m}$
Max. diameter	$513.8 \mu\text{m}$	
Effective slit width	0.64	

**Table 3.8:** Hints for PDA settings of different orders of refractions (Dantec Dynamics, 2002).

Order of refraction	Polarization	Preferable angle	Remarks
2nd order refraction	parallel	$143 \dots 148^\circ$ ( $\phi_r + 5 \dots 10^\circ$ )	$150 \dots 170^\circ$ should be avoided, if possible
Refraction	parallel	$30 \dots 75^\circ$ , optimum at $73.5^\circ$	High intensity
Reflection	perpendicular	$83^\circ \dots 115^\circ$ ( $\phi_{c1} \dots \phi_{r3} - 15^\circ$ )	Not for small droplets

angle and the polarization should be selected in a way that the confidence linearity should be over 90% and flat (see Fig. 3.15). Since access to the measurement section of the wind tunnel was limited and both the receiving



and sending optics of the LDV/PDA system should have been traversed, a scattering angle in backward direction ( $160^\circ$ ) was selected. It is generally accepted that PDA measurements in backscatter show limitations (Damaschke et al., 2002). According to the low confidence of linearity (18.43% in this case, due to ambiguities of different scattering orders) this region should be avoided if possible (see hints in Table 3.8). However, preliminary comparisons showed no noticeable deviations both in mean diameter and in spherical validation when comparing forward scatter and backward scatter, so that the previously discussed configuration was systematically used. Nevertheless, measurement

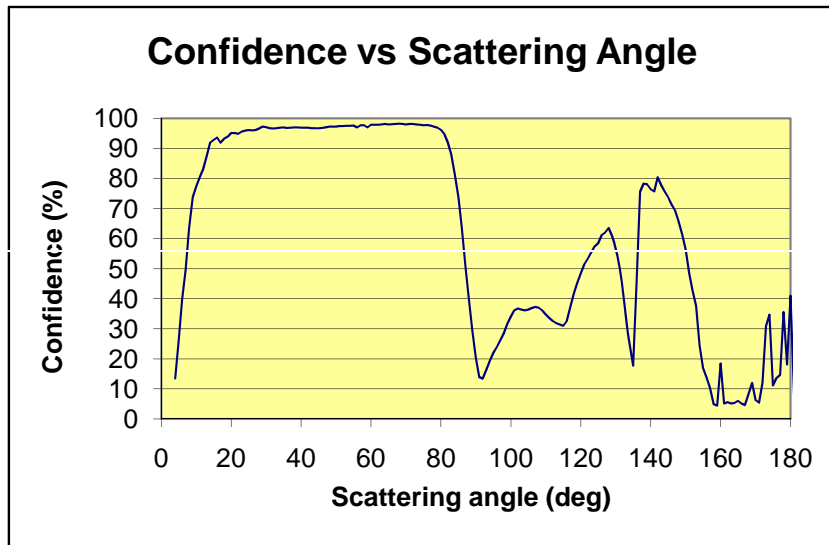


Figure 3.15: Confidence of Phase-Doppler linearity vs. scattering angle<sup>3</sup>

by means of PDA in optically dense sprays is a challenge, as also shown by Sultan et al. (2000), and would require different settings.

### 3.3.2 PIV system for velocity field measurements of both phases

Particle Image Velocimetry (PIV) is an optical method to measure velocity and related properties of fluids. The fluid should be seeded with tracer particles, similarly to LDV. In case of PIV measurements, PEG droplets are used as discussed previously in Chapter 2. However, the number density of tracer particles plays in case of PIV an important role. The main difference between PIV and LDV is that PIV produces two (or three) dimensional vector fields, while LDV measures velocity components at a single position.

<sup>3</sup>Screenshot from the PDA optical configuration plug-in of the BSA software.

To perform PIV analysis on the flow, two exposures of laser light are required upon the camera from the flow (i.e., two images). For recordings, digital cameras using CCD chips are used that can capture two frames at high speed with a few hundred nanoseconds delay between the frames. The frames are then split into a large number of interrogation areas (IA). It is then possible to calculate a displacement vector for each IA with help of signal processing and cross-correlation techniques. This is finally converted to a velocity using the time between laser shots and the physical size of each pixel on the camera. Further details on the PIV method can be found in Adrian (1991). Here, dif-

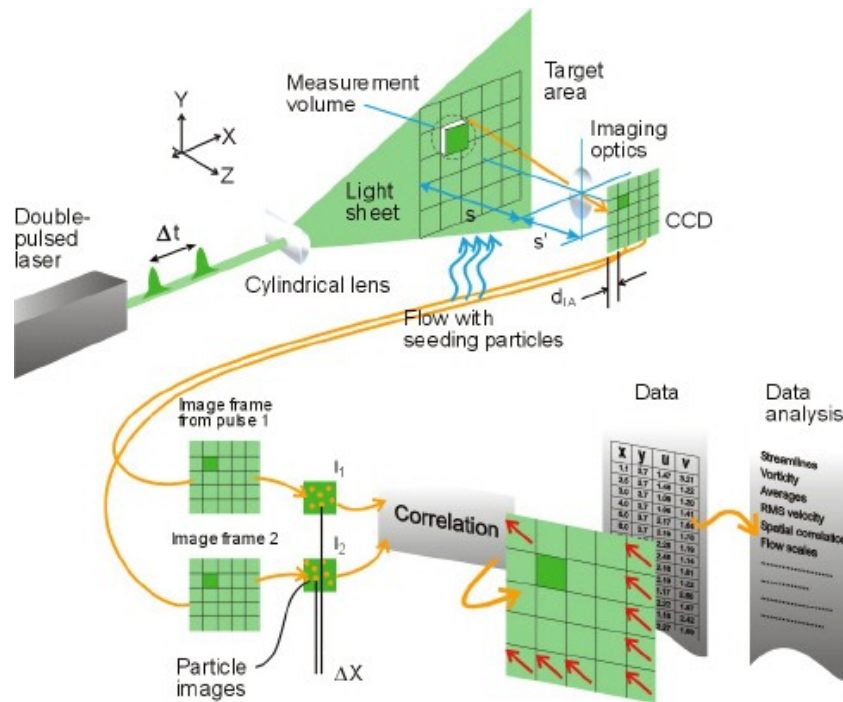
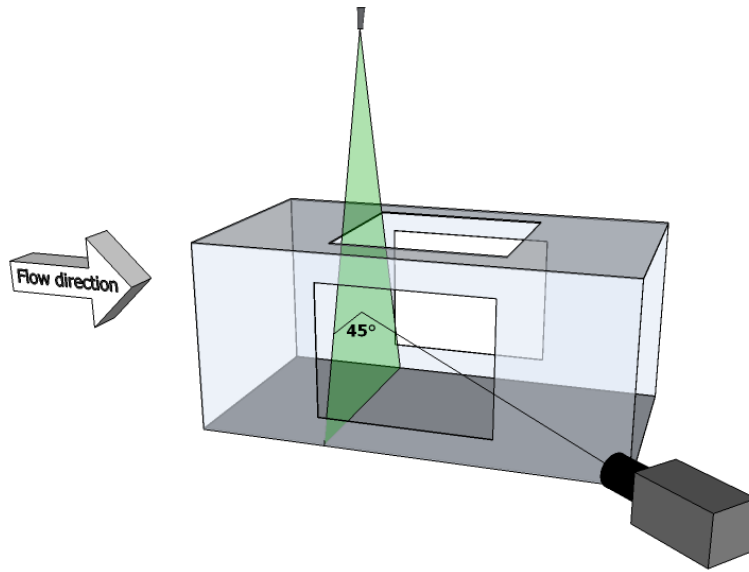


Figure 3.16: Schematic of a PIV system<sup>4</sup>

ferent operation modes like Laser-Speckle-Mode or Particle-Tracking-Mode are also discussed. The current status and development of PIV is summarized by Adrian (2005). The optically transparent windows of the wind tunnel made the non-intrusive PIV measurements possible, as described in the next chapter. Large-field velocity measurements were carried out to determine both transversal and longitudinal velocity components (Bordás et al., 2009; Bordás and Thévenin, 2009) of the disperse and continuous phases. Characteristic for the diagonal PIV measurements was the application of droplets directly as PIV particles and the relatively large angle between the camera axis and the normal of the measurement plane (see Fig. 3.17.).

<sup>4</sup>Image from Dantec Dynamics, <http://www.dantecdynamics.com>



**Figure 3.17:** Sketch of the PIV measurement setup for the measurement in a transversal plane.

The resulting angle between camera axis and normal of the laser sheet was  $45^\circ$ . This angle was imposed by the local conditions at the wind tunnel. The light sheet was perpendicular to the main flow direction.

PIV measurements have been carried out with the system described in Table 3.9. Calibration, evaluation and results are presented in the next chapter. It will also be shown there that a special post processing of the measurement data was needed to get proper results.

**Table 3.9:** PIV hardware components.

Component / property	Description
Laser	Double-pulsed Spectra Physics PIV-200
Laser energy @ wavelength	120 mJ at 532 nm
Repetition rate	10 Hz
Beam transmission	High power Dantec light guiding arm with LaVision sheet optics ( $f = -20$ )
Camera	Double frame Dantec FlowSense 2M
Resolution	$1\,600 \times 1\,186$ pixels at 8 bit
Camera optics	1 : 2.8D 60 mm AF Micro Nikkor
Wavelength filter	532 nm

### 3.3.3 Shadowgraphy system for the detection of droplet collision rates

Shadowgraphy, applied here for the investigation of droplet–droplet interactions is an imaging measurement method, relying on a CCD–camera, a far–field microscope, and a background illumination (see Fig. 3.18). Using a double frame camera, the velocity values can be determined as well. The employed camera is an Imager Intense camera with a 2/3” CCD–sensor from the Co. LaVision (resolution:  $1376 \times 1040$  pixel; pixel size:  $6.45 \times 6.45 \mu\text{m}$ ) mounted with a Questar QM1 far–field microscope.

The illumination has been provided by a double pulsed Nd:YAG laser (Litron) with a pulse energy of 300 mJ at a wavelength of 532 nm. With the help of the pulsed laser beams a fluorescence disc has been excited to get a homogeneous and powerful background illumination. High intensity is required especially for the case of small droplets and corresponding small measurement volumes.

The camera and the illumination lie on the same optical axis. As the droplets are illuminated from behind, their shadow image is recorded by the camera and the diameter of the droplets can be obtained with the help of a previously calibrated  $\mu\text{m}/\text{pixel}$  value (Bordás et al., 2006; Kapulla et al., 2006).

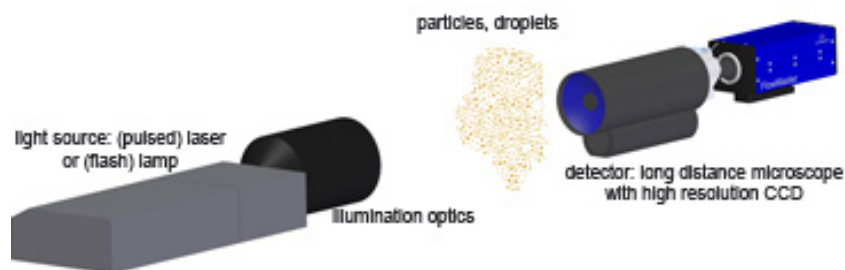


**Figure 3.18:** Schematic of a Shadowgraphy system<sup>5</sup>

Since the expected collision rate is usually moderate in disperse flows, and considering that the recording frequency of the applied laser/camera–system is limited to 10 Hz, measurements leading to meaningful statistics must be carried out for a long period of time at a given position.

The standard postprocessing of the recorded images has been conducted using the commercial Shadowgraphy software DaVis 7.2 (LaVision). The settings listed in Table 3.10 and hardware properties given in Table 3.11 have been used during batch processing.

<sup>5</sup>Image from LaVision, <http://www.lavision.de>

**Table 3.10:** Batch processing settings in DaVis.

Property	Value
<b>Intensity correction</b>	
Mean value	3 000 counts
Threshold for droplets	1 700 counts
<b>Set above/below constant</b>	
Lower level	2 000 counts
Upper level	3 000 counts
<b>Particle recognition</b>	
Global threshold	30%
Low level threshold	30%
High level threshold	50%
AOI expansion	50%

**Table 3.11:** Shadowgraphy hardware components.

Component	Property	Description
Camera	Imager Intense, double frame	Co. LaVision
	Chip size	2/3" CCD
	Resolution at 12 bit	1 376 × 1 040 pixels
	Pixel size	6.45 × 6.45 μm
	Max. recording rate	10 Hz at max. resolution
Camera optics	Questar QM1	Co. LaVision
	Far-field microscope	
Illumination	Double-pulse Nd:YAG Laser	Litron 300
	Laser pulse energy at 532 nm	300 mJ
	Max. repetition rate	15 Hz
	Beam transmission	High power mirrors, co. CVI Melles Griot
	Fluorescence disc	co. LaVision

## Conclusions

This chapter has introduced the setup used for the later described experiments. In the first part, the two-phase wind tunnel with its control and injection system including the developed software has been described. Then, the different configurations **M1**–**M4** used for the generation of controlled flow structures and turbulence have been introduced. The measured and derived flow properties have been summarized. Finally, the applied measurement

techniques were introduced, together with their most important hardware components and software settings.

Optical measurements in such two-phase flows are still highly challenging. Therefore, adaption and improvement were necessary concerning these measurement techniques before being able to carry out meaningful and high-quality experimental measurements, as described in the next chapter.



# Specific adaption of measurement methods

---

For an accurate and quantitative investigation of the flow conditions associated with different configurations in the wind tunnel, a very careful adjustment of the applied optical measurement techniques was required. Therefore, the measurement techniques had to be adapted to these difficult measurement environment. For this purpose the existing post-processing was improved or even completely replaced by our newly developed post-processing tool. These improvements are described in the present chapter.

## 4.1 Laser-Doppler methods

The LDV/PDA measurements and post-processing discussed in this work were first started by means of a commercial software (BSA Flow Software V2.12, from the Co. Dantec Dynamics). However, certain necessary changes to meet our specific needs, could not be taken into account. Therefore, a completely new in-house code was developed in LabView<sup>®</sup> as a complement. In this manner it was possible to simplify and speed up the measurement procedure and to improve its quality.

### 4.1.1 Laser-Doppler Velocimetry

#### Improved traversing and grid generation

One of these specific needs was the interruption criterion during measurements. In the commercial software, there were two conditions to stop the measurement at a certain grid position and to move to the next one

1. the measurement time and
2. the number of acquired samples.



These two conditions were connected by an OR operand. Was the data rate very low or even zero (e.g., near-wall measurements), the measurement time had to be passed, before the traverse was moved to the next position. This led to a significant and unnecessary loss of time. Therefore, the following conditions were implemented in our own LDV-software extension:

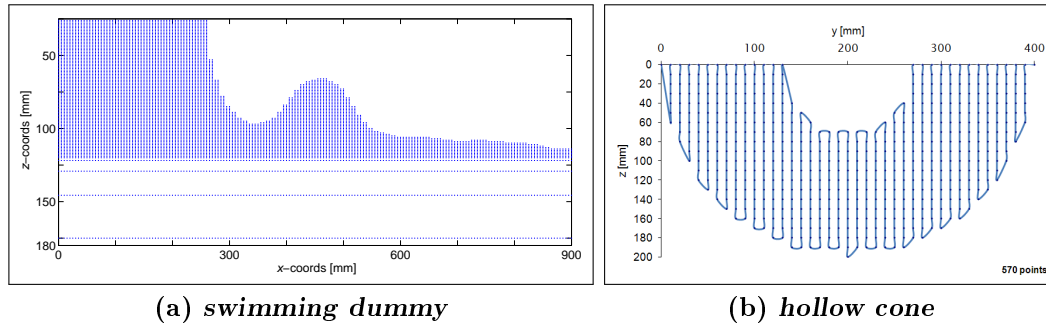


**Figure 4.1:** Exemplary applications of the advanced grid generation tool, left from [Witte et al. \(2006\)](#), right cross section in the wind tunnel.

- Threshold value to define the minimal burst amplitude:** this function could be helpful for such measurements, where the outline of the cross-section was irregular and the generation of the measurement grid was complicated, especially along the wall region of the cross-section, as discussed, e.g., in [Wunderlich et al. \(2007\)](#). An efficient grid generation consisted of creating a rectangular measurement grid including the whole cross-section, or even with a significant number of points outside the cross-section. Using the commercial software, these measurements would have taken an unacceptably long time, waiting for the predefined measurement time to pass at each position. Using our own software extension, grid points associated with insufficient burst amplitude could be identified and excluded almost immediately. Thus, the loss of time was minimized, since the traverse moved very rapidly to the next defined position.
- Minimal data rate:** Nevertheless, it could happen that the burst amplitude did not get below the predefined threshold value (e.g., due to reflections). In this case, the traverse would have stayed at the actual measurement position for the whole preset time, without delivering any result. In order to avoid this problem, the real mean data rate was checked for a time period of 1 second. If the data rate was zero, or below a predefined threshold, the data acquisition was stopped immediately and the traverse moved to the next position.

Applying both conditions simultaneously, the loss of time could be significantly reduced in particular for complex, non-rectangular cross-sections.

A further limitation was the grid generation process. The commercial software could only generate rectangular or cylindrical grids, while our own extension could handle arbitrary geometrical functions. In Fig. 4.1 a special grid around a swimmer dummy is exemplified, as applied in [Witte et al. \(2006\)](#) for LDV measurements in a water channel.

Furthermore, the direction and sequence of the traversing could be prescribed as well. This was helpful, e.g., for the investigation of sprays where a spherical (or ellipsoidal) cross-section was measured, starting with the middle position and spiraling toward the external wall. In this way the data rate was continuously decreasing (starting with the highest value) and the end of the measurement could be decided during the measurement, when the data rate became insufficient. This add-on can be used independently from the in-house LDV software and the corresponding grid positions can be exported to any further software.

### Measurement of periodic flows

In case of periodic flows phase decomposition is an essential issue. Using phase-locked acquisition, the time resolution of a single period can be significantly increased and the mean value and standard deviation can be determined safer as well (Fig. 4.2).

Using the available commercial LDV software, triggering is only possible with an external TTL-signal. In our own software, a further option was implemented, enabling a software-based in-situ triggering. In this way, the phase decomposition was possible with a defined period time and a phase angle, or with a digital signal and a defined threshold value, e.g., using a measured pressure curve ([Mátrai, 2009](#)). Fig. 4.2 shows an example for a phase-averaged measurement. On the left, the pressure curve is presented, measured by a pressure transducer. A user-defined threshold (red line, still on the left) is then used for the phase-decomposition. The phase time of the velocity is always set to zero if there is a trigger event (threshold value is crossed by a positive edge pressure value). The obtained instantaneous (and from now on phase-decomposed) velocity values are shown in Fig. 4.2 on the right. Finally a curve is fitted on these time/velocity point pairs, representing the phase-averaged mean curve. The standard deviation of the instantaneous values compared to the mean curve is the uncertainty ([Seshadhri et al., 2011](#)).

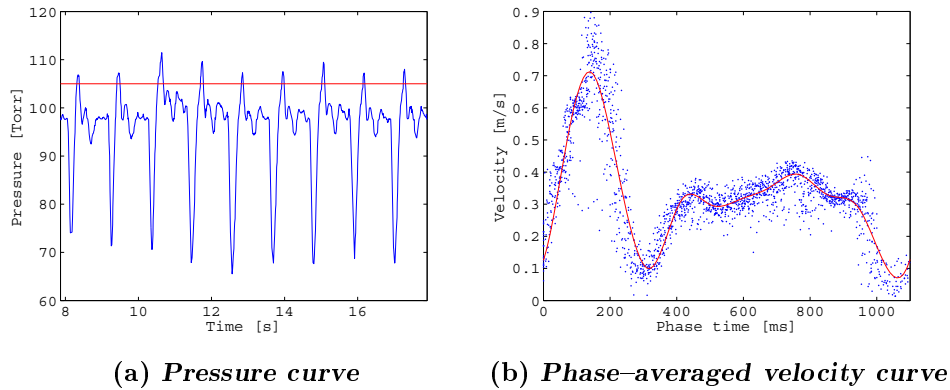


**Figure 4.2:** Example for a phase-averaged measurement in a medical model by means of LDV and a pressure transducer. The threshold for phase-averaging is applied on the instantaneous pressure values. The resulting phase decomposed velocities are presented on the right with a fitted velocity curve.

### Simultaneous Laser-Doppler Diameter and Velocity Measurements

Laser Doppler Velocimetry is generally used to obtain information about local velocities. However, the LDV-signals of particles contain often more information that can be used to determine other properties of the flow as well.

First, signals associated with different particles, such as bubbles or droplets and tracer particles might be distinguished. Thus, we are able to measure simultaneously (but separately) the velocity of both continuous and disperse phases (Bordás, 2005). This distinction is based on the amplitude of the pedestal signal, proportional to the scattered light from a particle passing the measurement volume.

Since the signals in the two-phase flow considered in this work are very similar, as the diameter of the tracer particles and water droplets was in the same order of magnitude, it was not possible to reliably separate the velocity information of air and droplets.

The in-house software extension can be used to carry out simultaneous velocity and size measurements. The principle limitation of LDV (only velocity measurements) can be compensated with a special technique, called LDDV, developed in our group (Wunderlich et al., 2006). The fundamental principle of this special LDV extension lies in the signal characteristics of particles passing through the measurement volume. Due to the fact that a burst can be separated into a low frequency part (pedestal signal) and a high frequency part

(Doppler signal), it provides more than only the velocity information (Wunderlich et al., 2009). The particle size measurement with the new software works in consecutive steps. During these steps the signals are acquired, separated into their pedestal and Doppler parts and evaluated online. Figure 4.3 provides an overview of the signal processing for the velocity and diameter estimation using a commercial LDV system and the complementary, in-house software for LDDV (Wunderlich et al., 2006).

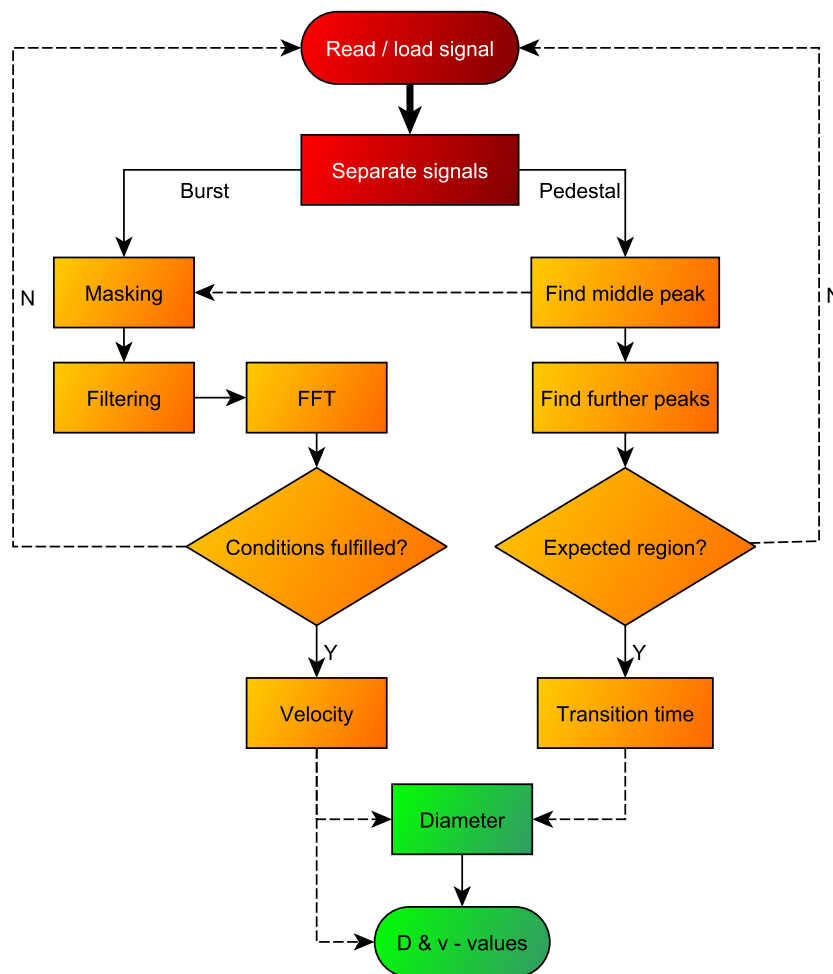


**Figure 4.3:** Flow chart of the LDDV working principle.

The velocity estimation is carried out as usual by means of a Fast-Fourier-Transformation (FFT) and the particle size is determined in a separate way through the LDDV software. The pedestal samples run through a special algorithm, which starts with the definition of a „high threshold“-value. This value is adapted to the maximum signal peak, generated by the reflection

of the passing particle (glance point), which is larger than the measurement volume of the LDV system for this application. From the intersection points of the threshold level on the signal peak, it is possible to find the center of the pedestal signal. Another „low threshold” value is chosen, to get rid of the background noise in the signal. This threshold value should be higher than the noise, but the smallest possible. When a particle larger than the measuring volume flows through this volume, the special structure of the pedestal shows two further signal peaks beside the maximum one. One is located before and one after the signal maximum, respectively, as exemplified in Fig. 4.4.

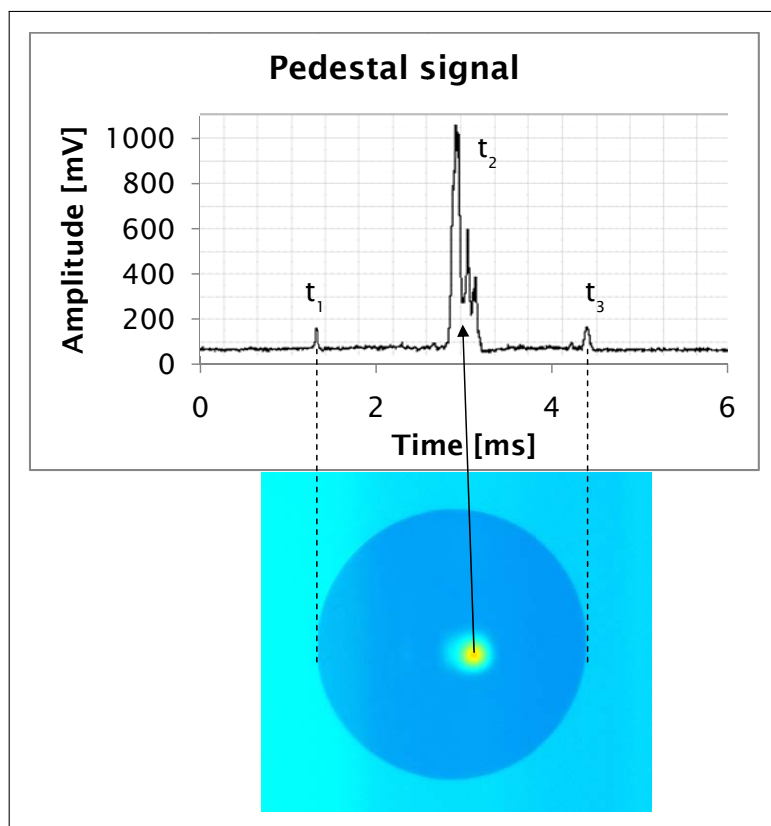


**Figure 4.4:** Typical pedestal signal of a passing droplet.

The two smaller peaks are intersected by the low threshold level. By this procedure, the middle of each peak can be found, which corresponds to two values for a certain time. The middle of the front peak defines the time at which the phase boundary at the front side of the particle (droplet or bubble) enters the measuring volume. This is the starting time  $t_1$ . The peak at the back of the pedestal signal occurs when the phase boundary at the end of the particle leaves the measurement volume. This yields the end time  $t_3$ . From

the difference of the two times one can exactly calculate the transition time  $t_t$  of the particle through the measuring volume:

$$t_t = t_3 - t_1 \dots \quad (4.1)$$

It is then easy to calculate the diameter of the passing particle. Multiplying the transition time  $t_t$  with the velocity  $u$  gives the particle diameter  $d_p$ .

$$d_p = u t_t \quad (4.2)$$

A validation by comparison with other non-intrusive measurement methods (for single droplets by means of Shadowgraphy (Bordás, 2005) and even for spray, generated by a pressure atomizer, by means of both PDA and Shadowgraphy methods (Hagemeier et al., 2008)) was already carried out, with an acceptable accuracy. Since LDDV does not require any additional hardware, it is extremely attractive to obtain simultaneously velocity and particle size.

Unfortunately, there is a practical limitation for the lowest measurable diameter, specified in the LDDV software during the signal processing, associated to the width of the middle peak. Using the LDV-system with test conditions (Hagemeier et al., 2008), the lowest diameter limit that can be measured accurately was found to be around 150  $\mu\text{m}$ . This is suitable for large droplets generated typically by pressure atomizers or sprinkler systems, but not for the droplet diameters considered further in the present conditions.

### 4.1.2 Phase-Doppler Velocimetry

#### Calculation of the droplet concentration

Preliminary measurements showed that droplet number density values, as determined by the commercial software employed at first (BSA Flow V4.10) were considerably overestimated. The values were up to 3 orders of magnitude higher, than the expectation. In the recent literature some newer proposals could be found concerning the correction of the droplet concentration and flux measured with PDA.

Therefore, an additional post-processing of the PDA measurements was implemented by means of a MATLAB<sup>®</sup> script using the previously exported measurement raw data, following the method by Roisman and Tropea (2001). In this publication it is explained that flux and concentration measurements

can exhibit large errors, which can be reexamined to compensate the measurement uncertainty. Here, a simplified description is proposed, which is suitable for our conditions. Let us consider the particle number density  $n$ . During calculations in cloud physics it is one of the most important quantities:

$$n = \frac{1}{t_M} \sum_{i=1}^{N_{sv}} \frac{\eta_{vi}}{A_{\gamma}(d_i, \gamma_i) u_i}, \quad (4.3)$$

where  $d_i$  is the diameter of the  $i^{th}$  drop,  $\gamma_i$  is the particle trajectory angle and  $\eta_{vi}$  is the average number of drops corresponding to a given validated signal.

A proposed algorithm for calculating the drop distribution is also presented in the article of [Hardalupas and Horender \(2000\)](#). First, the average value of the burst length of the class  $k$  should be calculated.

$$\bar{l}_k = \frac{1}{N_k} \sum_{i=1}^{N_k} l_{r,i} \quad (4.4)$$

Here,  $l_{r,i} = u_i \tau_i$ , where  $\tau_i$  is the residence time of a particle in the measurement volume. As PDA-measurements in the present work were carried out by means of a 1D-PDA system, the angle was always  $\gamma_i = 0$ , so the average angle presented in the article has not been calculated. The detection volume should be a non-truncated ellipsoid, which can be checked by the following condition:

$$\bar{l}_k < \frac{2l_s}{3\mu_2 \sin \phi}. \quad (4.5)$$

For these droplets, the largest aperture mask (mask „**A**”) was used with a slit width of 9 mm.  $\phi$  is the off-axis angle, which was set to  $160^\circ$  during all measurements.  $\mu_2 = a_z/a_x \gg 1$  is the ratio of the half axis of the detection volume, which can be represented as an ellipsoid. Depending on whether this condition is fulfilled or not, the diameter of the detection volume  $d_{tk}$  and the reference area  $A_{\gamma_i}$  can be calculated according to the equations presented in Table 4.1.

Now,

- the total number of signals  $N_s$ ,
- the total number of validated signals  $N_{sv}$ ,

- the duration of the signal  $\sigma_i$ ,
- the relative signal presence  $\epsilon = \frac{1}{t} \sum_{i=1}^{N_s} \sigma_i$ ,
- and the relative presence of validated signals  $\epsilon_v = \frac{1}{t} \sum_{i=1}^{N_{sv}} \sigma_i$

are available. With the help of the relative signal presence  $\epsilon$ , the droplet occurrence probability  $p_\lambda$  can be calculated:

$$p_\lambda = -\ln(1 - \epsilon) . \quad (4.6)$$

From here, the total number of drops  $N_d$  appearing in the detection volume in the observation time,  $t_o$  can be calculated using

$$N_d = \frac{N_s}{1 - p_\lambda} . \quad (4.7)$$

Finally, the average number of drops corresponding to a given validated signal  $\eta_{vi}$  can be calculated from the average number of drops corresponding to one signal  $\eta_i$  by multiplying with a correction factor  $r$  according to count errors due to multiple particles occurring in the detection volume or to non-validation of particles:

$$\eta_{vi} = r \eta_i = \frac{2 + \frac{p_\lambda}{\epsilon} \frac{N_d}{t} \sigma_i}{2 \frac{N_{sv}}{N_d} + \frac{p_\lambda \epsilon_v}{\epsilon}} . \quad (4.8)$$

All data are now available to calculate the concentration with Eq. (4.3). Comparative measurements showed that much better results can be obtained using this method (Roisman and Tropea, 2000) instead of the original implementation in the commercial software.

**Table 4.1:** Calculation of detection volume diameter and reference area.

	Condition fulfilled	Condition not fulfilled
Diameter of the detection volume	$d_{tk} = \frac{3}{2} \bar{l}_k$	$d_{tk} = \frac{4}{\pi} \bar{l}_k$
Reference area	$A_{\gamma i} = \frac{\pi \mu_2 d_{tk}^2}{4}$	$A_{\gamma i} = \frac{d_{tk} l_s}{\sin \phi}$



The determination of the probability density function  $n_k(d_k)$  is the key link between experimental data and numerical simulations. The corresponding post-processing was performed again with a MATLAB<sup>®</sup> script, using the previously exported PDA-measurement raw data, and allowing the computation of both the probability density function of the droplet number density ( $n_k(d_k)$ ) and of its standard deviation ( $\sigma_{n,k}$ ). The droplets are divided into classes ( $d_k$ ) with a diameter resolution of 2  $\mu\text{m}$  (freely selectable). The number density is computed separately for each size class using Eq. (4.3). In addition, the number density was calculated for different time scales by dividing the whole acquisition time  $T_{\text{acq}}$  into time intervals  $\Delta t$ . In this manner, the standard deviation  $\sigma_{n,k}$  can be calculated with

$$\sigma_{n,k} = \sqrt{\left( \frac{1}{T_{\text{acq}}} \sum_{j=1}^{T_{\text{acq}}/\Delta t} n_{k,j}^2 \Delta t \right) - n_k^2}. \quad (4.9)$$

The input data for the simulations (as described in [Bordás et al. \(2011b\)](#)) are then the droplet concentration as a function of the droplet diameter, together with the corresponding standard deviation, as exemplified in Fig. 4.5 for the entrance plane,  $x = 0$  mm.

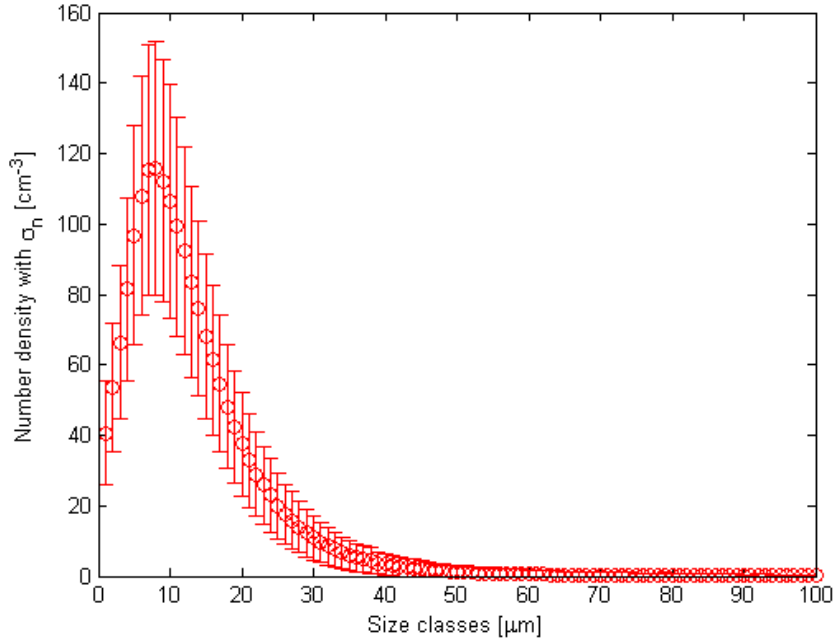


**Figure 4.5:** Probability density function of the measured droplet number density at the entrance of the test section as a function of the size class, including the measured standard deviation as an error bar.

## 4.2 Imaging methods

### 4.2.1 Shadowgraphy

#### Experimental measurement of the collision probability

The accurate determination of collision rates in turbulent flows is an essential task. Theoretical models often do not deliver correct estimations of the results observed in clouds (Xue et al., 2008). For this reason, an experimental, non-intrusive measurement of the collision rate is important to check this issue.

Its experimental determination in the two-phase wind tunnel is based on the Shadowgraphy imaging technique (Bordás et al., 2006; Kapulla et al., 2006). The evaluation process follows a specific algorithm (Bordás et al., 2010), which starts with the user-specific definition of a threshold value (see Table 3.10 on page 70) and the automatic segmentation of the shadow regions on every image. Subsequently, the dimensions of the shadow regions are measured, in particular the smallest and largest axis length values as well as the segmented shadow area. From these quantities a diameter equivalent to the segmented area and the centricity (ratio of minimum to maximum axes) are obtained. The latter one is of central interest to further process and quantify collision events.

Collision events have been identified automatically in this way by batch post-processing of a considerable quantity of single images (typically 10 000) at each position. In order to get finally the collision probability, the resulting number of collision events has been divided by the total number of evaluated droplets during post-processing.

In order to identify collision events, the main idea is to use the centricity of the observed particles, as defined previously. The deformation of the droplets due to aerodynamic forces can be calculated theoretically as a function of the dimensionless Weber number:

$$\text{We} = \frac{u_{p,rel}^2 d_p \rho_f}{\sigma} . \quad (4.10)$$

Considering a linear correlation between the Weber number value and the degree of aerodynamic droplet deformation (Pilch and Erdman, 1987), a correction of the centricity values has been carried out. The correction factor accounts for increased droplet deformation due to oscillations for higher droplet diameters and therefore allows lower centricity values to be accepted as valid

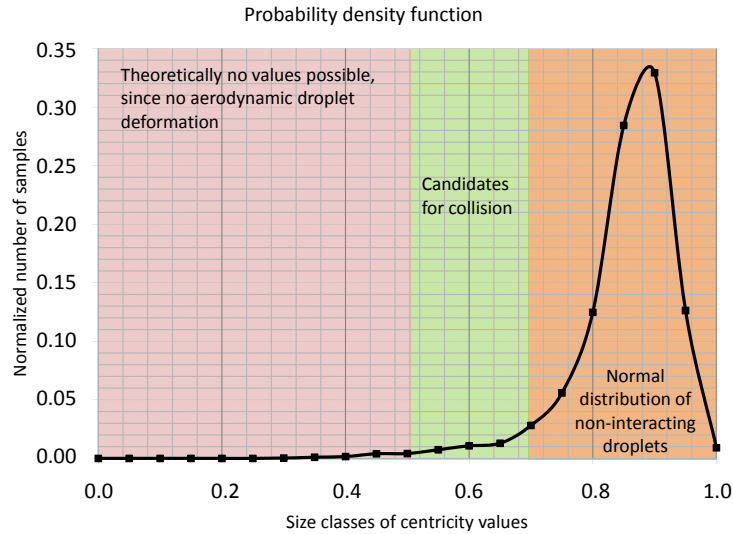


**Figure 4.6:** Distribution of droplet centricity for the configuration **M3** at  $x = 0, y = 0, z = 0$ .

for corresponding conditions. If the centricity falls outside of the tolerance range, this is an indication of a collision event.

In case of small droplets, the Weber number is small as well and there is no significant droplet deformation. As a consequence, the correction procedure described previously is without effect. The axis ratio of a single droplet should again be theoretically very close to 1.0. However, the measured values for centricity return a normal distribution between values of 0.7 and 1.0 (Fig. 4.6). This is due to slightly deformed droplets and even more to measurement uncertainties, in particular associated with the finite pixel resolution. The error induced by discretizing the true droplet boundaries on the pixels and thresholding is particularly important for the smallest droplets.

The probability distribution of the centricity (built using 10 000 images with 0.6 droplet per image in average) is presented in Fig. 4.6 for the configuration **M3** at  $(x, y, z) = (0, 0, 0)$  mm position. In the density distribution function two regions can be recognized, corresponding to droplets with and without collision.

The upper limit for the identification of collision events should be set according to the distribution obtained for non-colliding droplets. In the present case, the corresponding threshold has been set to 0.7, as depicted in Fig. 4.6. As a result of this automatic batch processing, a list of Shadowgraphy images containing promising candidates for collision events is produced. In order to

avoid artifacts and maximize accuracy, these candidate images are examined manually to exclude unsure events.

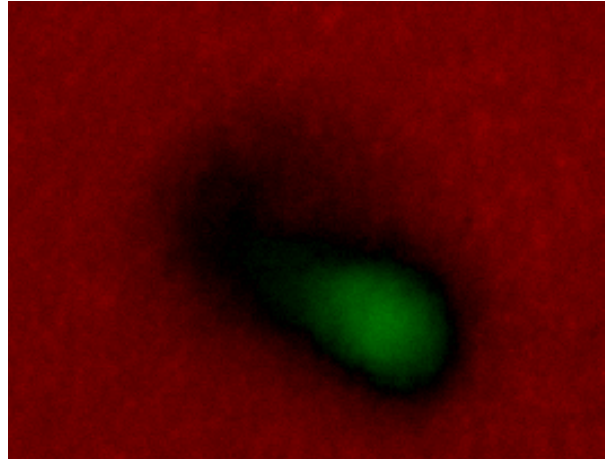


**Figure 4.7:** Example for an unsure collision event: particle partly out of focus.

A typical unsure collision event is exemplified in Fig. 4.7. It is difficult to develop reliable automatic procedures to take care of those. Most of these unsure events are associated with particle(s) not in focus or to two droplets partly hiding each other in the depth of the image. Nevertheless, let us stress that the automatic batch processing is a very efficient and absolutely necessary help to analyze collision events. Typically, less than 50 images must be manually analyzed from 10 000 recorded images. Some exemplary true collision events are presented in Fig. 4.8.

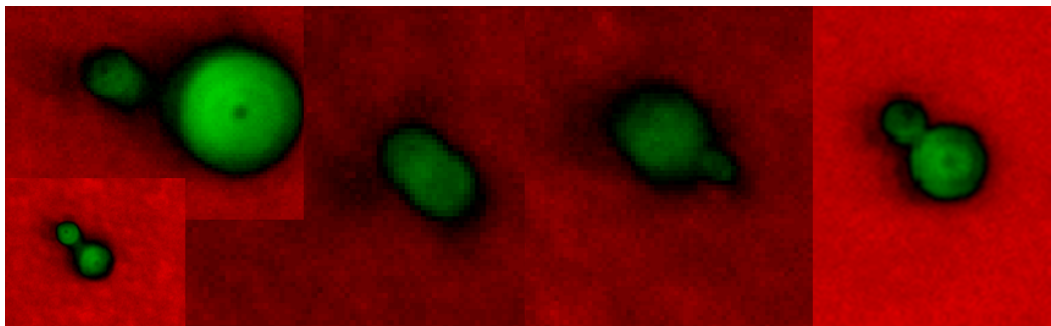


**Figure 4.8:** Some exemplary collision events.

### 4.2.2 Particle Image Velocimetry

There are different error sources influencing the velocity results of PIV measurements, for details see, e.g., [Pap et al. \(2009\)](#). The correction of velocity

vectors of two-dimensional PIV images is often discussed as well. In Tropea et al. (2007), the errors affecting the exact spatial description of the recorded images are considered.

Let us consider a simple case, when the system consists of planar surfaces with a good optical access. For such a case, correction with a linear transformation was already solved by Grant et al. (1994) and is also available in commercial softwares nowadays. The correction is easier when the optical axis of the camera is normal to the light sheet. The authors of this article converted the coordinates, using intercept theorems. For this purpose the distance between lens center and CCD-chip was used.

Nevertheless, in many applications the camera has got a significant angle to the light sheet, thus the light significantly refracts due to the perspective view. Reeves and Lawson (2004) used cross-correlation and a quadratic distortion mapping function to correct perspective errors of their single lens system. It was also found here that the single lens system has significant in-plane-errors, caused by perspective effects.

In case of stereoscopic PIV with more than one camera, such a correction is indispensable (Heineck et al., 2000; Willert, 1997). Scarano (2002) published a review article specially dedicated to iterative methods for processing PIV images. It can be summarized that the various methods only differ in their implementations but are fundamentally similar. Nogueira et al. (1997) presented post-processing steps that could enhance PIV performance. These steps consisted of the detection of erroneous vectors, correction and calculation of derived flow magnitudes, respectively, such as the first spatial derivative, flow divergence or vorticity.

In the following the correction of 2D-PIV measurements of the disperse phase in a two-phase air/droplet flow is described. Velocity components normal to the main flow were measured in the two-phase wind tunnel. It was found that the main flow components were at least one order of magnitude larger than those of the transversal ones. It was furthermore shown that post-processing of the measurement data was indispensable to get proper results, as the angle between the camera axis and the normal of the measurement plane was constrained by the local conditions at the wind tunnel: the used angle was  $45^\circ$ . The light sheet was perpendicular to the main flow direction. Properties of the PIV-system can be found in the previous chapter (Table 3.9 on page 68).

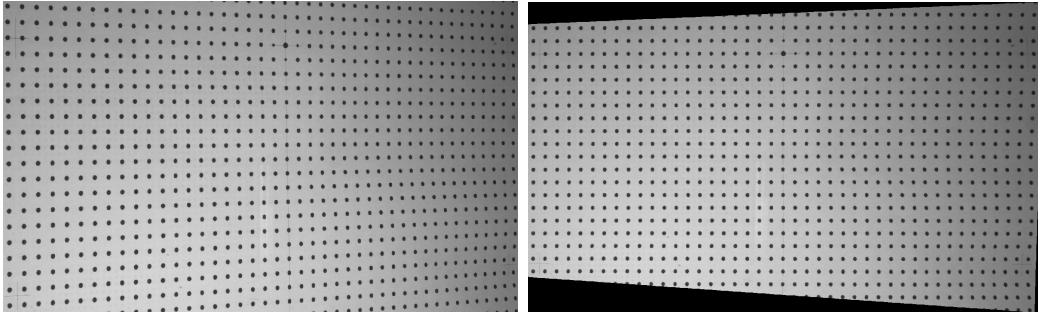


**Figure 4.9:** Recording of the calibration plate (left) and the dewarped image (right).

### Distortion correction

For the calibration, a large-area ( $450 \times 250$  mm) calibration plate with dot pattern (see Fig. 4.9 on the left) has been machined and placed into the test section of the wind tunnel. The diameter of each dot is 3 mm and the distance between the neighboring dots is 11 mm. The origin is marked by a dot with a diameter of 4 mm. Positive and negative  $y$ - and  $z$ -directions are marked by four dots of 2 mm, respectively in each direction. The plate is always aligned into the middle of the plane  $x = 0$ , so that its origin is 630 mm downstream the nozzle, in 250 mm height and 300 mm from each side-wall. Calibration and dewarping of the camera image occurs automatically by the software, whereas a direct linear transformation is applied.

The evaluation of the recorded  $4 \times 250$  double frame images have been corrected at first with the Flow Manager<sup>®</sup> software from the co. Dantec Dynamics with the built-in dewarping tool. This correction should eliminate the error caused by the perspective view. Thereafter an adaptive correlation with an interrogation area of  $64 \times 64$  pixels and an overlap of 75% was carried out. The resulting vector maps were filtered by range validation of the vector components within the range of  $\pm 1$  m/s. Finally, 250 images of each set were averaged and one of the results of the four sets is shown in Fig. 4.10. It can be seen that all original vectors point toward the positive  $y$ -direction, which does not correspond to reality, since it would mean that the flow impacts the back wall of the test section.

To understand the source of error, a schematic drawing is presented in Fig. 4.11 on page 90. The angle between sheet normal and camera axis was  $45^\circ$ .  $d$  was the distance between the camera optics and the middle of the laser plane. On the bottom, the area of interest has been magnified. A tracer in two different moments (1<sup>st</sup> and 2<sup>nd</sup> frame) was marked by  $(X_1, Y_1)$  and  $(X_2, Y_2)$ , respectively.

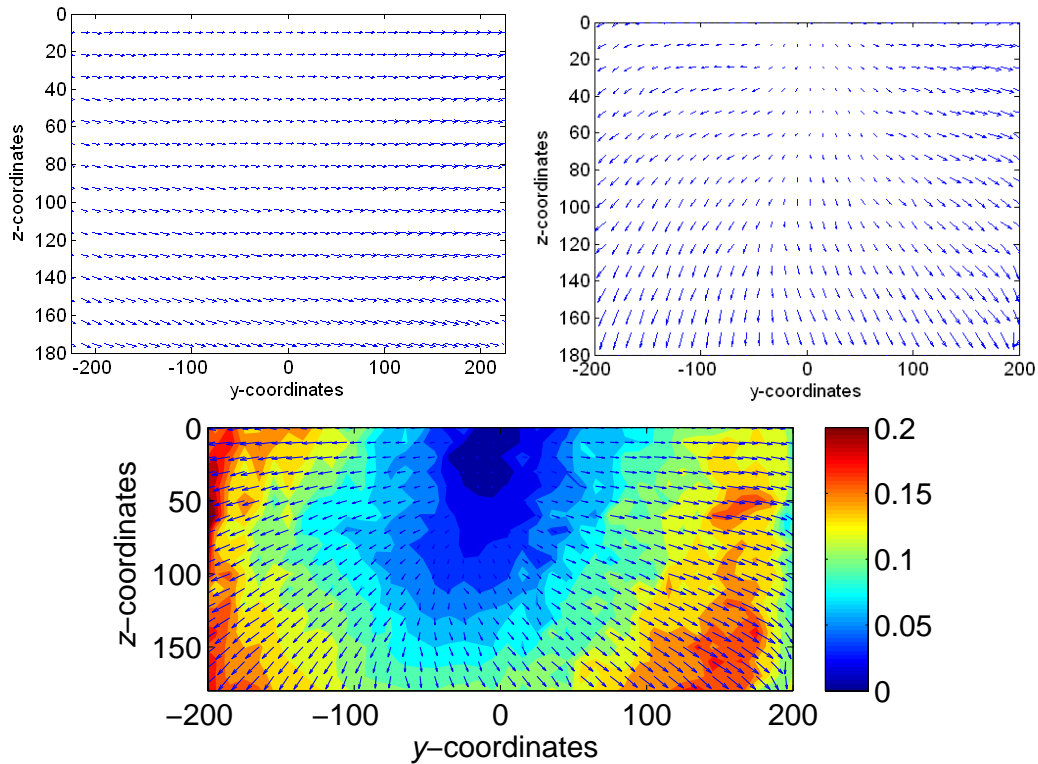


**Figure 4.10:** Averaged vector fields before (top left) and after (top right) correction. The corrected vector field is shown again in the bottom with the same aspect ratio in both coordinate directions and a contour plot in the background with color coding, representing the vector lengths.

Though the marked tracer moves parallel with the channel axis, the resulting vector will have both  $x$ - and  $y$ -components. The applied direct linear transformation corrects the perspective error, the distance between  $(X_{0i}, Y_{0i})$  and  $(X_{1i}, Y_{1i})$ , respectively. The aim of the additional correction described here is to eliminate as well the  $y$ -components in this example. The essence of the correction method is to subtract the projection of the  $x$ -component of the velocity vector (pointing from  $(X_{01}, Y_{01})$  to  $(X_{02}, Y_{02})$  in Fig. 4.11) from the resulting velocity vectors.

This means that complementary velocity information was needed in the main flow direction. Now, a correction was applied using this mean value of the velocities in main flow direction – which was already available from previous LDV measurements, see [www.ovgu.de/isut/lss/metstroem](http://www.ovgu.de/isut/lss/metstroem) and the PIV-vectors were corrected by the projection of those. The LDV measurement information was interpolated such that the velocity information was avail-

able at each interrogation area of the cross-correlation evaluation of the PIV measurements.

The corrected image can be seen in Fig. 4.10 (right). It corresponds to the expected results, demonstrating the high quality of the developed correction process. In this manner, it became possible to measure velocity components transverse to the main flow direction by PIV with a good accuracy.

## Conclusions

This chapter introduced the adaption and improvement of the applied optical measurement methods, from an advanced measurement grid generation and traversing method to the geometrical correction of 2D-PIV images. Most of these improvements were implemented as a post-processing of the raw measurement data. In this manner, further quantities could be derived, such as the corrected droplet number density for different size classes and its fluctuation. The method developed for the experimental determination of collision probability and the derived collision rate was also discussed. The measurement results and the database are now described in the next chapter.



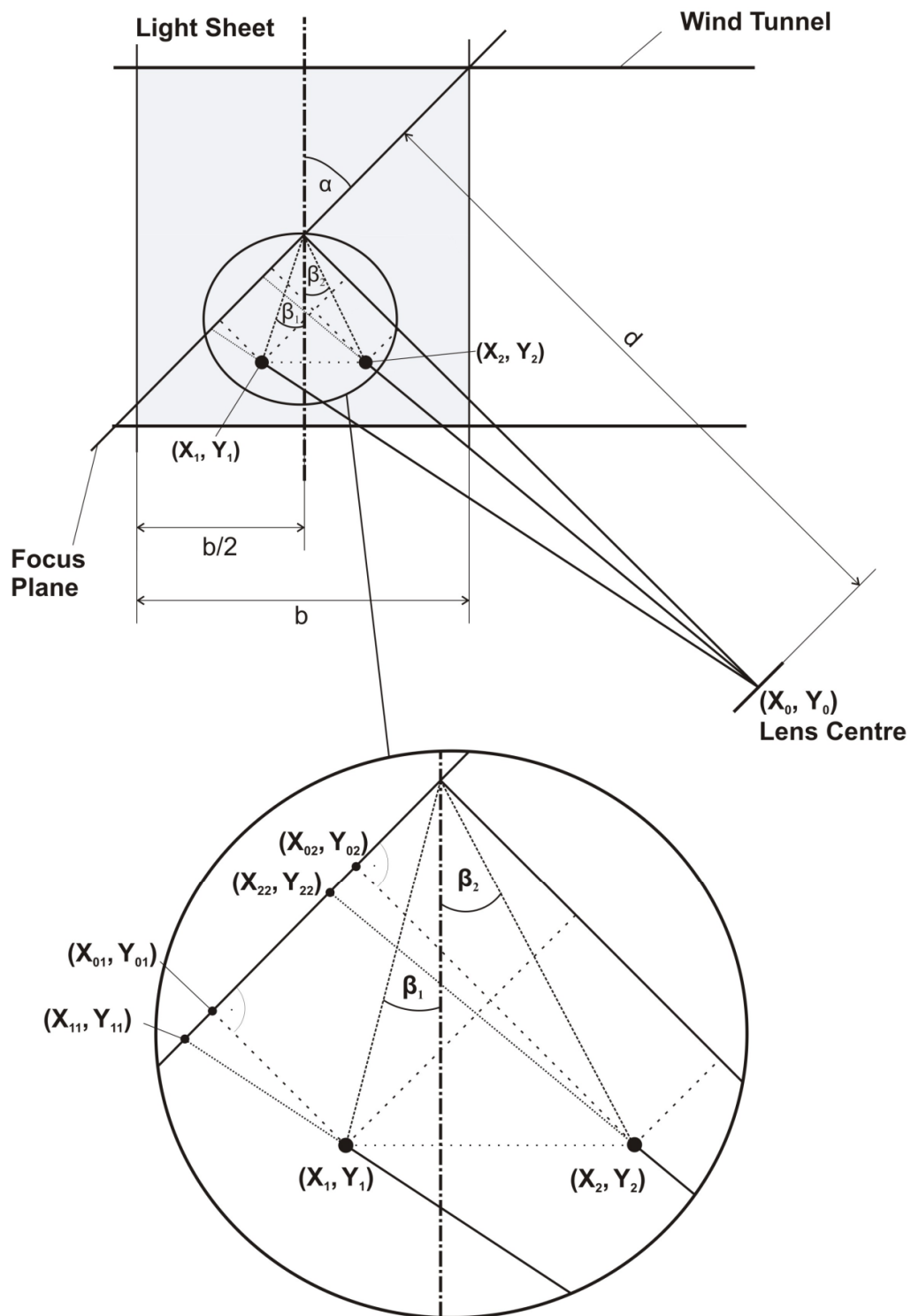


Figure 4.11: Illustration of the distortion, caused by an oblique view on the laser plane.

# Experimental results and analysis

---

In this chapter, the results of the measurements in the two-phase wind tunnel and of the post-processing are presented. Considerably higher droplet collision rates are observed and consequences for rain initiation are discussed. The online database is also introduced briefly, together with the structured experimental data. Finally, companion numerical simulations are discussed. Part of this chapter has been submitted as journal article to *Physics of Fluids* (experimental part) and to *Computers and fluids* (simulations).

## 5.1 Measurement uncertainty and repeatability

### 5.1.1 Measurement uncertainty of LDV/PDA

It is essential to determine and quantify the uncertainty of given measurements. One possibility would be to take another measurement method as reference for the verification of the measured quantities. Another measurement method was indeed available to characterize the particles (Shadowgraphy). However, this method had got a limitation concerning the lowest measurable diameter (about 5  $\mu\text{m}$ ). As a significant number of droplets are expected to be around and even below this value, a direct comparison is not possible.

For this reason a theoretical approach has been used instead. [Kapulla and Najera \(2006\)](#) made a theoretical estimation for the diameter measurement uncertainty by means of a PDA system. According to these calculations, the diameter values could be measured with an error of  $\pm 3.6\%$ . Note that a second, independent PDA system was also available for a short time in our group. Comparing the results from both systems and exchanging systematically single hardware components the deviation concerning particle diameter was indeed found to be around  $\pm 3\%$  in agreement with [Kapulla and Najera \(2006\)](#).

After a systematic inspection of the convergence of the measured data, 10 000 samples were used as condition to finish measuring at the actual position

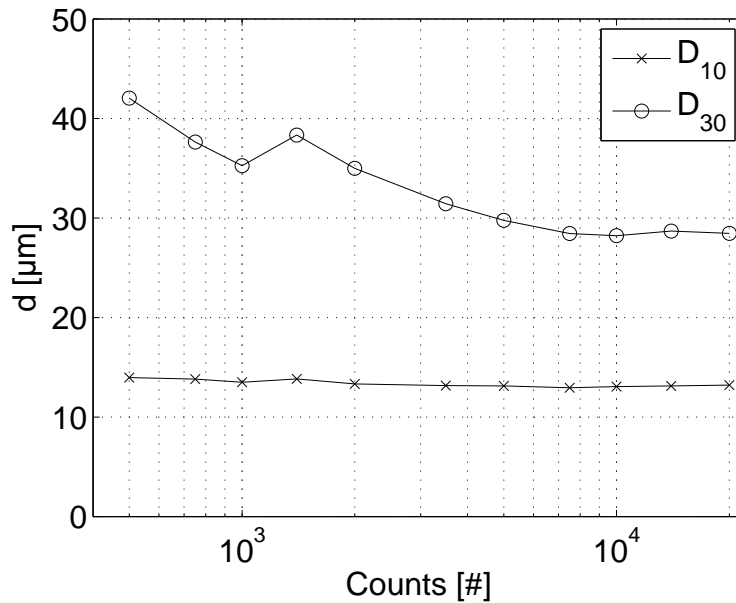


**Figure 5.1:** Convergence of the arithmetic mean and volume mean diameters measured by PDA. The volume mean diameter converges at around 8 000 samples.

with PDA, as shown in Fig. 5.1. From the literature (Lefebvre, 1989), a recommendation of 5 500 samples can be found. In the light of our own results, this value is too low to obtain converged statistics and all results presented afterwards have been obtained based on 10 000 samples.

### 5.1.2 Measurement repeatability of LDV/PDA

Measurement repeatability delivers information on the fluctuations of the measured quantity due to the whole system, including the injection and atomization (air and water pressure fluctuations, temperature influence) additionally to that of the measurement system.

To get information concerning measurement reproducibility and repeatability, some profile measurements have been repeated with the same conditions but on different days. These measurements were influenced both by the fluctuations caused by building the mean value (small time scale) and the long time fluctuations of the system. The statistical error has been calculated with the ratio of the maximal deviation and the mean value, as

$$\frac{\max(|d_{10,i} - \overline{d_{10}}|)}{\overline{d_{10}}} \quad (5.1)$$

for both mean diameters (Fig. 5.2) as well as for mean velocities (Fig. 5.3) at each and every point along a transversal profile. The obtained error was below  $\pm 3.4\%$  and  $\pm 5.0\%$ , respectively.

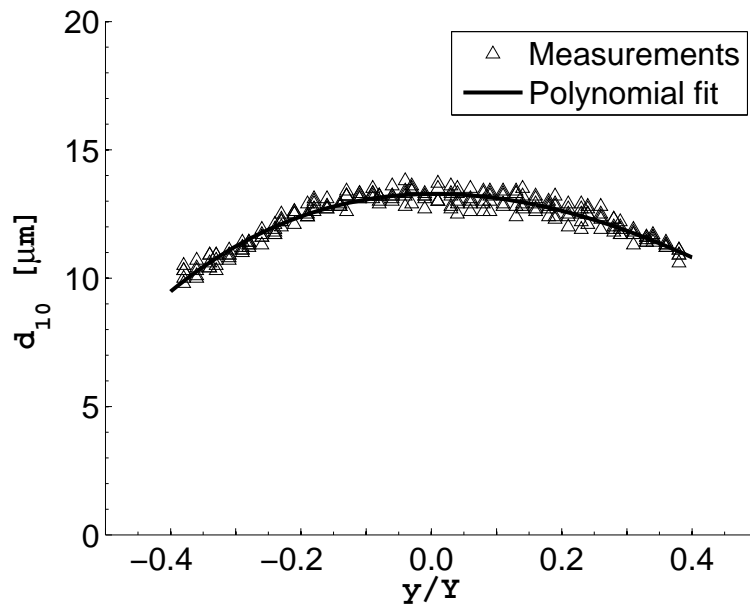


**Figure 5.2:** Mean diameter profile across the measurement section at  $x = 0, z = 0$ , measured by means of PDA.

## 5.2 Measurements of the continuous (air) phase

As the measurements were carried out by means of non-intrusive measurement techniques, tracer particles had to be added to the gas flow. It has already been shown in Chapter 2, how to select appropriate tracer particles for such investigations. Since the disperse (water) phase did not follow exactly the air flow, the velocity of both phases were finally measured separately.

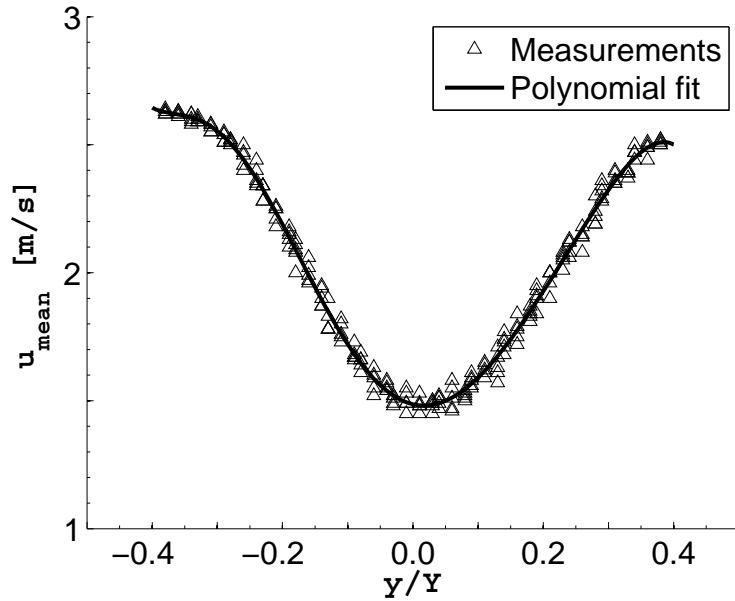


**Figure 5.3:** Mean longitudinal velocity profile of the droplets across the measurement section at  $x = 0, z = 0$ , measured by means of PDA.

### 5.2.1 Velocity measurements

#### LDV-measurements

The velocity distribution of the air phase at the inlet plane ( $x = 0$ ) has been measured by means of LDV. During the measurements of the continuous phase, the nozzle was operating only with air at the same pressure as in normal operation, but without water. In this way, the measurement of the air phase was possible, since the selected tracer particles (fog of PEG) followed the flow accurately (see Chapter 2). The mass flow rate of the air and water in normal nozzle operation was in the same order of magnitude ( $\frac{\dot{m}_w}{\dot{m}_a} = 2.5$ ), thus a very similar flow condition was assured as in case of the droplet injection.

In order to define the locations of the measurement points for the LDV and the PDA techniques, a measurement plane has been generated with 874 (19 in  $z$ -direction and 46 in  $y$ -direction) measurement points, with 10 mm distance in each direction between them.

LDV measurements are capable of a high temporal resolution. Thus, the velocity components measured in the mean flow direction (see Fig. 5.4) included the temporal fluctuations as well. In this way the determination of turbulence intensity was also possible (Fig. 5.6).

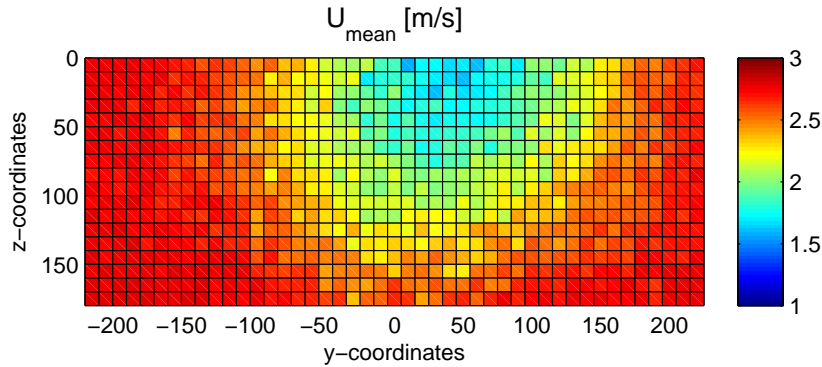


**Figure 5.4:** Mean longitudinal velocity distribution of the air phase at  $x = 0$ , measured by means of LDV.

Both LDV and PIV measurements showed that the other two velocity components (within the cross section of the test section) are at least one order of magnitude smaller than those of the main flow direction, as shown also in Figs. 4.10 and 5.5.

### PIV-measurements

For the air phase a longitudinal plane ( $y = 0$ ) was measured as well by means of PIV. The air flow was seeded by fog of PEG, since these particles were selected previously in Chapter 2. 300 image pairs were acquired with a recording frequency of 15 Hz. After applying a cross correlation method to the raw images, with interrogation areas of  $32 \times 32$  pixels and an overlap of 50%, an average vector field could be determined for the complete  $y = 0$  plane. The resulting 2D-velocity vector field is presented in Fig. 5.5 together with an instantaneous plot.

Here, the vertical velocity ( $z$ ) components were directly measured as well. It could be shown that they are one order of magnitude smaller than those in the main flow direction, in agreement with previous LDV measurements. Furthermore, the energy dissipation rate could also be calculated, with the help of a MATLAB<sup>®</sup> script, as described later.

### 5.2.2 Derived values

The mentioned measurement techniques can only deliver the magnitude of the velocity components (either spatially or temporally resolved). To obtain

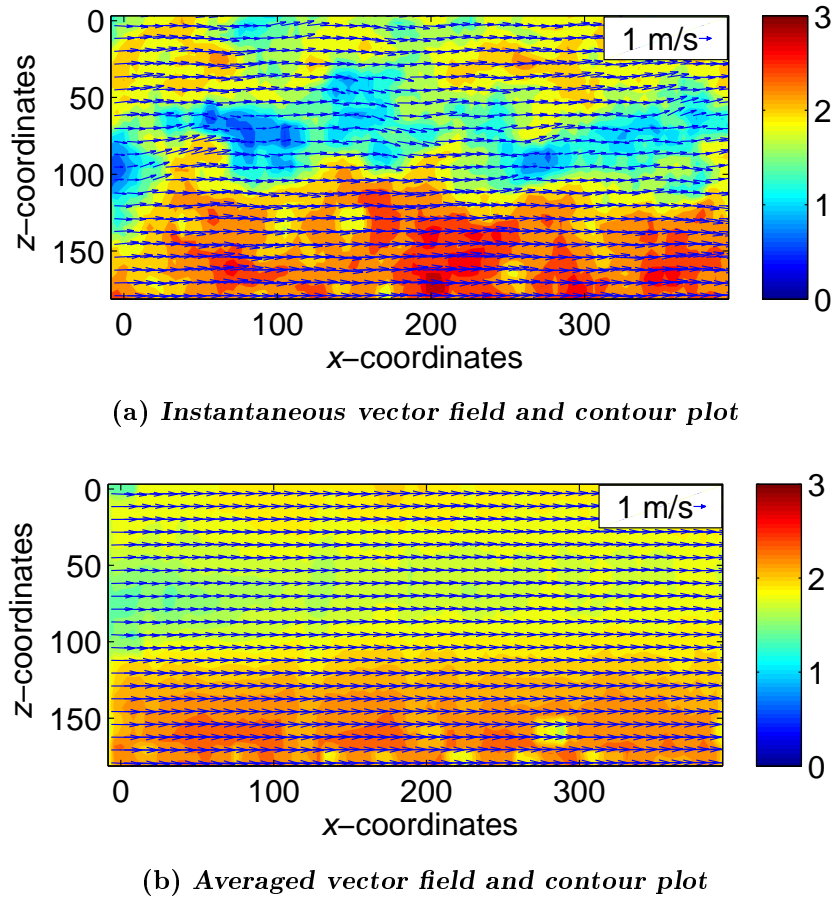


**Figure 5.5:** Instantaneous (top) and averaged (bottom) velocity vector fields and contour plots of the air phase at  $y = 0$  for the configuration **M3**, measured by means of PIV.

further information, post-processing of the measured data is necessary. In the following, the calculated values are presented, deduced from those of the measured ones.

### Turbulence intensity

Due to the high temporal resolution of the LDV measurements, the calculation of the RMS-velocity was possible. From this, the turbulence intensity could be calculated using Eq. (5.2) for the whole measurement plane, with a spatial resolution according to the measurement grid. The distribution of the turbulence intensity for the configuration **M1** at  $x = 0$  is presented in Fig. 5.6.

The turbulence intensity is calculated by the ratio of the RMS velocity and of the local mean velocity for each position of the measurement grid:

$$\text{Tu} = \frac{\overline{u'}}{U} . \quad (5.2)$$

The mean value of the turbulence intensity was around 10%, which is a usual boundary condition for numerical simulations of industrial flows as well. Moreover, the inhomogeneous distribution of Tu visible in Fig. 5.6 was adequate for the investigation of the influence of different turbulence conditions on the local droplet–droplet interactions as discussed later.

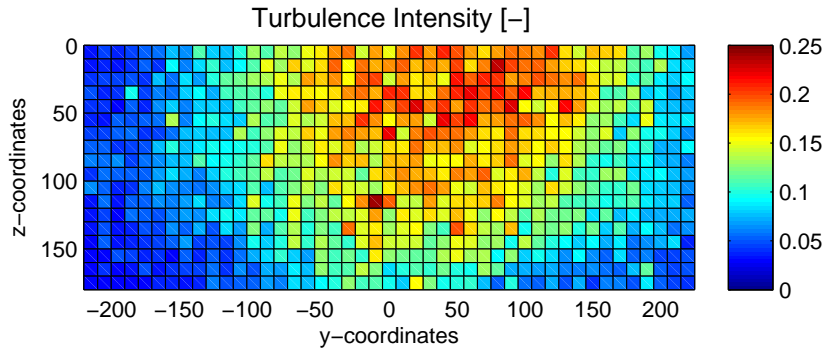


**Figure 5.6:** Mean turbulence intensity distribution of the air phase in  $x$ -direction at  $x = 0$ , measured by means of LDV.

### Turbulent kinetic energy

Assuming isotropy of the velocity fluctuations, the TKE can be calculated using

$$k = \frac{3}{2} \left( \overline{u'^2} \right) . \quad (5.3)$$

The calculated values for all configurations are summarized in Table 5.1 on page 100.

### Energy dissipation rate

Calculation of the energy dissipation rate was based on PIV–measurements, in the longitudinal middle plane ( $y = 0$ ) as shown in Fig. 5.5. The following equation



$$\varepsilon = \nu \overline{\frac{\partial v}{\partial x} \left( \frac{\partial u}{\partial y} + \frac{\partial v}{\partial x} \right)}, \quad (5.4)$$

simplified from that of [Hinze \(1975\)](#) was applied for the two dimensional vector fields of 300 images in each configuration, as described by [Saarenrinne and Piirto \(2000\)](#). The dissipation rate was averaged for every vector field and represented as a histogram. The peak of the normal distribution was determined and the other values outside the Gaussian distribution were finally filtered out, as shown in Fig. 5.7. The resulting mean dissipation rate was in the required order of magnitude, found in the literature. Typical for cumulus clouds are values between  $0.001 \dots 0.1 \text{ m}^2/\text{s}^3$ , according to [Rogers and Yau \(1996\)](#).

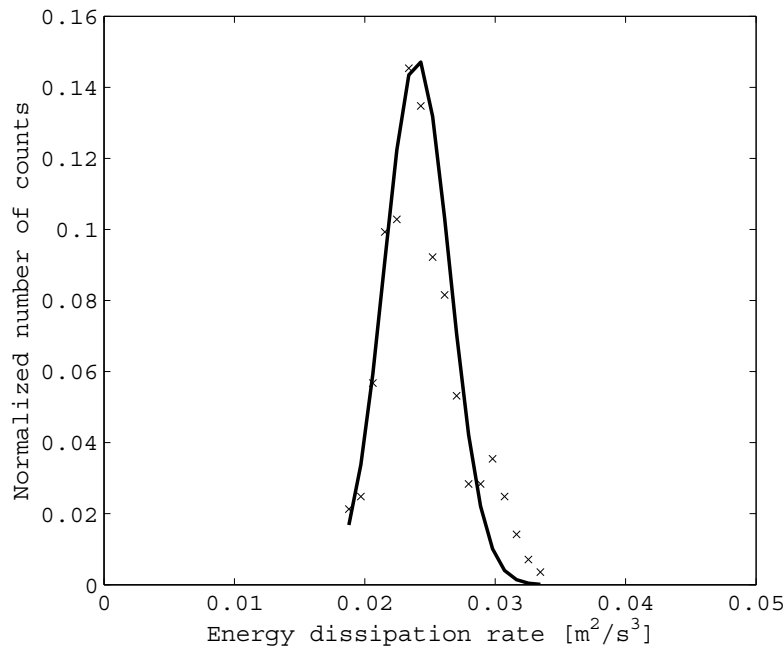


**Figure 5.7:** Distribution of the calculated energy dissipation rate from 300 PIV vector fields in the  $y = 0$  plane.

Another MATLAB<sup>®</sup> script was used to determine the energy cascade of the flow from the PIV vector field, as shown in Fig. 5.8. From this, the longitudinal integral length scale could be calculated and from that the energy dissipation rate (Eq. (3.7)), as a further comparison with the previously calculated values. The results of this second method were in the same order of magnitude and thus showed a good agreement:

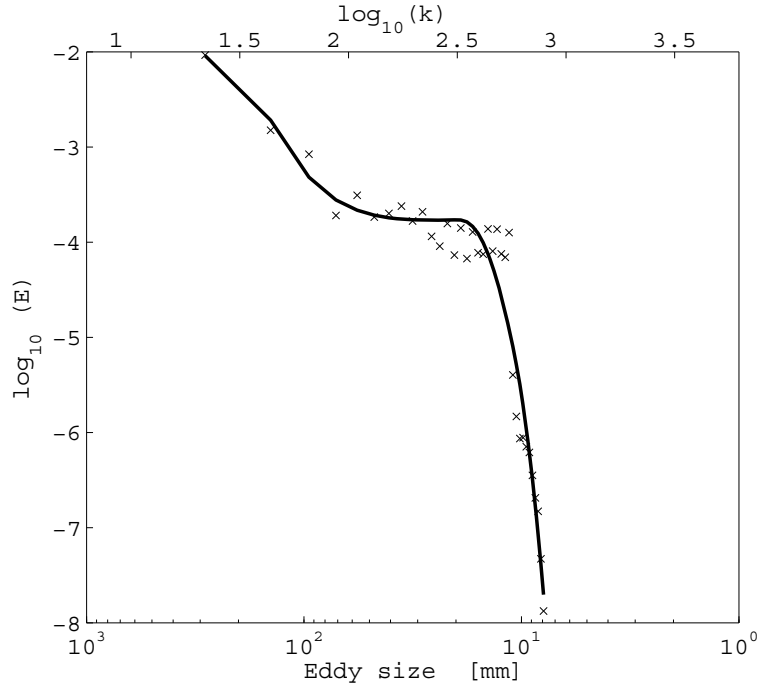


**Figure 5.8:** Calculated energy cascade of the flow. Post processing of a PIV measurement in the  $y = 0$  plane.

Turbulent kinetic energy:	$k = 0.0146 \text{ m}^2/\text{s}^2$
Longitudinal integral length scale:	$l_{11} = 0.0656 \text{ m}$
RMS of velocity fluctuations:	$u' = 0.1710 \text{ m/s}$
Energy dissipation rate:	$\varepsilon = 0.0761 \text{ m}^2/\text{s}^3$

However, the available flow information in the entrance plane ( $x = 0$ ) is more complete and will be used for the calculation of energy dissipation rates in the following. The energy dissipation rate and the deduced turbulence scales are summarized in Table 5.1 for all configurations.

### Turbulence scales

The obtained time scale and length scale for the Kolmogorov (or dissipation) scale can now be calculated by Eqs. (3.8) and (3.9) using the measured energy dissipation rate, determined from PIV measurements, with the help of Eq. (5.4). The values obtained for  $\tau_K$  and  $l_K$  are listed in Table 5.1 and correspond to typical values in cumulus clouds.

**Table 5.1:** Measured and deduced values of the continuous phase for all the configurations in the wind tunnel at  $x = 0$ . The turbulent energy dissipation rates were calculated by means of PIV measurements, as described in this Chapter and the turbulence scales were deduced from those.

Quantity	M1	M2	M3	M4	Cumulus clouds
$U_a$ [m/s]	2.45	2.93	2.32	2.92	1 ... 8
$u'_a$ [m/s]	0.25	0.18	0.33	0.35	$\approx 0.8$
$k$ [m <sup>2</sup> /s <sup>2</sup> ]	0.11	0.05	0.18	0.22	$\approx 1$
$l$ [m]	0.1	0.01	0.1	0.02	100
$\varepsilon$ [m <sup>2</sup> /s <sup>3</sup> ]	$2.5 \cdot 10^{-2}$	$1.2 \cdot 10^{-2}$	$2.6 \cdot 10^{-2}$	$5.5 \cdot 10^{-2}$	$10^{-2} \dots 10^{-1}$
$\tau_K$ [s]	$2.5 \cdot 10^{-2}$	$3.5 \cdot 10^{-2}$	$2.4 \cdot 10^{-2}$	$1.7 \cdot 10^{-2}$	$\approx 10^{-2}$
$l_K$ [m]	$6.2 \cdot 10^{-4}$	$7.4 \cdot 10^{-4}$	$6.1 \cdot 10^{-4}$	$5.1 \cdot 10^{-4}$	$\approx 10^{-3}$
$\lambda_g$ [m]	$1.1 \cdot 10^{-2}$	$5.6 \cdot 10^{-3}$	$4.9 \cdot 10^{-3}$	$9.3 \cdot 10^{-3}$	$\approx 10^{-1}$
$\text{Re}_\lambda$ [-]	170	70	60	200	$\approx 10^5$

### 5.3 Measurements of the disperse (droplet) phase

Properties of the disperse phase have been measured separately from those of the continuous one for each configuration in three transversal ( $x = 0$ ,  $x = 200$  and  $x = 400$ ) and a longitudinal ( $y = 0$ ) plane, of course using the same measurement grid as in case of the continuous phase. [Lefebvre \(1989\)](#) summarized the common mean diameters and their range of applications (see Table 5.2). For the characterization of the two-phase flow investigated in the wind tunnel, the arithmetic ( $d_{10}$ ) and volume mean ( $d_{30}$ ) diameters were relevant. Therefore, these values are considered in the following. Note that in the meteorology the mean masses are commonly calculated (which can be then converted to diameters), using the moments of the mass distribution function  $q$ . E.g., a number weighted mean mass  $x_{10}$  can be calculated by the ratio of the first (LWC) and zeroth (total number of droplets) moment of the mass distribution function:

$$x_{10} = \frac{\int_x q(x) dx}{\int_x x q(x) dx} = \frac{\text{LWC}}{N}. \quad (5.5)$$

**Table 5.2:** Mean diameters and their applications, following Lefebvre (1989). The order can be determined by summing the numbers in the index of  $d$ . E.g., for Sauter mean diameter, the order is  $3 + 2 = 5$ .

Symbol	Name	Application
$d_{10}$	<b>Arithmetic mean</b>	<b>Comparison</b>
$d_{20}$	Surface mean	Surface area controlling
$d_{30}$	<b>Volume mean</b>	<b>Volume controlling</b>
$d_{21}$	Length mean (surface area)	Absorption
$d_{31}$	Length mean (volume)	Evaporation, molecular diffusion
$d_{32}$	Sauter mean	Mass transfer, reaction
$d_{43}$	Herdan mean/de Brouckere	Combustion equilibrium

### 5.3.1 Velocity and diameter measurements

Velocities measured by PDA are based on the same principles as LDV. However, using PDA, the simultaneous measurement of diameter and velocity values is possible. This allowed the investigation of the velocity–diameter correlation (Fig. 5.9). The projection of the scatter plot onto the  $y$ -axis shows the Gaussian distribution of the droplet velocities, while the projection onto the  $x$ -axis represents the log–normal DSD.

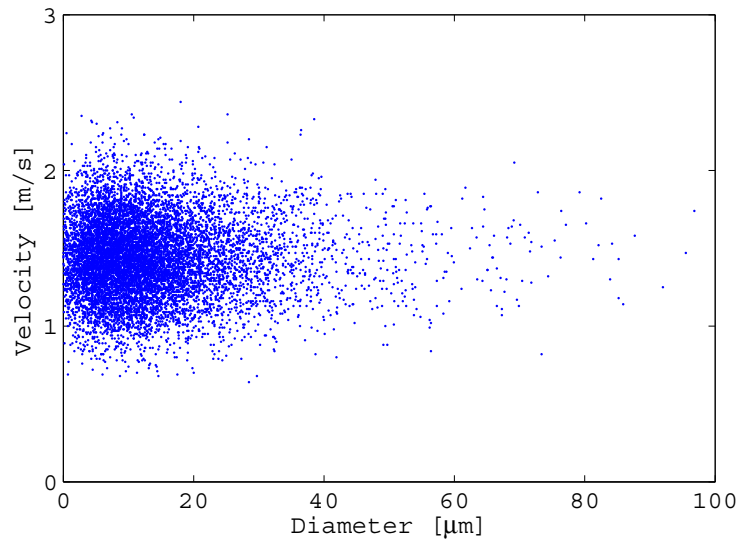


**Figure 5.9:** Velocity-diameter correlation of the water droplets for the configuration M1 at the  $x = 0$ ,  $y = 5$ ,  $z = 0$  mm position.

The response of the droplets to the flow can also be noticed in this scatter plot. Smaller droplets have a higher velocity fluctuation, while the larger ones converge toward the mean velocity value.

Having the measurement results of both phases, the relative velocity of the droplets could be calculated, which was found to be 0.3 m/s in average for the configuration **M1** at  $x = 0$ . This value reduced to 0.15 m/s as the droplets reached the  $x = 400$  plane. It can be concluded that in this configuration, the droplets were still accelerating within the measurement section.

Selecting the first ( $x = 0$ ) measurement plane as a boundary condition for a numerical simulation, the suitability of the applied model and parameters can be validated with further measurement results, as shown in Section 5.6.1. As an example, the mean velocity results of the droplets, measured by means of PDA in the configuration **M1** for the planes  $x = 0$ ,  $x = 200$  and  $x = 400$  mm are presented in Fig. 5.10.

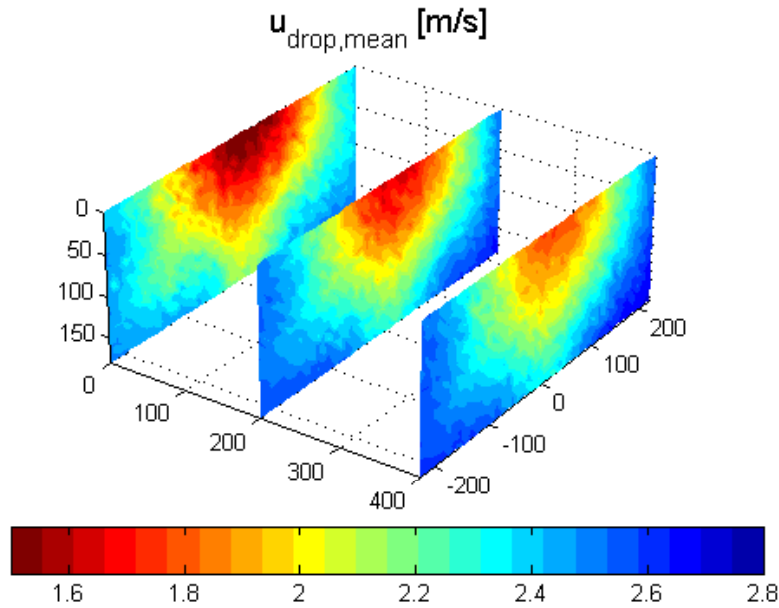


**Figure 5.10:** Mean droplet velocity distribution in the planes  $x = 0$ ,  $x = 200$  and  $x = 400$  of the configuration **M1**, measured by means of PDA.

### 5.3.2 Derived values

Further properties could be deduced by post-processing the measurement data, such as the number of droplets per unit volume, the number of droplets

of certain radii per unit volume, or the collision rate per unit volume, as explained in Chapter 4.

### Droplet number density

Measurements of droplet concentration have already been discussed by other groups (Roisman and Tropea, 2000, 2001; Sommerfeld and Qiu, 1995; Tropea et al., 1996). In the present work and based on PDA measurements, the droplet number density calculations by Roisman and Tropea (2001) were applied in a slightly modified manner, as described in Chapter 4, allowing the calculation of the standard deviation and of the probability density function. This PDF was the main interface between the experiments and the simulations (boundary conditions) as discussed later in Section 5.6.

The average mean droplet number density per unit volume was found to be  $2000 \text{ 1/cm}^3$  for the configuration **M1** at  $x = 0$ . The associated spatial distribution is presented in Fig. 5.11. Theoretically, calculating with a droplet injection rate of  $0.1 \text{ 1/min}$  and a mean droplet diameter of  $12.5 \text{ }\mu\text{m}$ , the corresponding droplet number density per unit volume should indeed approximately be  $2000 \text{ 1/cm}^3$ , confirming experimental measurements. This value corresponds to the typical values in cumulus clouds (Kampe, 1950), as listed in Table 5.5.

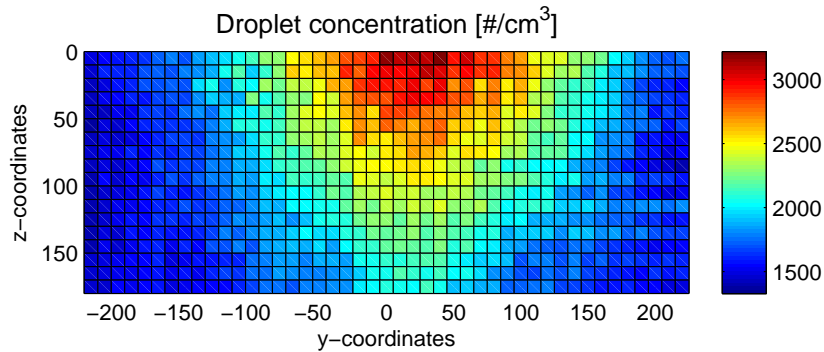


**Figure 5.11:** Droplet number density per unit volume in  $\text{1/cm}^3$  at  $x = 0$  calculated from the PDA results as described by Roisman and Tropea (2001) and discussed in Chapter 4.

### Droplet collision rate

The employed evaluation algorithm, as described previously in Chapter 4, was based on droplet shape recognition and discriminates collision events from

aerodynamic droplet deformation, which is an essential issue when considering large droplet diameters, where the  $We$ -number is larger than 1. Different theoretical predictions of collision probability can be found in the literature for corresponding conditions, as discussed in Chapter 1 and summarized in Table 1.2 on page 18. The calculation of theoretical collision rates was done in this chapter according to the equation from Williams and Crane (1983):

$$N = n^2 d_{1,2}^2 (8\pi \overline{u'^2})^{1/2} . \quad (5.6)$$

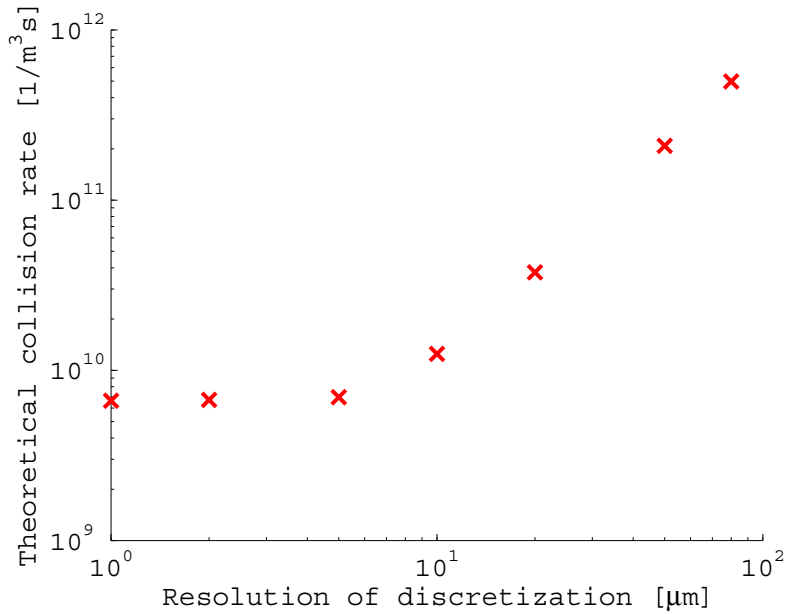


**Figure 5.12:** Influence of the discretization resolution on the calculated theoretical collision rate.

Nevertheless, it should be kept in mind that this equation is originally valid for single droplet sizes and not for a droplet size distribution. Therefore, the theoretical collision rate was calculated by the above equation for each size class pair obtained by discretizing the distribution with a resolution of  $2 \mu\text{m}$  (a finer resolution does not change the obtained results, see Fig. 5.12):

$$N = \sum_{i,j} N_{i,j} = \sum_{i,j} n_i n_j d_i d_j (8\pi (u_{i,p,rel}^2 + u_{j,p,rel}^2))^{1/2} . \quad (5.7)$$

The resulting matrix is graphically presented in Fig. 5.13. Due to symmetry ( $N_{i,j} = N_{j,i}$ ), only half of the matrix has to be considered. Finally, the elements of one triangular part of the resulting matrix were then summed up,

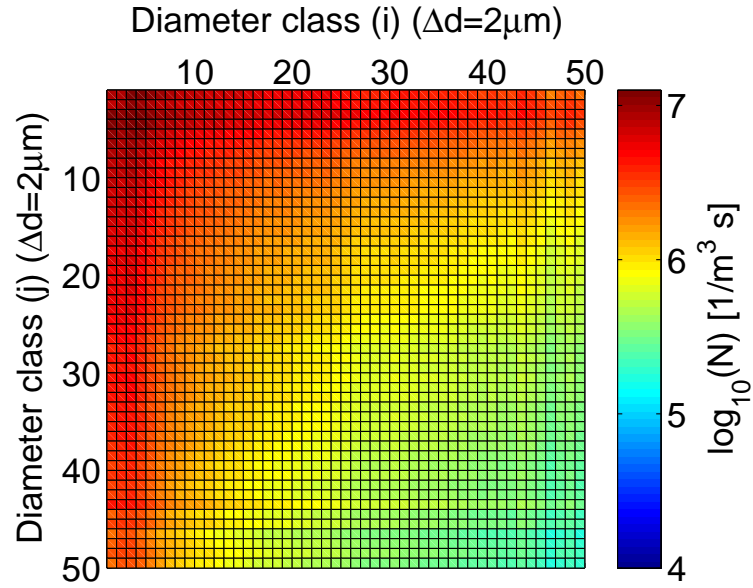


**Figure 5.13:** Collision rate matrix of the discretized droplet size distribution.

to consider each collision event exactly once (including the matrix principal diagonal) (Bordás et al., 2011).

**Table 5.3:** Properties required for the calculation of theoretical collision rates at the discussed measurement points, as measured by PDA.

	$d_{10}$ [ $\mu\text{m}$ ]	$n$ [ $1/\text{m}^3$ ]	$u'_{p,rel}{}^2$ [ $\text{m/s}$ ]
Configuration <b>M3</b> , $x = 0$ mm, $y = 0$ mm			
$z = 0$	14.50	$5.74 \cdot 10^9$	0.31
$z = 40$	14.20	$5.50 \cdot 10^9$	0.36
$z = 90$	13.70	$6.83 \cdot 10^9$	0.43
$z = 140$	14.00	$4.74 \cdot 10^9$	0.33
Configuration <b>M4</b> , $x = 0$ mm, $y = 150$ mm			
$z = 0$	9.70	$2.57 \cdot 10^9$	0.22
$z = 20$	10.10	$2.31 \cdot 10^9$	0.23
$z = 40$	9.70	$2.59 \cdot 10^9$	0.25
$z = 60$	9.60	$2.31 \cdot 10^9$	0.40
$z = 90$	8.05	$3.21 \cdot 10^9$	0.67
$z = 120$	7.50	$2.40 \cdot 10^9$	0.61
$z = 140$	7.75	$1.92 \cdot 10^9$	0.40



The theoretical droplet collision rates  $N_{th}$  calculated in this manner are presented in Table 5.4. For comparison with them, collision rates  $N_D$  and  $N_n$  estimated experimentally by Shadowgraphy following the procedure described in Chapter 4 (see also Bordás et al. (2010)) are also listed.

Different profiles were selected for the Shadowgraphy measurements in the Configurations **M3** and **M4**, each in the  $x = 0$  plane at  $y = 0$  and  $y = 150$  mm, respectively. The  $z$ -coordinates were in the range of  $z = 0$  down to 140 mm.

The experimental collision rate has been determined in two different manners. Either using the data rate, subscript  $D$  or the concentration, subscript  $n$  respectively, both obtained from PDA measurements. The two results are nearly identical, confirming the robustness of the procedure. Furthermore the standard deviation of the collision rates is given here as  $\sigma$ , using again the same indices for concentration or data rate based values. After post-processing the experimental results of Shadowgraphy, a local collision probability  $p_{coll}$  was measured as described in Chapter 4. This should be converted to collision rate, with the usual units of  $1/\text{m}^3\text{s}$ . This could be realized by either using the data rate  $D$  or the droplet number density  $n$ . In Table 5.4, the experimental collision rate has been calculated using both the data rate  $D$  and the concentration  $n$ , obtained from previous PDA measurements. The results are also presented in Fig. 5.14. The theoretical collision probability, calculated by Eq. (5.7) is plotted as well in Fig. 5.14 for the considered positions.

**Table 5.4:** Experimentally determined collision rates together with their standard deviation  $\sigma$  and comparison with theoretical predictions.

$z$ [mm]	$N_{th}$	$N_D$	$\sigma_{N,D}$ [ $1/\text{m}^3\text{s}$ ]	$N_n$	$\sigma_{N,n}$	$\frac{N_D}{N_{th}}$	$\frac{N_n}{N_{th}}$ [-]
Configuration <b>M3</b> , $x = 0$ mm, $y = 0$ mm							
0	$9.66 \cdot 10^9$	$4.33 \cdot 10^{10}$	$3.84 \cdot 10^9$	$4.47 \cdot 10^{10}$	$7.05 \cdot 10^9$	4.49	4.63
40	$6.77 \cdot 10^9$	$4.44 \cdot 10^{10}$	$3.81 \cdot 10^9$	$4.52 \cdot 10^{10}$	$6.89 \cdot 10^9$	6.59	6.71
90	$1.26 \cdot 10^{10}$	$6.07 \cdot 10^{10}$	$4.10 \cdot 10^9$	$7.56 \cdot 10^{10}$	$9.10 \cdot 10^9$	4.83	6.02
140	$5.22 \cdot 10^9$	$3.20 \cdot 10^{10}$	$3.85 \cdot 10^9$	$2.96 \cdot 10^{10}$	$6.34 \cdot 10^9$	6.14	5.68
Configuration <b>M4</b> , $x = 0$ mm, $y = 150$ mm							
0	$1.85 \cdot 10^9$	$5.58 \cdot 10^9$	$6.32 \cdot 10^8$	$4.96 \cdot 10^9$	$5.56 \cdot 10^8$	3.02	2.68
20	$1.66 \cdot 10^9$	$5.48 \cdot 10^9$	$7.02 \cdot 10^8$	$5.05 \cdot 10^9$	$6.40 \cdot 10^8$	3.30	3.05
40	$1.72 \cdot 10^9$	$4.97 \cdot 10^9$	$6.40 \cdot 10^8$	$5.02 \cdot 10^9$	$6.40 \cdot 10^8$	2.89	2.92
60	$2.68 \cdot 10^9$	$5.37 \cdot 10^9$	$8.64 \cdot 10^8$	$6.08 \cdot 10^9$	$9.67 \cdot 10^8$	2.01	2.27
90	$6.62 \cdot 10^9$	$1.11 \cdot 10^{10}$	$1.98 \cdot 10^9$	$1.70 \cdot 10^{10}$	$2.99 \cdot 10^9$	1.67	2.57
120	$4.28 \cdot 10^9$	$7.75 \cdot 10^9$	$1.21 \cdot 10^9$	$9.70 \cdot 10^9$	$1.49 \cdot 10^9$	1.81	2.27
140	$1.37 \cdot 10^9$	$4.12 \cdot 10^9$	$6.53 \cdot 10^8$	$4.11 \cdot 10^9$	$6.40 \cdot 10^8$	3.02	3.01

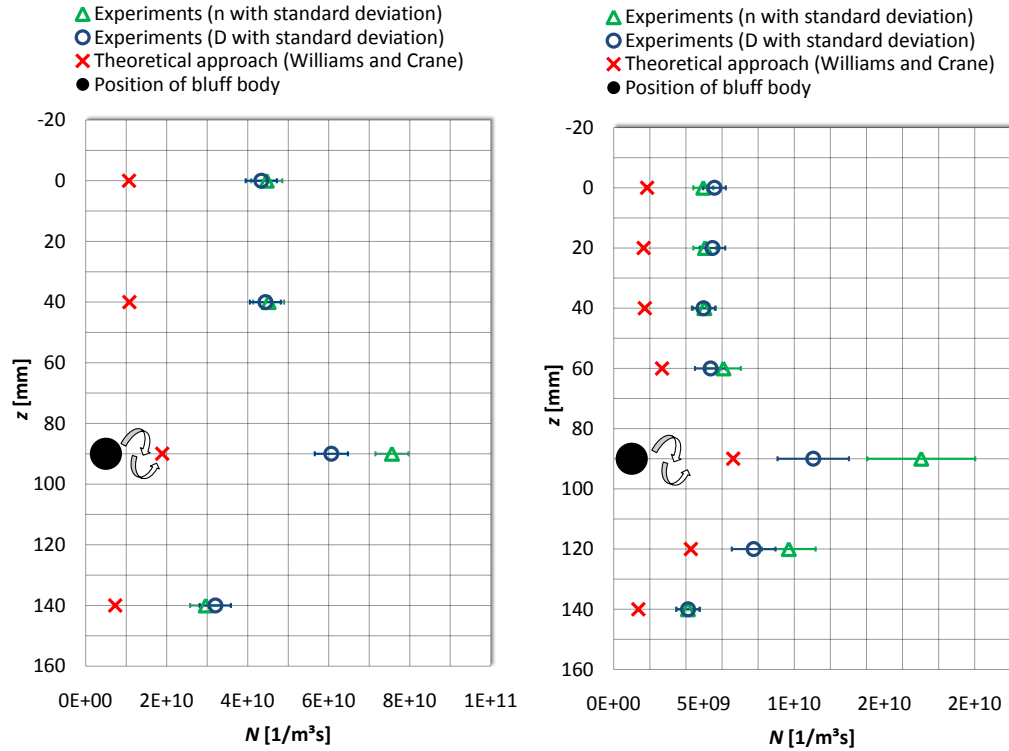


**Figure 5.14:** Comparison of the measured (blue, green) and theoretical (red) collision rates per unit volume for the configuration **M3** (left) and **M4** (right) at different  $z$ -heights.

Finally, the comparison between theoretical predictions and measured results shows qualitatively a good agreement for the present case (Fig. 5.14). The influence of the bluff body is remarkable: PDA measurements showed that for this position (Table 5.3,  $z = 90$ ) the droplet number density was increased, which can be explained by the preferential concentration of the droplets (Shaw et al., 1998). The experimental droplet collision rate shows also an increase in the wake of the cylinder in agreement with the theoretical prediction (Table 5.4 and Fig. 5.14).

However, quantitatively the experimental findings lead again systematically to an increased collision rate, typically by a factor of 2 to 6, compared to theory. The noticeably increased collision rate measured in all configurations would support the findings of other groups, for instance the observations discussed by Xue et al. (2008), showing that the theory underestimates the collision rate in turbulent flows. It should be noted that the conversion by means of the droplet number density  $n$ , showed a larger deviation for this measurement configuration. Since the determination of  $n$  is rather complicated, as shown

before, the reliability of the values based on  $D$  is higher. These values ( $N_D$ ) are therefore preferred in the following.

The collision rates measured by Shadowgraphy for the configuration **M3** also showed a good agreement with PDA measurements of droplet growth, as exemplified in Fig. 5.15. PDA shows an increase in diameter by 18%, corresponding to a volume growth of 63% during travel time within the measurement section. The collision rates measured by Shadowgraphy would lead to a typical volume increase of about 60%, assuming that each collision event successfully leads to coalescence. This agreement demonstrates that

- growth by collisions was the dominating process for the present measurements, in which condensation and evaporation play a negligible role.
- the experimentally measured collision rates are validated indirectly by an independent measurement technique, PDA.

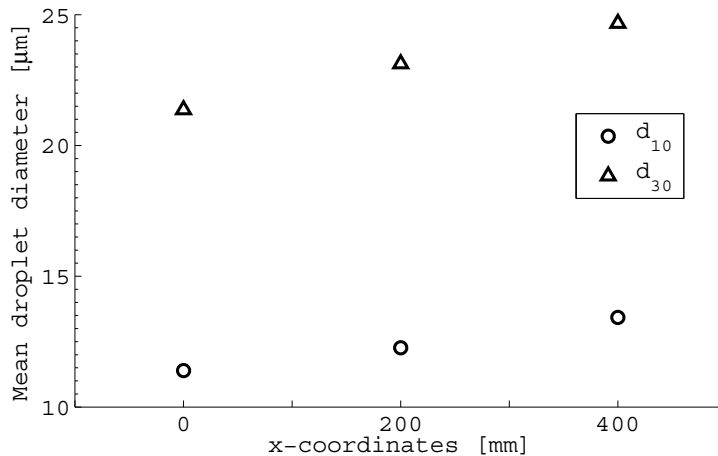


**Figure 5.15:** Mean and volume mean diameter development along the  $x$ -axis for the configuration **M3**, measured by means of PDA. The increase in mean droplet sizes can be recognized.

## 5.4 Consequences for rain formation in clouds

In this section the influence of the different turbulent conditions on rain formation (Bordás et al., 2011a) is discussed.

### 5.4.1 Reproducing cloud turbulence at small scales

In configuration **M1** the turbulent kinetic energy generation occurred without any artificial influence of the turbulence properties, as mentioned before. However, the injection in counter-flow direction already caused relatively high turbulence intensities. In this way the objective (generate more energetic turbulence structures) was already fulfilled. For the project the variation of different turbulence and spray properties was furthermore required, which was assured by the configurations **M2**, **M3** and **M4**.

The velocity distribution was remarkably influenced by the geometrical conditions in the different configurations. A comparison of the inlet velocities is presented in Fig. 5.16, where the inlet plane for each of four configurations is shown. The difference to the configuration **M1**, without any artificial turbulence except for the injection in counter-flow direction, can be easily recognized. In case of the configuration **M2**, the velocity distribution was smoother, i.e., the velocity distribution narrower, due to the grid. The results of the configuration **M3** showed the influence of the bluff body, fixed horizontally in the middle of the measurement section at  $z = 90$  mm. In case of the configuration **M4**, both phenomena could be noticed and additionally the influence of the double injection-head could be observed, though this was noticeably suppressed by the passive grid.

The characteristic values describing turbulence in cumulus clouds can be found in the literature (Pruppacher and Klett, 1997; Shaw, 2003). Most significant values, which determine the turbulent scales, are the turbulent kinetic energy (TKE)  $k$  and its dissipation rate  $\varepsilon$ . TKE is a measure of the velocity fluctuations, which is typically moderate in cumulus clouds. Thus, the TKE value should be in the order of magnitude of  $0.8 \text{ m}^2/\text{s}^2$  (see Table 5.1 on page 100). This means velocity fluctuations of approx.  $1 \text{ m/s}$ . During our measurements, velocity fluctuations of up to approx.  $0.35 \text{ m/s}$  were measured. This means a TKE of around  $k = 3/2\overline{u'^2} = 0.22 \text{ m}^2/\text{s}^2$ , which is already in the right order of magnitude. The energy dissipation rate,  $\varepsilon$  can vary over several orders of magnitude in turbulent clouds, but is relatively low compared to lots of other engineering flows ( $\varepsilon = 0.01 \dots 0.1 \text{ m}^2/\text{s}^3$  (Rogers and Yau, 1996)).

The typical values found in clouds and those of the flow in our wind tunnel are summarized in Tables 5.1 and 5.5. It can be seen that all properties relevant for rain initiation are in the right order of magnitude. As a consequence, all findings of this study should be applicable as well to rain formation in cumulus clouds.

**Table 5.5:** Typical values in cumulus clouds and the corresponding ones in the wind tunnel.

Denomination	Cumulus clouds	Wind tunnel
Relative humidity	saturated air	saturated air
LWC	0.1 . . . 7 g/m <sup>3</sup>	2 g/m <sup>3</sup>
Number density	1 . . . 7 000 1/cm <sup>3</sup>	2 000 1/cm <sup>3</sup>

### 5.4.2 Passive grid

The passive grid had a homogenizing effect in this case (see the velocity distribution in Fig. 5.16 for the configuration **M2**), thus causing a narrower velocity distribution and lower velocity fluctuations, remarkably suppressing the influence of the injection system. Therefore, the standard deviation of velocity was also moderate. The passive grid globally decreased the turbulent kinetic energy and its dissipation rate. However, comparing theoretical predictions in Table 3.6 on page 62 (Chapter 3) with the measured values (Table 5.1 on page 100), it is clear that the theory strongly underpredicts turbulence level, probably due to the inhomogeneous flow upstream of the grid.

### 5.4.3 Bluff body

The bluff body increased the velocity fluctuations behind the cylinder due to shedding vortices, as expected (see the velocity distribution in Figs. 5.16 and 5.5 for the configuration **M3**). As it can be seen in Fig. 5.16, the droplet velocities were also noticeably influenced, since they could partly follow the changes in the continuous flow. Therefore, the droplet concentration also increased in the cylinder wake, due to preferential concentration, leading to an increased collision rate. The expected mean distance between two subsequent vertices (about 10 cm) was also observed, as it can be noticed in Fig. 5.5. However, the vortex street was relatively irregular, probably due to the high Reynolds number and the non-uniform inlet flow, as already discussed in Chapter 3.

### 5.4.4 Conclusions

As consequences for rain formation it is shown that the aim of this work was achieved, through carrying out experimental measurement in a two-phase wind tunnel applying different flow configurations, of which properties were

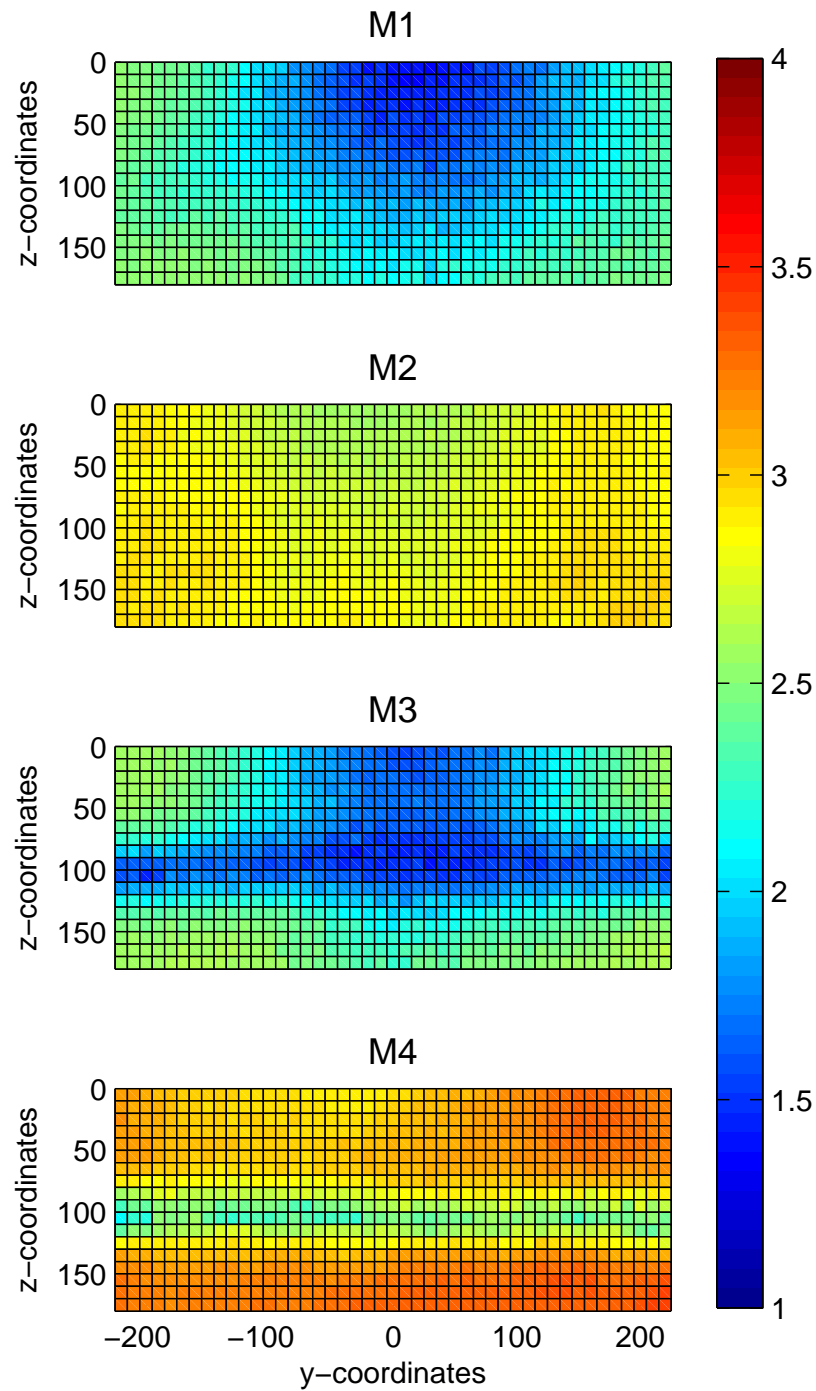


**Figure 5.16:** Mean longitudinal velocity distribution of the droplets at  $x = 0$ , measured by means of PDA, for the configurations **M1**, **M2**, **M3** and **M4**, respectively.

adapted to that of cumulus clouds. Flow properties were systematically varied and their influence was examined, including particle concentration, which was also compared with theoretical predictions. The experimental data were collected systematically in a database, which serves mainly the aim of validation of companion numerical simulations.

It is also confirmed here apparently by the first systematical experimental investigation of collision events in the world that measured collision rates are underestimated by theory in certain circumstances, in agreement with theoretical and numerical findings of other groups. This means that model improvements are necessary for the prediction of collision rates in turbulent flows in the size regime associated to the growth gap. The significant role of turbulence on preferential concentration and on collision rates is also supported by the measurements in the wake of the cylinder.

## 5.5 Online experimental database

Results of all the measured configurations are freely available in a structured online database at the address <http://www.ovgu.de/iust/lss/metstroem>. The database was prepared in an Open Source Content Management System, Plone<sup>®</sup> CMS and its contents are continuously updated. The starting page of the database contains a login system, which does not limit the access, but creates an obstacle for unauthorized use of the database. The registration can be done by sending a request e-mail to the webmaster, who manually registers the new user, generating automatically an account with a login and a password. After logging in, the database user gets to the starting page. This page contains general information about the wind tunnel, measurement planes and spray injection.

The structure of the database is based on the experimental configurations:

- **M1** - without any artificial turbulence modification,
- **M2** - with a passive grid,
- **M3** - with a bluff body and
- **M4** - with both grid and bluff body and a double spray configuration.

Schematics of the different configurations simplify the understanding of the measurement setup. By clicking on a certain configuration (see Fig. 5.17),

the associated web page can be reached. Each page of a certain configuration contains the full measurement data in ASCII format, ready for download.

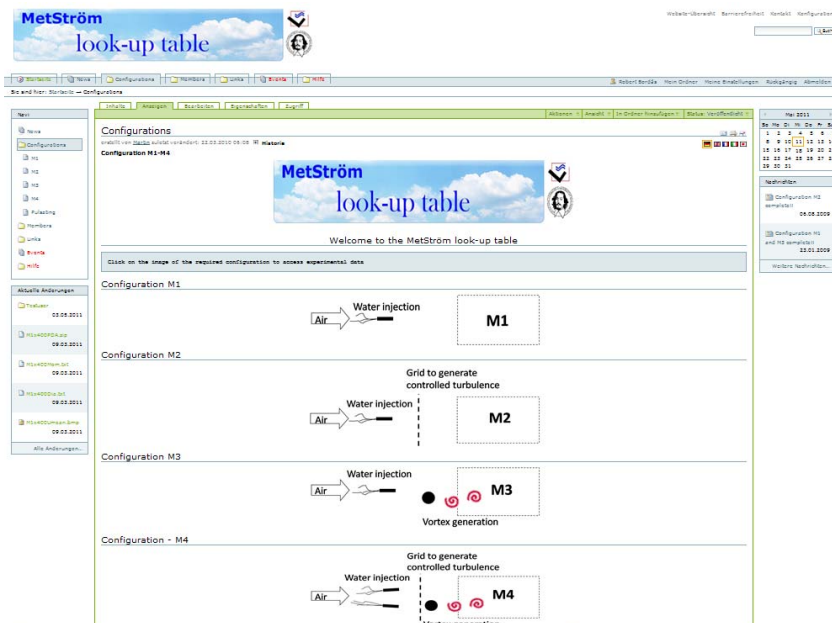


**Figure 5.17:** Screenshot of the database: navigation page containing the different experimental configurations.

Every experimental subfolder includes:

- the time-averaged measurement data,
- the instantaneous values compressed in a zip-file,
- and a contour or vector plot to simplify data presentation, mainly for the validation of companion numerical simulations.

The experimental data are structured according to three different properties that can be combined in a search:

- the different measurement configurations,
- the measurement planes,
- and the measurement methods.

The measurement configurations are characterized by their flow properties, collected in a table. The measurement methods are also briefly described. For a better overview, contour plots of the measured quantities and tabular



values are included as well. The database has also got a search function to ease data access in the database (e.g., “look for measurement data at the plane  $x = 0$  of every configuration”).

An automatic report is generated as well about the actual updates and a mailing list is available to inform database users. In order to exemplify the content of this database, Appendix B to E contain selected examples of the results.

## 5.6 Companion numerical simulations

As part of a collaboration with the Free University of Berlin, configuration **M1** has been simulated based on a population balance approach to describe the droplet population. A detailed description can be found in [Bordás et al. \(2011b\)](#).

The inlet boundary condition of the air flow is directly based on LDV-measurements of the continuous phase, while the initial droplet properties are determined from PDA experiments, as presented previously in Chapter 4 (Fig. 4.5 on page 82).

The behavior of the droplet population is modeled by means of a population balance system, consisting of the Navier–Stokes equations describing the air flow together with an additional equation for the DSD. This equation takes into account the transport, the growth, and the aggregation of droplets. The DSD describes the spatial evolution of the droplet diameters (so-called internal coordinate) such that the equation for the DSD is finally defined in a 4D domain.

In the applied method, the turbulent flow field is simulated fully implicitly. A variational multiscale (VMS) method is applied for turbulence modeling. The backward and forward Euler schemes are used as temporal discretization for the population balance equation. A preprocessing approach was applied to compute the aggregation integrals. The robustness of the prediction with respect to varying numerical methods has been furthermore demonstrated.

### 5.6.1 Numerical models

Only the lower half of the test section is simulated, in agreement with the experiments described previously in Chapter 3.

Boundary conditions for the flow field have to be prescribed at the whole boundary of the domain used in the simulations. It is not clear if the used outflow boundary condition, associated with zero normal stresses, could introduce a noticeable modeling error. For this reason, the domain for the simulations was chosen to be somewhat longer than the real measurement domain, so that the outflow boundary condition did not influence the computational results at the locations where comparisons are possible. Thus, the final computational domain in  $x$ -direction was set from 0...500 mm, while the rest was identical with the experiments.

The inlet condition at the  $x = 0$  mm plane was directly prescribed using the time-averaged experimental velocity and its standard deviation. The second and third components of the inlet velocity are set to be zero.

On all other boundaries, free slip with penetration conditions were used. This kind of boundary condition models fluctuations on the boundaries, which are directed inside and outside the domain. This corresponds to the experimental setup, since the boundaries of the measured volume are slightly away from the walls of the wind tunnel.

The complete domain was triangulated with a  $50 \times 45 \times 18$  hexahedral grid, equidistant in each direction. With this grid, the positions of the measurement points were located at computational nodes, allowing a direct comparison. In addition, the mesh for the internal coordinate was chosen in such a way that a direct fitting of the experimental data was possible. Since the data were given for equidistributed diameters, the grid for the internal coordinate was defined in the same way. To obtain an initial condition, the flow was simulated until it was fully developed (Fig. 5.18). An instantaneous flow field was then saved and used as initial flow field in all simulations. The DSD was modeled by a population balance equation, including transport, growth, and agglomeration of droplets.

As previously discussed, experimental data are available for the time-averaged first component of the droplet velocity at the planes  $x = 0$  mm,  $x = 200$  mm and  $x = 400$  mm (see Fig. 5.10). These values are subtracted from the experimental data of the time-averaged velocity of air, giving a time-averaged velocity difference between the dilute (water droplets) and continuous (air) phases. This difference was interpolated in  $x = 0 \dots 400$  mm and the values at the plane  $x = 400$  mm were used for the extrapolation in the domain  $x = 400 \dots 500$  mm, extending beyond the measured region. Then, this difference was subtracted from the first component of the velocity computed by the Navier–Stokes equations to define the first (longitudinal) component of the droplet velocity  $u_d$ . The other components of the droplet velocity were

just prescribed as the velocity components acquired from the solution of the Navier–Stokes equations.

A model for the growth rate due to condensation was derived in [Rogers and Yau \(1996\)](#), similar to that of Eq. (1.9). In all present simulations, a constant supersaturation of 1% ( $S = 1.01$ ) was assumed, which is a typical value for clouds and corresponds to an estimation of the maximum value found in the wind tunnel experiments (see Chapter 2). The model employed for the aggregation follows [Hulburt and Katz \(1964\)](#) and [Mersmann \(2001\)](#), consisting of two terms:

- the first one models the production of droplets of diameter  $d$  due to the agglomeration of smaller droplets, while
- the second term in the model accounts for the disappearance of droplets of diameter  $d$  because of their agglomeration with other droplets.

For the aggregation kernel two physical processes (Brownian motion and shear) are combined:

$$\kappa_{agg}(d, d') = C_{brown} \frac{2k_B T}{3\mu} (d + d') \left( \frac{1}{d} + \frac{1}{d'} \right) + C_{shear} \sqrt{2\nabla u : \nabla u} (d + d')^3, \quad (5.8)$$

where  $k_B = 1.38065 \cdot 10^{-23}$  J/K is the Boltzmann constant. The two dimensionless model parameters,  $C_{brown}$  and  $C_{shear}$ , are calibrated by fitting the numerical results to experimental data.

The experimental data obtained for the droplet number density  $n$  (in  $1/\text{cm}^3$ ), see Eq. (4.3), have to be converted first to a DSD  $q$  (in  $1/\text{m}^4$ ).

$$q_{in,exp}(x, d_{i+1/2}) = 10^{12} \frac{n_i}{d_{i+1} - d_i} \quad (5.9)$$

For the conversion of the experimental number density  $n_i$  to the DSD  $q$ , equality in Eq. (5.9) is assumed and the DSD is linearly interpolated. The standard deviation is scaled in the same way:

$$\sigma_{q,i}(x, d_{i+1/2}) = 10^{12} \frac{\sigma_{n,i}}{d_{i+1} - d_i}. \quad (5.10)$$

The corresponding numerical methods are described in detail in [Bordás et al. \(2011b\)](#).

### 5.6.2 Numerical results

All simulations were performed with the code MOONMD (John and Matthies, 2004). Figure 5.18 presents an example for an instantaneous view of the computed air velocity field. It can be clearly seen that the flow in the center of the channel is slower due to the nozzle mount placed upstream of the measurement section, similar to Fig. 2.9. The residence time of a droplet in the measurement section is typically below 0.2 s.

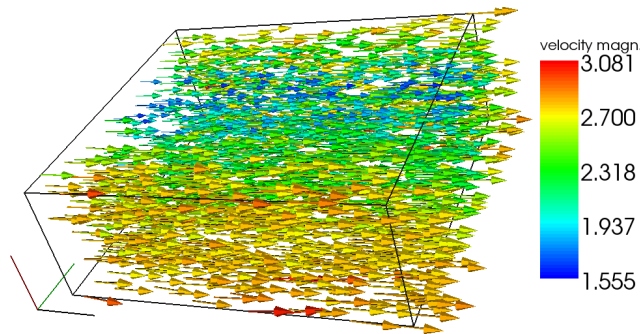


**Figure 5.18:** Instantaneous velocity field obtained from the simulation, with the outflow boundary of the measurement section ( $x = 400$  mm) on the right hand side.

The first purpose of these numerical studies was the calibration of the unknown Brownian and shear parameters in the aggregation kernel. The calibration was performed by fitting the computed DSD to the experimental data. The DSD was available from the experiments at each measurement point of the outlet plane ( $x = 400$  mm). Due to the turbulent character of the flow, the experimental data, which are already time-averaged, are rather different at different measurement points. For this reason, an averaging in space was applied to the data, leading to one space-time-averaged curve to compare with. The same space-time-averaging was applied for the computational results as well, where the time averaging was performed for an interval of 0.5 s.

Figure 5.19 presents results for the calibration of the required parameters. For small droplets, the aggregation associated to Brownian motion dominates, as expected from the physics. On the other hand, for larger droplets (typically for  $d \gtrsim 7$   $\mu\text{m}$ ), shear-induced aggregation and hence the shear parameter becomes essential to fit the experimental data correctly (Fig. 5.19). It should be noted that the used model for the DSD possesses only one direction, namely that larger droplets are created from smaller ones, by aggregation or by growth. Hence, a good prediction of the small droplets is a necessary basis for a good prediction of the large droplets. From the experimental setup it can

be expected that aggregation is the dominating mechanism. This dominance was numerically verified by comparing results without the growth term and with including this term using a realistic value for the supersaturation. As expected, the impact of the growth term on the simulated DSDs is negligible for the present conditions.

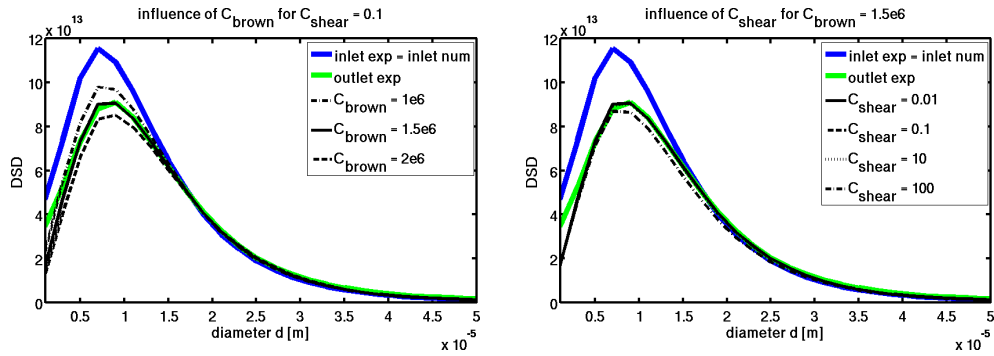


**Figure 5.19:** Calibration of the model parameters  $C_{\text{brown}}$  and  $C_{\text{shear}}$ . The green curves are the averaged experimental data at the outlet of the measurement volume, all other curves are simulation results.

Finally, it has been found that for appropriately chosen aggregation parameters, the change of the droplet size distribution observed in the experiments from the inlet to the outlet is very well reproduced by the numerical simulations.

## Conclusions

This chapter has presented the experimental results in the two-phase wind tunnel. All experimental data have been collected in a clearly structured database, accessible online. In order to get further information about the flow properties, post-processing of the measurement data is needed, which has also been discussed for both phases separately. Finally, companion numerical simulations have been briefly presented, showing a very promising agreement in first comparisons.

# Conclusions and outlook

---

## 6.1 Conclusions

The present work deals with optical measurements in disperse two-phase flows with a focus on meteorological problems. The main motivation is to create an experimental database, suitable for a quantitative validation of corresponding numerical simulations. Further on, the growth gap during warm rain initiation in cumulus clouds has been also considered, which process is not clearly understood yet. The experimental characterization of droplet collision rates in turbulent flows should help to improve existing theoretical and numerical models.

After a short introduction in rain formation and especially warm rain initiation, studies based on two-phase wind tunnels are reviewed. It is established that there is no single work dealing with systematic, non-intrusive investigation of cloud droplet interactions, where the results are collected in an online database with a free access. Then, an overview is presented about the theory of droplet collisions valid for cloud conditions. A suitable model is selected to calculate theoretical collision rates for later comparison.

Next, fundamentals of optical flow measurements are considered. Especially, different tracer particles for fluid measurements are investigated and compared with each other. Finally, a suitable seeding material (fog of polyethylene glycol (PEG)) has been selected for the measurement methods employed in this thesis.

For the experiments a two-phase wind tunnel has been specifically adapted to simulate all relevant conditions found in cumulus clouds. All important properties for the continuous phase (air mean velocity, velocity fluctuation, relevant turbulence parameters) as well as for the disperse phase (droplet size, droplet number density, liquid water content (LWC)) are finally very close to values typically found in cumulus clouds. Turbulent kinetic energy (TKE) and its dissipation rate are also adjusted to those typical for cumulus clouds.

Results obtained in a free flow, in a flow with turbulence modified by a passive grid, and in a flow perturbed by a cylindrical bluff-body inducing large-scale structures have been compared. A dual spray configuration has been considered as well, to enhance droplet collision probability and to broaden the involved droplet diameter spectrum. In this way a systematic variation of turbulence properties and of droplet diameter distributions have been realized.

For an accurate and quantitative investigation of the flow conditions associated with different configurations in the wind tunnel, a very careful adjustment of the applied optical measurement techniques is required. Therefore, the measurement techniques have been adapted to this difficult measurement environment. For this purpose the existing post-processing have been improved or even completely replaced by our newly developed post-processing tool.

Detailed measurements based on non-intrusive optical diagnostics have been used to characterize both the continuous and the disperse phase at different cross-sections. Velocity of both phases and diameter of the droplets have been measured as a function of time. Thus, some further flow properties could be deduced as well in order to characterize turbulence, such as turbulence intensity, TKE and its dissipation rate or the turbulence scales. Derived values of the disperse phase are important for the investigation of meteorological flows, such as droplet number density or collision rate per unit volume.

The calculation of droplet number density of defined droplet radii and its temporal fluctuation is especially an important issue, since it is the interface between experiments and numerical simulations as pointed out in this work. The boundary conditions are delivered in this manner, allowing a direct validation by comparisons.

The optimization of the Shadowgraphy technique for a quantitative investigation of droplet-droplet interactions is a major contribution of this work, since we appear to be the first group in the world able to characterize such collisions experimentally in a systematic, non-intrusive manner. Using the developed method the collision probability, i.e., the number of colliding droplets divided by the number of droplets in a unit volume can be determined experimentally. After measuring all parameters it becomes possible to calculate the collision rate from the measured collision probabilities combined with results from PDA and to compare with theoretical predictions.

Such a comparison with theoretical models shows a good agreement concerning the order of magnitude. Nevertheless, measured collision probabilities for the conditions used in the present work are systematically higher by a factor of 2

to 6 compared to theory, corroborating observations from other groups. For the present conditions, collisions dominate the droplet growth process rather than condensation.

All experimental results are summarized in a database, freely accessible through Internet, at the address <http://www.ovgu.de/isut/lss/metstroem>. The structure of the database is based on the different experimental configurations involving turbulence modification, as described in this work. With the help of the database, which is updated continuously, an exact investigation of droplet–droplet interaction is possible. The aim is to better understand meteorological flow processes, with emphasis on rain formation in cumulus clouds. Using this database it should become possible to validate in a quantitative manner simulation models and procedures needed to predict meteorological flows of interest.

The companion numerical simulations are also presented, using the experimental results of the measurements described in this work. First comparisons between experimental and numerical results showed a very promising agreement.

## 6.2 Outlook

At present, even more complex configurations are considered, in particular to check the possible influence of further parameters on droplet collision frequency. Time–dependent flows are used to investigate the impact of such gusts on the findings, which would increase the TKE of the flow. This can be achieved, either by varying the rotation speed of the fan in the wind tunnel as a function of time, or by deploying active or semi–active grids to generate even higher velocity fluctuations, leading ultimately to the desired TKE around  $1 \text{ m}^2/\text{s}^2$ .

Furthermore, further injection heads associated with different droplet sizes should be considered to enhance collision events within the test section while involving collision partners of different sizes, taking into consideration droplet size distributions and droplet number densities typical for cumulus clouds. In this manner, it should become ultimately possible to test theoretical predictions in a more systematic manner and to improve available models if needed.

Further on, solid particles should also be introduced into the flow, to check the effect on collision efficiency and droplet growth rate, as aerosols or ice particles do in cumulus clouds.



In future measurements the droplet temperature will be controlled, which is a cost-effective method to impose temperature differences between the continuous and the disperse phases. In this manner, the influence of evaporation/condensation will be also investigated and compared to numerical predictions.

APPENDIX A

# Wind tunnel specifications

---



<b>Test section: closed</b>			
<b>Windows</b>	Height [m]:	0.5	Width [m]: 1.5
	Height [m]:	0.4	Length [m]: 0.5
<b>Test table</b>	No. of windows [-]:	3	
			Width [m]: 0.45
	Outlet height [m]:	0.75	Outlet width [m]: 0.5
<b>Diffuser</b>	Inlet height [m]:	1.4	Inlet width [m]: 0.75
	Outlet height [m]:	0.5	Outlet width [m]: 1.4
<b>Confuser</b>			Length [m]: 1.9
			0.6
<b>Test section: open</b>			
<b>Test table</b>			Width [m]: 0.6
			Length [m]: 1.1
<b>Air inlet cone</b>	Outlet height [m]:	0.55	Outlet width [m]: 0.65
	Outlet height [m]:	0.75	Outlet width [m]: 0.75
<b>Diffuser</b>	Inlet height [m]:	1.4	Inlet width [m]: 1.4
	Outlet height [m]:	0.5	Outlet width [m]: 0.6
<b>Confuser</b>			Length [m]: 2.25
			Length [m]: 1.9
<b>Turning chamber – 1</b>			
<b>Guide vanes</b>	No. of vane blades [-]:	13	Vane chord length [m]: 0.25
	Inlet height [m]:	0.82	Inlet width [m]: 0.82
<b>Diffuser</b>	Outlet height [m]:	0.86	Outlet width [m]: 0.86
			Length [m]: 0.84
<b>Turning chamber – 2</b>			
<b>Guide vanes</b>	No. of vane blades [-]:	13	Vane chord length [m]: 0.25
	Inlet height [m]:	0.95	Inlet width [m]: 0.95
<b>Transition element</b>	Outlet diameter [m]:	1	Length [m]: 0.75

<b>Fan (50 Hz motor drive)</b>			
<b>Nose cone</b>	Rotor hub diameter [m]:	0.5	Length [m]: 0.15
<b>Rotor</b>	Rotor tip (duct) diameter [m]:	1	Nom. rotor RPM: 1475
	Nom. volume flow rate [m <sup>3</sup> /h]:	15	Nom. static pressure rise [Pa]: 800
<b>Electric motor</b>	Nom. RPM:	1475	Nom. shaft power [kW]: 18.5
	Minimum frequency [Hz]:	0	Maximum frequency [Hz]: 120
<b>Outlet guide vane</b>	No. of guide vane blades [-]:	5	Vane blade chord length [m]: 0.1
<b>Duct</b>	Diameter [m]:	1	Length [m]: 2
<b>Diffuser</b>	Inlet height [m]:	1	Inlet width [m]: 1
	Outlet height [m]:	1.15	Outlet width [m]: 1.15
<b>Turning chamber – 3</b>			
<b>Guide vanes</b>	No. of vane blades [-]:	13	Vane chord length [m]: 0.3
<b>Duct</b>	Height [m]:	1.15	Width [m]: 1.15
<b>Turning chamber – 4</b>			
<b>Guide vanes</b>	No. of vane blades [-]:	13	Vane chord length [m]: 0.3
<b>Straightener insert</b>	Inlet height [m]:	1.15	Inlet width [m]: 1.15
	Outlet height [m]:	1.4	Outlet width [m]: 1.4
<b>Duct</b>	Height [m]:	1.4	Width [m]: 1.4
<b>Inserts with mounts</b>			
<b>For grids</b>	Height [m]:	0.5	Width [m]: 0.6
<b>For sprays</b>	Diameter [m]:	0.10	No. of inserts: 6

Table A.1: Wind tunnel data sheet.

# Selected experimental results, Configuration M1

---

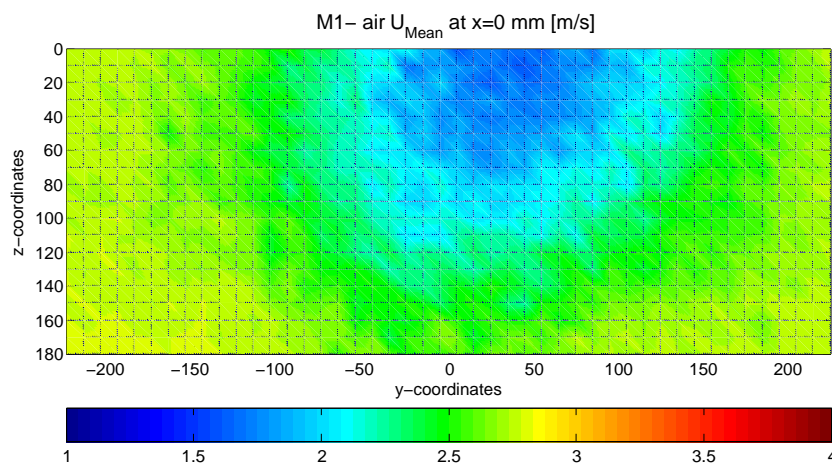


**Figure B.1:** Mean air velocity distribution of configuration M1 at  $x = 0$  mm, measured by LDV.

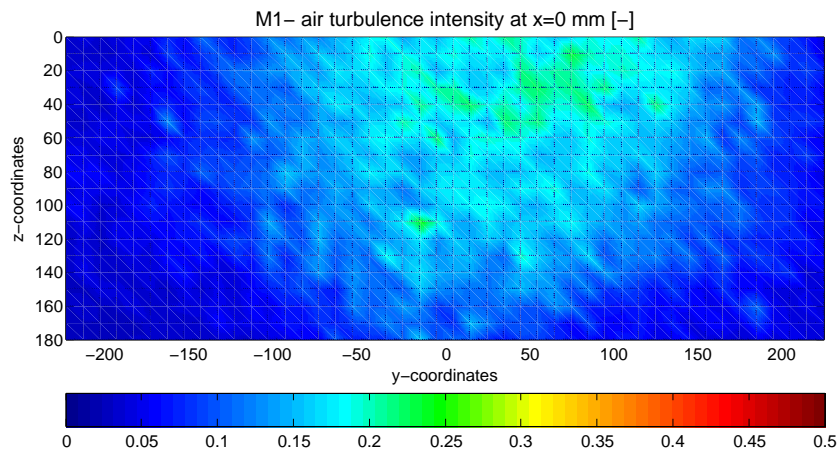


**Figure B.2:** Air turbulence intensity of configuration M1 at  $x = 0$  mm, measured by LDV.

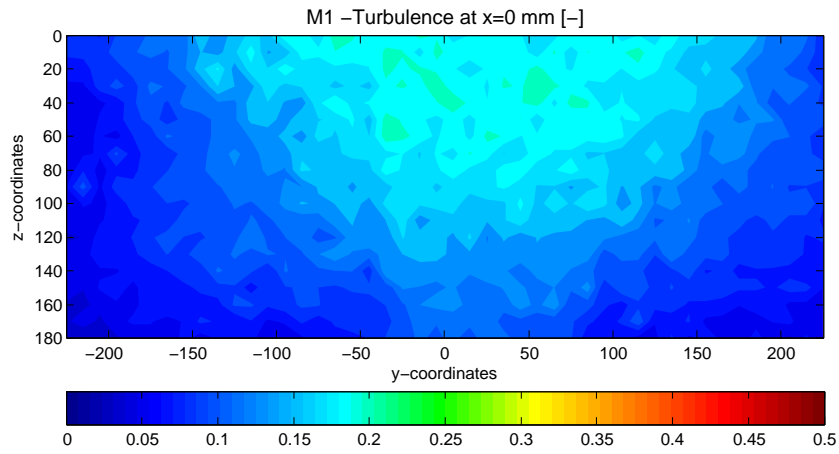


**Figure B.3:** Turbulence intensity distribution of the disperse phase of configuration M1 at  $x = 0$  mm, measured by PDA.

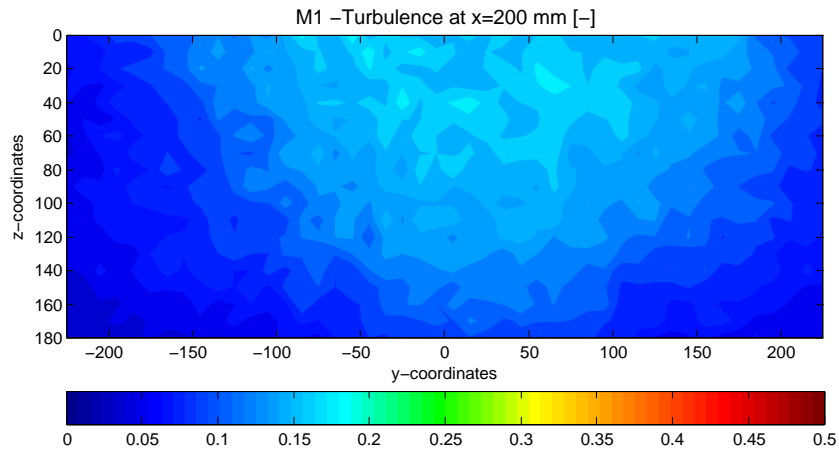


**Figure B.4:** Turbulence intensity distribution of the disperse phase of configuration M1 at  $x = 200$  mm, measured by PDA.

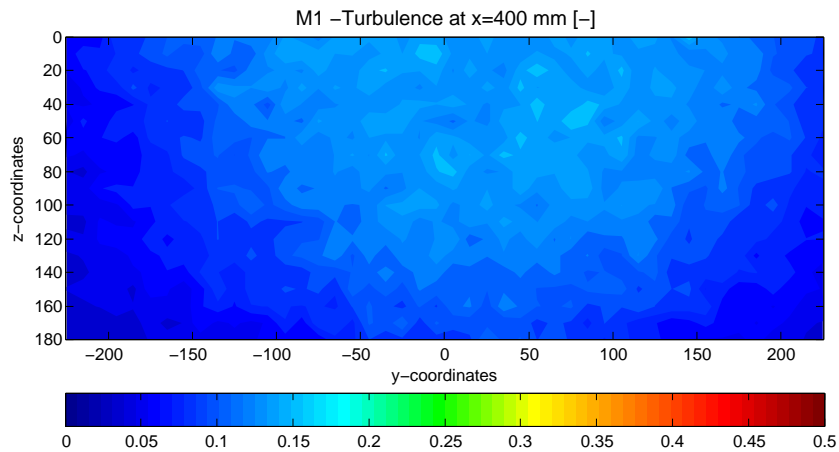


**Figure B.5:** Turbulence intensity distribution of the disperse phase of configuration M1 at  $x = 400$  mm, measured by PDA.

# Selected experimental results, Configuration M2

---

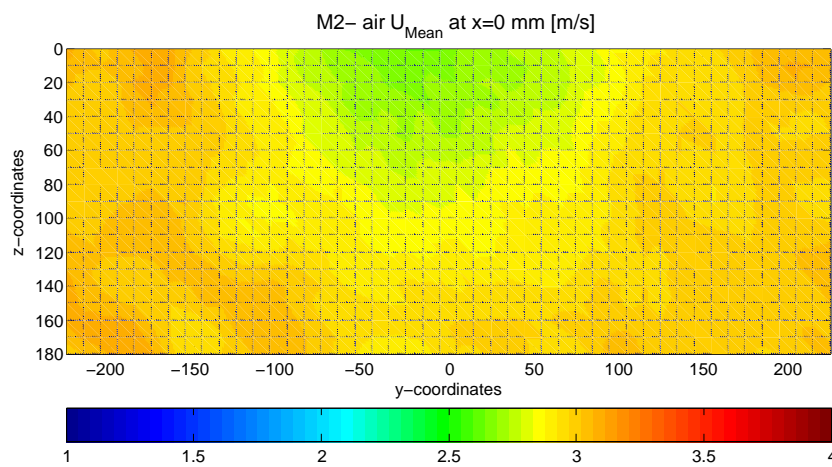


**Figure C.1:** Mean air velocity distribution of configuration **M2** at  $x = 0$  mm, measured by LDV.

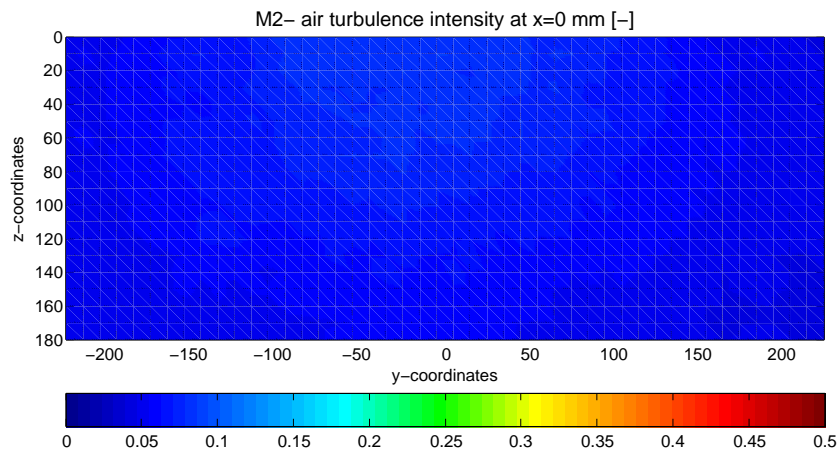


**Figure C.2:** Air turbulence intensity of configuration **M2** at  $x = 0$  mm, measured by LDV.



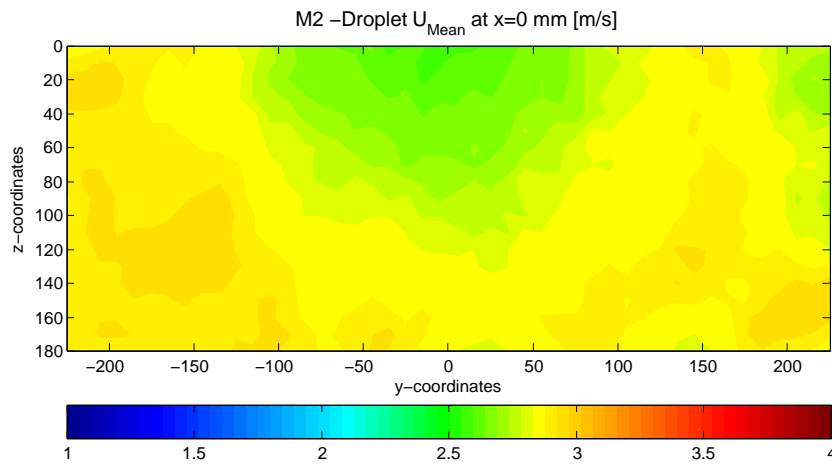


Figure C.3: Mean droplet velocity distribution of configuration M2 at  $x = 0$  mm, measured by PDA.

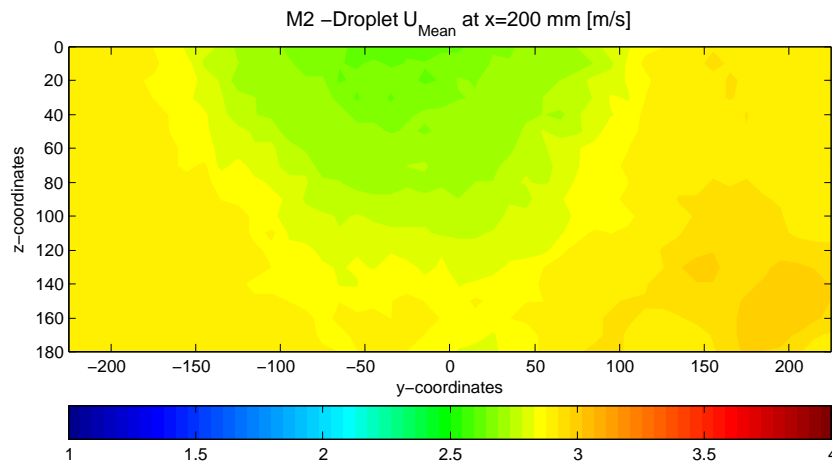


Figure C.4: Mean droplet velocity distribution of configuration M2 at  $x = 200$  mm, measured by PDA.

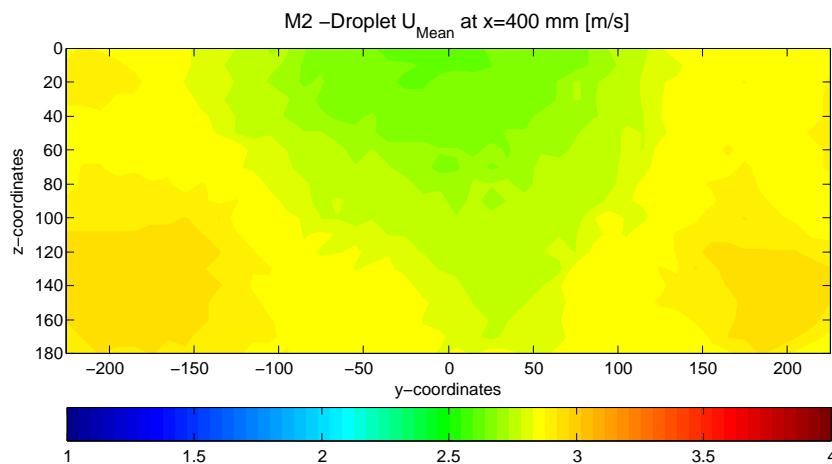
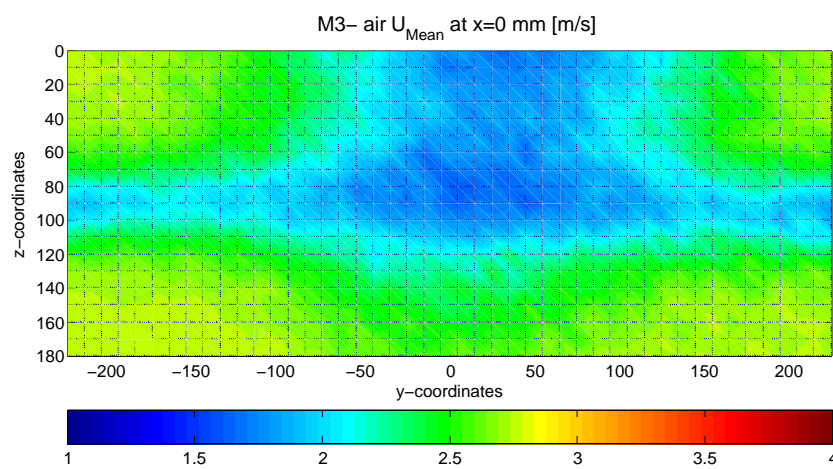


Figure C.5: Mean droplet velocity distribution of configuration M2 at  $x = 400$  mm, measured by PDA.

# Selected experimental results, Configuration M3

---



**Figure D.1:** Mean air velocity distribution of configuration **M3** at  $x = 0$  mm, measured by LDV.

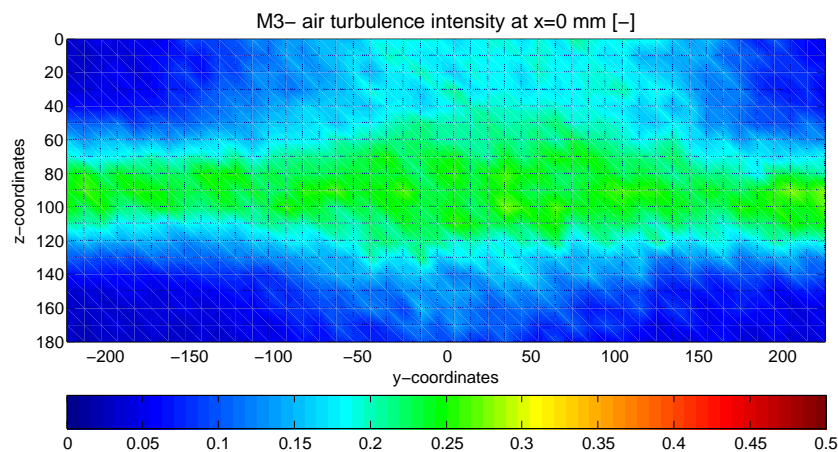


**Figure D.2:** Air turbulence intensity of configuration **M3** at  $x = 0$  mm, measured by LDV.

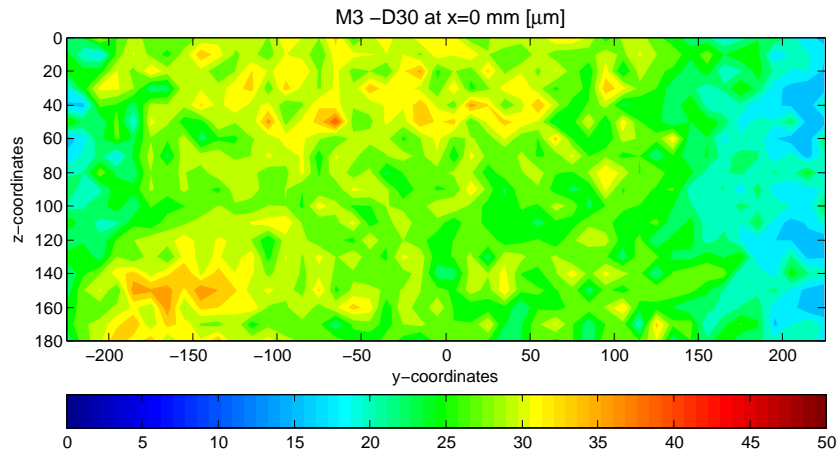


**Figure D.3:** Droplet volume mean diameter ( $D_{30}$ ) distribution of configuration M3 at  $x = 0$  mm, measured by PDA.

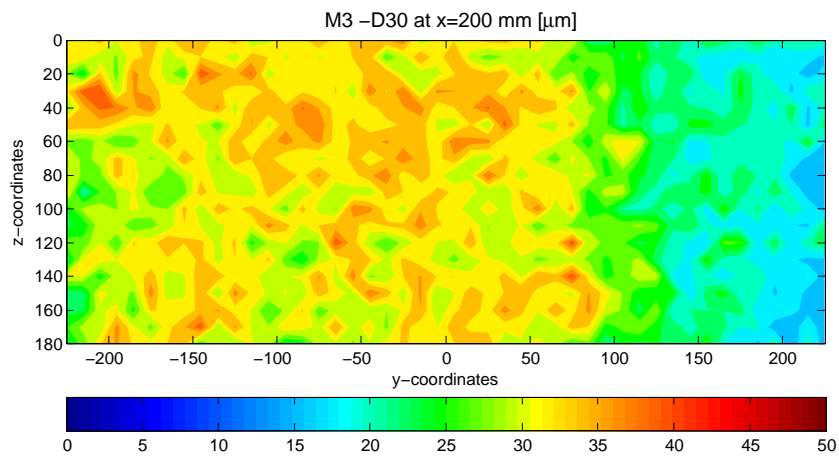


**Figure D.4:** Droplet volume mean diameter ( $D_{30}$ ) distribution of configuration M3 at  $x = 200$  mm, measured by PDA.

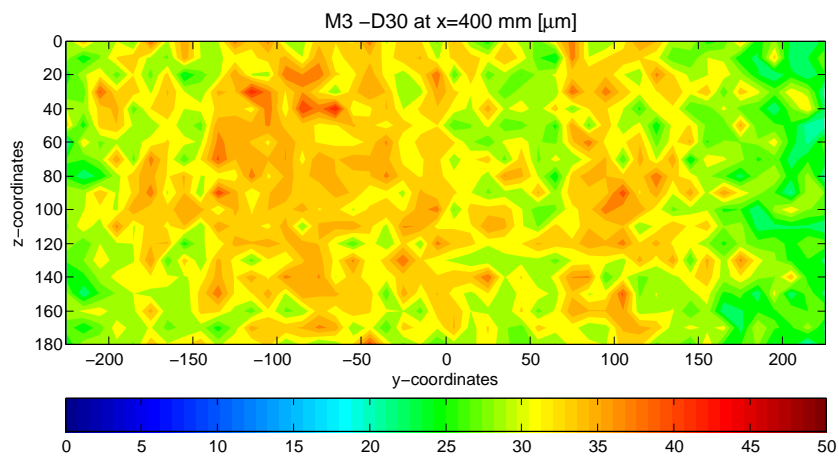


**Figure D.5:** Droplet volume mean diameter ( $D_{30}$ ) distribution of configuration M3 at  $x = 400$  mm, measured by PDA.

# Selected experimental results, Configuration M4

---

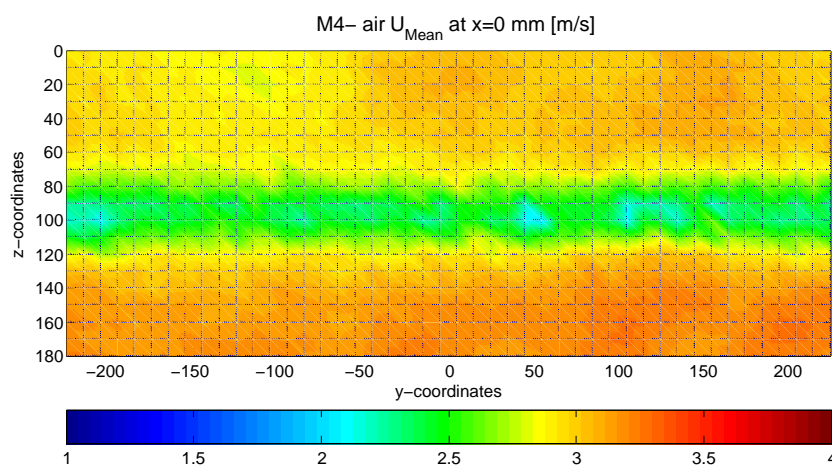


**Figure E.1:** Mean air velocity distribution of configuration M4 at  $x = 0$  mm, measured by LDV.

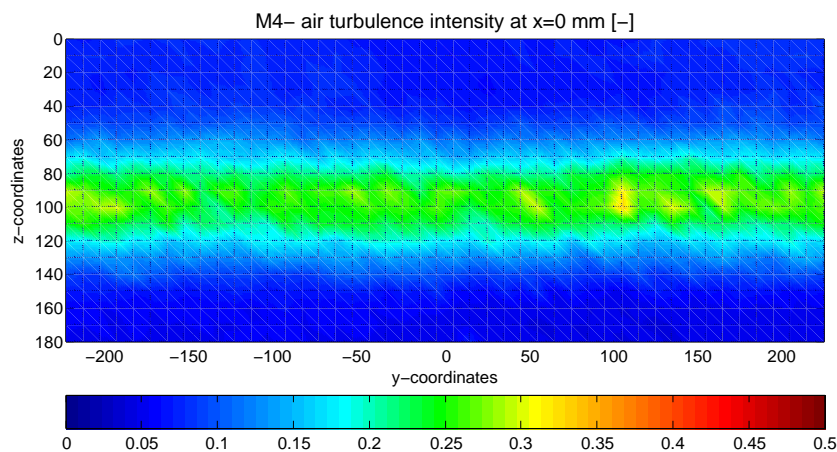


**Figure E.2:** Air turbulence intensity of configuration M4 at  $x = 0$  mm, measured by LDV.

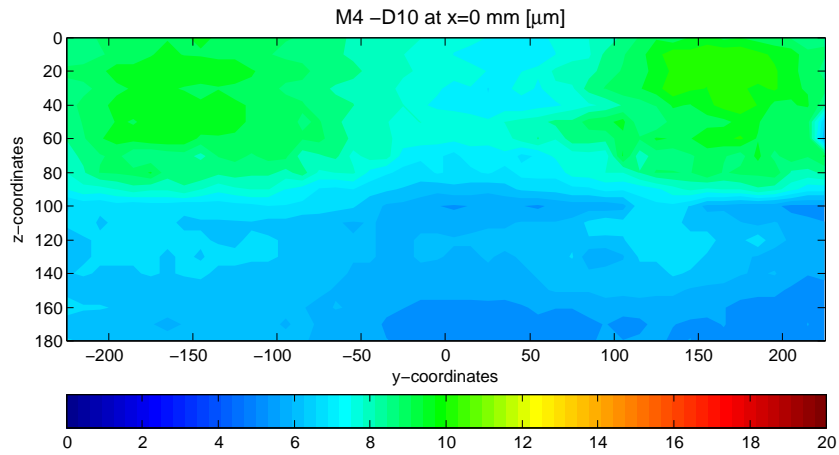


**Figure E.3:** Droplet mean diameter ( $D_{10}$ ) distribution of configuration M4 at  $x = 0$  mm, measured by PDA.

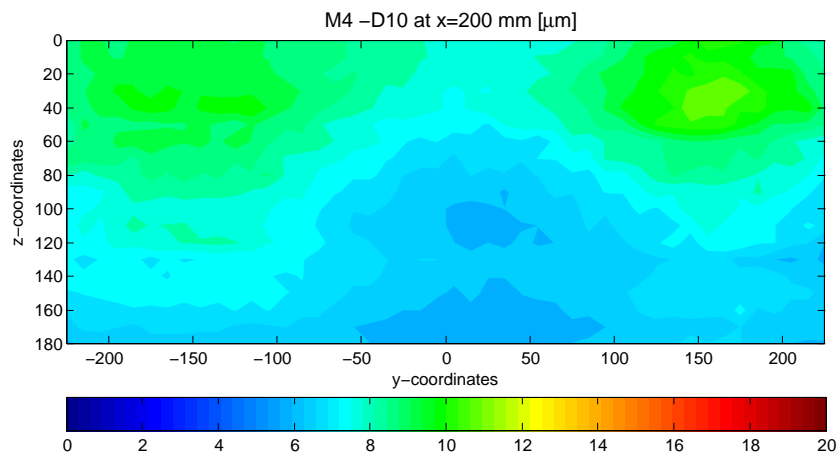


**Figure E.4:** Droplet mean diameter ( $D_{10}$ ) distribution of configuration M4 at  $x = 200$  mm, measured by PDA.

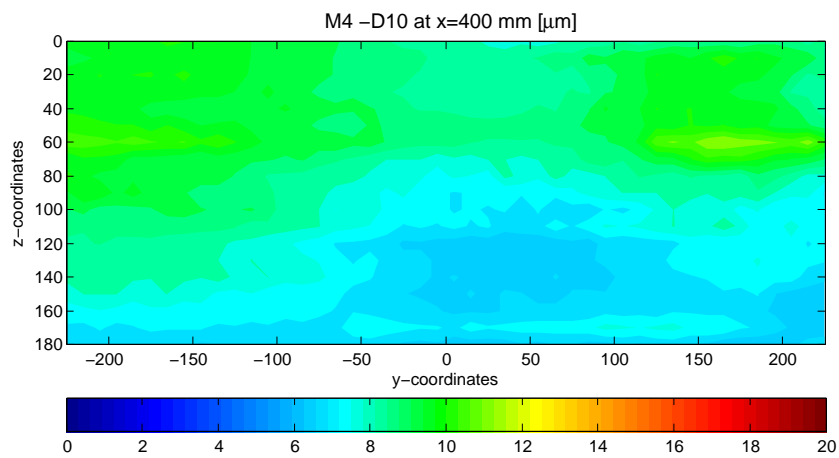


**Figure E.5:** Droplet mean diameter ( $D_{10}$ ) distribution of configuration M4 at  $x = 400$  mm, measured by PDA.

# List of Figures

1.1	The rain dance is out of date. . . . .	1
1.2	Typical number density values belonging to different droplet sizes and the <b>dominating processes</b> of cloud droplet size development. . . . .	2
1.3	Water cycle. Image from the U.S. Geological Survey’s (USGS) <a href="http://ga.water.usgs.gov/edu">http://ga.water.usgs.gov/edu</a> . . . . .	3
1.4	Schematic curves of droplet growth time. Regions with dominant mechanisms are also indicated. . . . .	4
1.5	Condensational water droplet volume growth with $S = 101\%$ and $d_0 = 12.5 \mu\text{m}$ . . . . .	13
2.1	Representation of light refraction. . . . .	22
2.2	Image of an aorta model, in which the refractive index of the liquid has been matched to that of the silicon block in order to carry out LDV measurements. Left, without liquid filling, in the middle filled with water and on the right when filling with refractive index matched liquid ( <b>Wunderlich et al., 2007</b> ). . . . .	24
2.3	Left: original calibration pattern; middle: distorted image behind a curved surface; right: corrected image reconstructed from that in the middle ( <b>Pap et al., 2009</b> ). . . . .	24
2.4	Droplet size distribution of the PEG fog, measured in the wind tunnel by means of PDA. . . . .	26
2.5	Settling velocity of the considered particles in air as a function of time. . . . .	28
2.6	Illustration of the normalized deviation between different particle and fluid trajectories ( <b>Bordás et al., 2008</b> ). . . . .	31
2.7	Amplitude ratio $\eta$ between particle and fluid velocity against oscillation frequency of the flow. . . . .	34
2.8	Limit frequency versus particle diameter. The amplitude ratio $\eta$ is fixed to a value of 95%. . . . .	35
2.9	Iso-surfaces of the simulated flow field in the test section of the wind tunnel. . . . .	37
2.10	Dimensionless deviation of trajectories from the ideal one for the considered tracer particles. . . . .	38
3.1	Göttingen-type two-phase wind tunnel with closed test section. The test section is shown in Fig. 3.2 in detail. . . . .	42

3.2	Transparent test section with optional passive grid and cylindrical bluff body. The coordinate system and measurement planes are marked as well. . . . .	43
3.3	Close view of the spray head (left) and injected spray (right)..	44
3.4	Mean axial velocity (left) and turbulence intensity (right) distribution of the air flow, without droplet injection at the entrance of the measurement section – 630 mm behind the nozzle ( $x = 0$ mm). The circles show the influence of the injection and the dashed rectangle the selected measurement section, with minimal influence of the injection system. . . . .	44
3.5	Droplet size distribution and suitable log-normal distribution function at $x = 0, y = -5, z = 90$ , measured by PDA. . . . .	45
3.6	<b>Measured velocity</b> at the entrance of the wind tunnel test section for different <b>input voltage</b> functions vs. time during pulsed operation. . . . .	48
3.7	Photos of the grid, of the cylinder and of the dual spray injection mounted in the test section of the wind tunnel. . . . .	49
3.8	Schematics of configurations <b>M1–M4</b> , respectively. . . . .	50
3.9	Configuration <b>M1</b> . . . . .	51
3.10	Configuration <b>M2</b> . . . . .	53
3.11	Configuration <b>M3</b> . . . . .	60
3.12	Configuration <b>M4</b> . . . . .	61
3.13	Schematic of an LDV system . . . . .	63
3.14	Schematic of a PDA system . . . . .	64
3.15	Confidence of Phase-Doppler linearity vs. scattering angle . . . . .	66
3.16	Schematic of a PIV system . . . . .	67
3.17	Sketch of the PIV measurement setup for the measurement in a transversal plane. . . . .	68
3.18	Schematic of a Shadowgraphy system . . . . .	69
4.1	Exemplary applications of the advanced grid generation tool, left from <b>Witte et al. (2006)</b> , right cross section in the wind tunnel. . . . .	74
4.2	Example for a phase-averaged measurement in a medical model by means of LDV and a pressure transducer. The threshold for phase-averaging is applied on the instantaneous pressure values. The resulting phase decomposed velocities are presented on the right with a fitted velocity curve. . . . .	76
4.3	Flow chart of the LDDV working principle. . . . .	77
4.4	Typical pedestal signal of a passing droplet. . . . .	78

---

4.5	Probability density function of the measured droplet number density at the entrance of the test section as a function of the size class, including the measured standard deviation as an error bar. . . . .	82
4.6	Distribution of droplet centricity for the configuration <b>M3</b> at $x = 0, y = 0, z = 0$ . . . . .	84
4.7	Example for an unsure collision event: particle partly out of focus. . . . .	85
4.8	Some exemplary collision events. . . . .	85
4.9	Recording of the calibration plate (left) and the dewarped image (right). . . . .	87
4.10	Averaged vector fields before (top left) and after (top right) correction. The corrected vector field is shown again in the bottom with the same aspect ratio in both coordinate directions and a contour plot in the background with color coding, representing the vector lengths. . . . .	88
4.11	Illustration of the distortion, caused by an oblique view on the laser plane. . . . .	90
5.1	Convergence of the arithmetic mean and volume mean diameters measured by PDA. The volume mean diameter converges at around 8 000 samples. . . . .	92
5.2	Mean diameter profile across the measurement section at $x = 0, z = 0$ , measured by means of PDA. . . . .	93
5.3	Mean longitudinal velocity profile of the droplets across the measurement section at $x = 0, z = 0$ , measured by means of PDA. . . . .	94
5.4	Mean longitudinal velocity distribution of the air phase at $x = 0$ , measured by means of LDV. . . . .	95
5.5	Instantaneous (top) and averaged (bottom) velocity vector fields and contour plots of the air phase at $y = 0$ for the configuration <b>M3</b> , measured by means of PIV. . . . .	96
5.6	Mean turbulence intensity distribution of the air phase in $x$ -direction at $x = 0$ , measured by means of LDV. . . . .	97
5.7	Distribution of the calculated energy dissipation rate from 300 PIV vector fields in the $y = 0$ plane. . . . .	98
5.8	Calculated energy cascade of the flow. Post processing of a PIV measurement in the $y = 0$ plane. . . . .	99
5.9	Velocity-diameter correlation of the water droplets for the configuration <b>M1</b> at the $x = 0, y = 5, z = 0$ mm position. . . . .	101



5.10	Mean droplet velocity distribution in the planes $x = 0$ , $x = 200$ and $x = 400$ of the configuration <b>M1</b> , measured by means of PDA. . . . .	102
5.11	Droplet number density per unit volume in $1/\text{cm}^3$ at $x = 0$ calculated from the PDA results as described by Roisman and Tropea (2001) and discussed in Chapter 4. . . . .	103
5.12	Influence of the discretization resolution on the calculated theoretical collision rate. . . . .	104
5.13	Collision rate matrix of the discretized droplet size distribution. . . . .	105
5.14	Comparison of the measured (blue, green) and theoretical (red) collision rates per unit volume for the configuration <b>M3</b> (left) and <b>M4</b> (right) at different $z$ -heights. . . . .	107
5.15	Mean and volume mean diameter development along the $x$ -axis for the configuration <b>M3</b> , measured by means of PDA. The increase in mean droplet sizes can be recognized. . . . .	108
5.16	Mean longitudinal velocity distribution of the droplets at $x = 0$ , measured by means of PDA, for the configurations <b>M1</b> , <b>M2</b> , <b>M3</b> and <b>M4</b> , respectively. . . . .	111
5.17	Screenshot of the database: navigation page containing the different experimental configurations. . . . .	113
5.18	Instantaneous velocity field obtained from the simulation, with the outflow boundary of the measurement section ( $x = 400$ mm) on the right hand side. . . . .	117
5.19	Calibration of the model parameters $C_{\text{brown}}$ and $C_{\text{shear}}$ . The green curves are the averaged experimental data at the outlet of the measurement volume, all other curves are simulation results. . . . .	118
B.1	Mean air velocity distribution of configuration <b>M1</b> at $x = 0$ mm, measured by LDV. . . . .	127
B.2	Air turbulence intensity of configuration <b>M1</b> at $x = 0$ mm, measured by LDV. . . . .	127
B.3	Turbulence intensity distribution of the disperse phase of configuration <b>M1</b> at $x = 0$ mm, measured by PDA. . . . .	128
B.4	Turbulence intensity distribution of the disperse phase of configuration <b>M1</b> at $x = 200$ mm, measured by PDA. . . . .	128
B.5	Turbulence intensity distribution of the disperse phase of configuration <b>M1</b> at $x = 400$ mm, measured by PDA. . . . .	128
C.1	Mean air velocity distribution of configuration <b>M2</b> at $x = 0$ mm, measured by LDV. . . . .	129

---

C.2	Air turbulence intensity of configuration <b>M2</b> at $x = 0$ mm, measured by LDV. . . . .	129
C.3	Mean droplet velocity distribution of configuration <b>M2</b> at $x = 0$ mm, measured by PDA. . . . .	130
C.4	Mean droplet velocity distribution of configuration <b>M2</b> at $x = 200$ mm, measured by PDA. . . . .	130
C.5	Mean droplet velocity distribution of configuration <b>M2</b> at $x = 400$ mm, measured by PDA. . . . .	130
D.1	Mean air velocity distribution of configuration <b>M3</b> at $x = 0$ mm, measured by LDV. . . . .	131
D.2	Air turbulence intensity of configuration <b>M3</b> at $x = 0$ mm, measured by LDV. . . . .	131
D.3	Droplet volume mean diameter ( $D_{30}$ ) distribution of configuration <b>M3</b> at $x = 0$ mm, measured by PDA. . . . .	132
D.4	Droplet volume mean diameter ( $D_{30}$ ) distribution of configuration <b>M3</b> at $x = 200$ mm, measured by PDA. . . . .	132
D.5	Droplet volume mean diameter ( $D_{30}$ ) distribution of configuration <b>M3</b> at $x = 400$ mm, measured by PDA. . . . .	132
E.1	Mean air velocity distribution of configuration <b>M4</b> at $x = 0$ mm, measured by LDV. . . . .	133
E.2	Air turbulence intensity of configuration <b>M4</b> at $x = 0$ mm, measured by LDV. . . . .	133
E.3	Droplet mean diameter ( $D_{10}$ ) distribution of configuration <b>M4</b> at $x = 0$ mm, measured by PDA. . . . .	134
E.4	Droplet mean diameter ( $D_{10}$ ) distribution of configuration <b>M4</b> at $x = 200$ mm, measured by PDA. . . . .	134
E.5	Droplet mean diameter ( $D_{10}$ ) distribution of configuration <b>M4</b> at $x = 400$ mm, measured by PDA. . . . .	134



# List of Tables

1.1	Summary of the wind tunnels described in the present section, including the wind tunnel of the University of Magdeburg, described later in Chapter 3. . . . .	8
1.2	Summary and hints for the equations of the collision theory based on those of <a href="#">Mersmann (2001)</a> . . . . .	18
2.1	Properties of potential tracer particles for gas flows. Both theoretically available and practically <b>considered</b> . . . . .	27
2.2	Terminal velocity values for different tracer particles ( $\vartheta = 20^\circ\text{C}$ , $p = 1$ bar). . . . .	28
2.3	Characteristic timescale of the flow and calculated relaxation times and Stokes numbers. . . . .	30
2.4	Frequency limits of a flow, in which the particles can react to changes with an amplitude ratio of 95% . . . . .	35
3.1	Main properties of the AK4a A/D converter and ADA2 A/D–D/A converter. . . . .	46
3.2	Main properties of the pressure transducer and the hygrometer. . . . .	47
3.3	Main properties of the SETRA pressure transducers. . . . .	48
3.4	Main properties of the considered passive grids. The finally selected one is marked as bold. . . . .	56
3.5	Predicted mean values for the considered passive grids at the entrance of the test section. . . . .	58
3.6	Summary of theoretically predicted values for the configurations <b>M1–M4</b> . . . . .	62
3.7	Properties of the LDV/PDA system. . . . .	65
3.8	Hints for PDA settings of different orders of refractions ( <a href="#">Dantec Dynamics, 2002</a> ). . . . .	65
3.9	PIV hardware components. . . . .	68
3.10	Batch processing settings in DaVis. . . . .	70
3.11	Shadowgraphy hardware components. . . . .	70
4.1	Calculation of detection volume diameter and reference area. . . . .	81

---

5.1	Measured and deduced values of the continuous phase for all the configurations in the wind tunnel at $x = 0$ . The turbulent energy dissipation rates were calculated by means of PIV measurements, as described in this Chapter and the turbulence scales were deduced from those. . . . .	100
5.2	Mean diameters and their applications, following Lefebvre (1989). The order can be determined by summing the numbers in the index of $d$ . E.g., for Sauter mean diameter, the order is $3+2 = 5$ .	101
5.3	Properties required for the calculation of theoretical collision rates at the discussed measurement points, as measured by PDA.	105
5.4	Experimentally determined collision rates together with their standard deviation $\sigma$ and comparison with theoretical predictions.	106
5.5	Typical values in cumulus clouds and the corresponding ones in the wind tunnel. . . . .	110
A.1	Wind tunnel data sheet. . . . .	126

# Bibliography

- J. Abrahamson. Collision rates of small particles in a vigorously turbulent fluid. *Chemical Engineering Science*, 30(11):1371–1379, 1975.
- R. J. Adrian. Particle-imaging techniques for experimental fluid mechanics. *Annual Reviews in Fluid Mechanics*, 23(1):261–304, 1991.
- R. J. Adrian. Twenty years of particle image velocimetry. *Experiments in Fluids*, 39(2):159–169, 2005.
- R. A. Antonia, T. Zhou, and Y. Zhu. Three-component vorticity measurements in a turbulent grid flow. *Journal of Fluid Mechanics*, 374:29–57, 1998.
- S. Ayyalasomayajula, A. Gylfason, L. R. Collins, E. Bodenschatz, and Z. Warhaft. Lagrangian measurements of inertial particle accelerations in grid generated wind tunnel turbulence. *Physical Review Letters*, 97(14):144507, 2006.
- L. Baranyi, S. Szabó, B. Bolló, and R. Bordás. Analysis of flow around a heated circular cylinder. *Journal of Mechanical Science and Technology*, 23:1829–1834, 2009.
- A. B. Basset. *Treatise on Hydrodynamics*, volume 2. Deighton, Bell & Co., Cambridge, 1888.
- G. Batchelor and A. Townsend. Decay of turbulence in the final period. *Proceedings of the Royal Society of London. Series A, Mathematical and Physical Sciences*, pages 527–543, 1948.
- K. V. Beard and H. T. Ochs III. Warm-rain initiation: An overview of microphysical mechanisms. *Journal of Applied Meteorology*, 32(4):608–625, 1993.
- K. V. Beard and H. R. Pruppacher. A determination of the terminal velocity and drag of small water drops by means of a wind tunnel. *Journal of Atmospheric Sciences*, 26(5):1066–1072, 1969.
- K. V. Beard and H. R. Pruppacher. A wind tunnel investigation of the rate of evaporation of small water drops falling at terminal velocity in air. *Journal of the Atmospheric Sciences*, 28(8):1455–1464, 1971.

- J. Bhatia, J. Domnick, F. Durst, and C. Tropea. Phase-Doppler-anemometry and the log-hyperbolic distribution applied to liquid sprays. *Particle & Particle Systems Characterization*, 5(4):153–164, 1988.
- R. Bordás. *Separate LDA velocity measurement of simultaneously existing tracer particles and air bubbles in a water flow*. Diploma Thesis, Budapest University of Technology and Economics, 2005.
- R. Bordás, A. Öncül, K. Zähringer, and D. Thévenin. Optical measurements in two-phase flows involving particles. In G. Kompenhans and A. Schröder, editors, *12th International Symposium on Flow Visualization*, pages 025/1–025/10, Göttingen, Germany, 2006.
- R. Bordás, T. Hagemeyer, and D. Thévenin. Experimental quantification of droplet collision rates in turbulent sprays. In *7th International Symposium on Turbulence and Shear Flow Phenomena*, Ottawa, Canada, 2011. accepted for presentation.
- R. Bordás and D. Thévenin. Modeling cumulus clouds in a two-phase wind tunnel. In *European Geosciences Union General Assembly EGU 2009*, Vienna, Austria, 2009.
- R. Bordás, C. Bendicks, R. Kuhn, B. Wunderlich, D. Thévenin, and B. Michaelis. Coloured tracer particles employed for 3D-PTV in gas flows. In J. Prenel and Y. Bailly, editors, *13th International Symposium on Flow Visualization*, pages 093.1–12, Nice, France, 2008.
- R. Bordás, K. Hanke, P. Bencs, and D. Thévenin. 2D-PIV measurements in a two-phase wind tunnel normal to the main flow. In L. Lehoczky, editor, *XXIII. microCAD International Scientific Conference*, pages 39–46, Miskolc, Hungary, 2009.
- R. Bordás, T. Hagemeyer, and D. Thévenin. Experimental investigation of droplet-droplet interactions. In *23rd European Conference on Liquid Atomization and Spray Systems*, pages 198.1–6, Brno, Czech Republic, 2010.
- R. Bordás, T. Hagemeyer, B. Wunderlich, and D. Thévenin. Droplet collisions and interaction with the turbulent flow within a two-phase wind tunnel. *Physics of Fluids*, 2011a. accepted for publication.
- R. Bordás, V. John, E. Schmeier, and D. Thévenin. Measurement and simulation of a droplet population in a turbulent flow field. *Computers and Fluids*, 2011b. submitted.

- V. Borue and S. A. Orszag. Self-similar decay of three-dimensional homogeneous turbulence with hyperviscosity. *Physical Review E*, 51(2):856–859, 1995.
- J. Boussinesq. *Théorie analytique de la chaleur, mise en harmonie avec la thermodynamique et avec la théorie mécanique de la lumière*, volume 2. Gauthier-Villars, Paris, 1903.
- J. Calbó and J. Sabburg. Feature extraction from whole-sky ground-based images for cloud-type recognition. *Journal of Atmospheric and Oceanic Technology*, 25(1):3–14, 2008.
- T. R. Camp and P. C. Stein. Velocity gradients and internal work in fluid motion. *Journal of the Boston Society of Civil Engineers*, 85:219–37, 1943.
- A. Celani, G. Falkovich, A. Mazzino, and A. Seminara. Droplet condensation in turbulent flows. *EPL (Europhysics Letters)*, 70:775–781, 2005.
- G. Comte-Bellot and S. Corrsin. The use of a contraction to improve the isotropy of grid-generated turbulence. *Journal of Fluid Mechanics*, 25(04):657–682, 1966.
- S. Corrsin. *Turbulence: experimental methods*, volume 8 of *Handbuch der Physik*. Springer, Berlin, 1963.
- C. Crowe. *Multiphase Flow Handbook*. Taylor and Francis Group, 2006.
- C. Crowe, M. Sommerfeld, and Y. Tsujinaka. *Multiphase Flows with Droplets and Particles*. CRC Press, 1998.
- N. Damaschke, H. Nobach, N. Semidetnov, and C. Tropea. Optical particle sizing in backscatter. *Applied optics*, 41(27):5713–5727, 2002.
- Dantec Dynamics. BSA Flow Software Installation and User’s guide, Ver. 4.10, 2002.
- F. C. De Almeida. The collisional problem of cloud droplets moving in a turbulent environment-Part II: Turbulent collision efficiencies. *Journal of the Atmospheric Sciences*, 36(8):1564–1576, 1979.
- A. Ducci, E. Konstantinidis, S. Balabani, and M. Yianneskis. Direct measurement of the turbulent kinetic energy viscous dissipation rate behind a grid and a circular cylinder. In *Proc. 11th Int. Symp. on Applications of Laser Techniques to Fluid Mechanics, Lisbon, Portugal*, pages 1–12, 2002.



- G. Erpul, D. Gabriels, and D. Janssens. Assessing the drop size distribution of simulated rainfall in a wind tunnel. *Soil & Tillage Research*, 45(3-4):455–463, 1998.
- G. Erpul, L. D. Norton, and D. Gabriels. Raindrop-induced and wind-driven soil particle transport. *CATENA*, 47(3):227–243, 2002.
- G. Erpul, L. D. Norton, and D. Gabriels. Splash-saltation trajectories of soil particles under wind-driven rain. *Geomorphology*, 59(1-4):31–42, 2004.
- G. Erpul, D. Gabriels, and L. D. Norton. Sand detachment by wind-driven raindrops. *Earth Surface Processes and Landforms*, 30(2):241–250, 2005.
- J. Fan, R. Zhang, G. Li, W. Tao, and X. Li. Simulations of cumulus clouds using a spectral microphysics cloud-resolving model. *Journal of Geophysical Research-Atmospheres*, 112(D4):D04201, 2007.
- J. R. Fessler, J. D. Kulick, and J. K. Eaton. Preferential concentration of heavy particles in a turbulent channel flow. *Physics of Fluids*, 6(11):3742–3749, 1994.
- J. P. Fugal, R. A. Shaw, E. W. Saw, and A. V. Sergeev. Airborne digital holographic system for cloud particle measurements. *Applied Optics*, 43(32):5987–5995, 2004.
- N. Fukuta and L. Walter. Kinetics of hydrometeor growth from a vapor-spherical model. *Journal of the Atmospheric Sciences*, 27(8):1160–1172, 1970.
- D. Gabriels, W. Cornelis, I. Pollet, T. Van Coillie, and M. Ouessar. The I.C.E. wind tunnel for wind and water erosion studies. *Soil Technology*, 10(1):1–8, 1997.
- W. George. The decay of homogeneous isotropic turbulence. *Physics of Fluids A*, 4(7):1492–1509, 1992.
- P. Glantz, K. J. Noone, and S. R. Osborne. Comparisons of airborne CVI and FSSP measurements of cloud droplet number concentrations in marine stratocumulus clouds. *Journal of Atmospheric and Oceanic Technology*, 20(1):133–142, 2003.
- J. Goff and S. Gratch. Low-pressure properties of water from -160 to 212 F. *Transactions of the American Society of Heating and Ventilating Engineers*, 51:95–122, 1946.

- W. Grabowski. Coupling cloud processes with the large-scale dynamics using the cloud-resolving convection parameterization (CRCP). *Journal of the Atmospheric Sciences*, 58(9):978–997, 2001.
- H. L. Grant and I. C. T. Nisbet. The inhomogeneity of grid turbulence. *Journal of Fluid Mechanics*, 2(3):263–272, 1956.
- I. Grant, X. Pan, X. Wang, and N. Stewart. Correction for viewing angle applied to PIV data obtained in aerodynamic blade vortex interaction studies. *Experiments in Fluids*, 18(1):95–99, 1994.
- T. Hagemeyer, R. Bordás, P. Bencs, B. Wunderlich, and D. Thévenin. Determination of droplet size and velocity distributions in a two-phase wind tunnel. In P. Bailly and J. P. Prenel, editors, *ISFV13 - 13th International Symposium on Flow Visualization*, pages 094/1–094/10, Nice, France, 2008.
- Y. Y. Hardalupas and S. Horender. Phase Doppler anemometer for instantaneous measurements of droplet concentration. In *Proceedings of the 10th International Symposium on Application of Laser Techniques to Fluid Mechanics*, pages 23.1/1–13, Lisboa, Portugal, 2000.
- J. T. Heineck, G. K. Yamauchi, A. J. Wadcock, L. M. Lourenco, and A. Abrego. Application of three-component PIV to a hovering rotor wake. In *American Helicopter Society*, volume 56, pages 375–390, 2000.
- J. O. Hinze. *Turbulence*. McGraw-Hill Book Company, 1975.
- A. T. Hjelmfelt and L. F. Mockros. Motion of discrete particles in a turbulent fluid. *Applied Scientific Research*, 16(1):149–161, 1966.
- H. Hulburt and S. Katz. Some problems in particle technology – a statistical mechanical formulation. *Chemical Engineering Science*, 19:555–574, 1964.
- V. John and G. Matthies. MooNMD - a program package based on mapped finite element methods. *Computing and Visualization in Science*, 6:163–170, 2004.
- D. B. Johnson. The onset of effective coalescence growth in convective clouds. *Quarterly Journal of the Royal Meteorological Society*, 119(513):925–933, 1993.
- H. J. Kampe. Visibility and liquid water content in clouds in the free atmosphere. *Journal of the Atmospheric Sciences*, 7(1):54–57, 1950.
- R. Kapulla and S. Najera. Operation conditions of a phase Doppler anemometer: droplet size measurements with laser beam power, photomultiplier volt-

- age, signal gain and signal-to-noise ratio as parameters. *Measurement Science and Technology*, 17:221–227, 2006.
- R. Kapulla, M. Trautmann, S. Güntay, A. Dehbi, and D. Suckow. Comparison between phase-Doppler anemometry and shadowgraphy systems with respect to solid-particle size distribution measurements. In D. Dopheide, H. Müller, V. Strunck, B. Ruck, and A. Leder, editors, *Lasermethoden in der Strömungsmesstechnik*, pages 3/1–3/6, Braunschweig, Germany, GALA, 2006.
- A. P. Khain. Notes on state-of-the-art investigations of aerosol effects on precipitation: a critical review. *Environmental Research Letters*, 4(1):015004, 2009.
- O. Kisi and J. Shiri. Precipitation forecasting using wavelet-genetic programming and wavelet-neuro-fuzzy conjunction models. *Water Resources Management*, pages 1–18, 2011.
- Y. Kogan. Drop size separation in numerically simulated convective clouds and its effect on warm rain formation. *Journal of the Atmospheric Sciences*, 50(9):1238–1253, 1993.
- P. M. Korczyk, T. A. Kowalewski, and S. P. Malinowski. Investigations of turbulence statistics in the laboratory model of an atmospheric cloud. In G. Kompenhans and A. Schröder, editors, *12th International Symposium on Flow Visualization*, pages 1–10, Göttingen, Germany, 2006.
- H. Kraus. *Die Atmosphäre der Erde: Eine Einführung in die Meteorologie*. Springer, 2004.
- F. E. Kruis and K. A. Kusters. The collision rate of particles in turbulent flow. *Chemical Engineering Communications*, 158(1):201–230, 1997.
- J. Kussin. *Experimentelle Studien zur Partikelbewegung und Turbulenzmodifikation in einem horizontalen Kanal bei unterschiedlichen Wandrauigkeiten*. Ph.D. Thesis, Martin-Luther-Universität Halle-Wittenberg, 2004.
- A. La Porta, G. Voth, A. Crawford, J. Alexander, and E. Bodenschatz. Fluid particle accelerations in fully developed turbulence. *Nature*, 409(6823):1017–1019, 2001.
- L. D. Landau and E. M. Lifschitz. *Lehrbuch der theoretischen Physik, Band VI, Sect. 59: Hydrodynamik*. Akademie-Verlag, Berlin, 1966.

- I. Langmuir. The production of rain by a chain reaction in cumulus clouds at temperatures above freezing. *Journal of the Atmospheric Sciences*, 5(5): 175–192, 1948.
- E. M. Laws and J. L. Livesey. Flow through screens. *Annual Reviews in Fluid Mechanics*, 10(1):247–266, 1978.
- A. Lefebvre. *Atomization and sprays*. CRC Press, 1989.
- R. List. Der Hagelversuchskanal. *Zeitschrift für Angewandte Mathematik und Physik (ZAMP)*, 10(4):381–415, 1959. ISSN 0044-2275.
- M. Manton. The equation of motion for a small aerosol in a continuum. *Pure and Applied Geophysics*, 115(3):547–559, 1977.
- Z. Mátrai. *Laser-Doppler-Velocimetry Measurements in Artificial Medical Models*. B.Sc. Thesis, University of Miskolc, 2009.
- M. Maxey and J. Riley. Equation of motion for a small rigid sphere in a nonuniform flow. *Physics of Fluids*, 26:883–889, 1983.
- M. R. Maxey. The gravitational settling of aerosol particles in homogeneous turbulence and random flow fields. *Journal of Fluid Mechanics*, 174:441–465, 1987.
- W. McComb. *The physics of fluid turbulence*. Oxford University Press, USA, 1992.
- A. McNaught and A. Wilkinson. *Compendium of Chemical Terminology - The Gold Book*. IUPAC. Blackwell Science, 1997.
- A. Melling. Tracer particles and seeding for Particle Image Velocimetry. *Measurement Science and Technology*, 8(12):1406–1416, 1997.
- A. Mersmann. *Crystallization technology handbook*. Marcel Dekker Inc, 2001.
- N. P. Mikhailova, E. U. Repik, and Y. P. Sosedko. Scales of grid and honeycomb-generated turbulence. *Fluid Dynamics*, 36(1):69–79, 2001.
- M. S. Mohamed and J. C. Larue. The decay power law in grid-generated turbulence. *Journal of Fluid Mechanics*, 219:195–214, 1990.
- P. Mohr, B. Taylor, and D. Newell. CODATA recommended values of the fundamental physical constants: 2006. *Reviews of Modern Physics*, 80(2): 633–730, 2008.

- L. Mydlarski and Z. Warhaft. On the onset of high-Reynolds-number grid-generated wind tunnel turbulence. *Journal of Fluid Mechanics*, 320:331–368, 1996.
- J. Nogueira, A. Lecuona, and P. A. Rodriguez. Data validation, false vectors correction and derived magnitudes calculation on PIV data. *Measurement Science and Technology*, 8(12):1493–1501, 1997.
- C. Norberg. Flow around a circular cylinder: aspects of fluctuating lift. *Journal of Fluids and Structures*, 15(3-4):459–469, 2001.
- C. W. Oseen. *Hydrodynamik*. Akademische Verlagsgesellschaft m. b. H., Leipzig, 1927.
- N. T. Ouellette, H. Xu, M. Bourgoïn, and E. Bodenschatz. An experimental study of turbulent relative dispersion models. *New Journal of Physics*, 8(6):109, 2006.
- N. Özyilmaz. *Lattice Boltzmann Computations of Grid-Generated Turbulence*. Ph.D. Thesis, Friedrich-Alexander-Universität Erlangen-Nürnberg, 2010.
- N. Özyilmaz, K. N. Beronov, and A. Delgado. Characterization of the dissipation tensor from DNS of grid-generated turbulence. In S. Wagner, M. Steinmetz, A. Bode, and M. Brehm, editors, *High Performance Computing in Science and Engineering*, pages 315–323. Springer, 2009.
- I. R. Paluch, C. A. Knight, and L. J. Miller. Cloud liquid water and radar reflectivity of nonprecipitating cumulus clouds. *Journal of the Atmospheric Sciences*, 53(11):1587–1603, 1996.
- E. Pap, G. Janiga, and R. Bordás. Möglichkeiten zur rechnerischen Korrektur der optischen Abbildungsverzerrungen bei PIV. In L. Lehoczky, editor, *XXIII. microCAD International Scientific Conference*, pages 77–86, Miskolc, Hungary, 2009.
- M. Pilch and C. Erdman. Use of breakup time data and velocity history data to predict the maximum size of stable fragments for acceleration-induced breakup of a liquid drop. *International Journal of Multiphase Flow*, 13(6):741–757, 1987.
- M. Pinsky and A. Khain. Formation of inhomogeneity in drop concentration induced by the inertia of drops falling in a turbulent flow, and the influence of the inhomogeneity on the drop-spectrum broadening. *Quarterly Journal of the Royal Meteorological Society*, 123(537):165–186, 1997.

- M. Pinsky, A. Khain, and M. Shapiro. Collisions of small drops in a turbulent flow. Part I: Collision efficiency. Problem formulation and preliminary results. *Journal of the Atmospheric Sciences*, 56(15):2585–2600, 1999.
- M. Pinsky, A. Khain, and H. Krugliak. Collisions of cloud droplets in a turbulent flow. Part V: Application of detailed tables of turbulent collision rate enhancement to simulation of droplet spectra evolution. *Journal of the Atmospheric Sciences*, 65(2):357–374, 2008.
- M. B. Pinsky and A. P. Khain. Simulations of drop fall in a homogeneous isotropic turbulent flow. *Atmospheric Research*, 40(2-4):223–259, 1996.
- S. Pope. *Turbulent flows*. Cambridge Univ. Press, 2000.
- A. Protat, D. Bouniol, J. Delanoë, E. O’Connor, P. May, A. Plana-Fattori, A. Hasson, U. Gørsdorf, and A. Heymsfield. Assessment of CloudSat reflectivity measurements and ice cloud properties using ground-based and airborne cloud radar observations. *Journal of Atmospheric and Oceanic Technology*, 26:1717–1741, 2009.
- H. R. Pruppacher and K. V. Beard. A wind tunnel investigation of the internal circulation and shape of water drops falling at terminal velocity in air. *Quarterly Journal of the Royal Meteorological Society*, 96(408):247–256, 1970.
- H. R. Pruppacher and J. D. Klett. *Microphysics of Clouds and Precipitation*, volume 18. Kluwer Academic Publishers, 1997.
- H. R. Pruppacher and M. Neiburger. The UCLA cloud tunnel. In *Proc. International Conference on Cloud Physics*, pages 389–392, 1968.
- M. Reeves and N. J. Lawson. Evaluation and correction of perspective errors in endoscopic PIV. *Experiments in Fluids*, 36(5):701–705, 2004.
- M. Reeves, D. Towers, B. Tavender, and C. Buckberry. A technique for routine, cycle-resolved 2-D flow measurement and visualisation within SI engine cylinders in an engine development environment. In *10th International Symposium on Applications of Laser Techniques to Fluid Mechanics*, Lisboa, Portugal, 2000.
- R. R. Rogers and M. K. Yau. *A short course in cloud physics*. International series in natural philosophy. Butterworth-Heinemann, Oxford, 1996.
- I. V. Roisman and C. Tropea. Drops distribution and flux measurements in sprays using the phase Doppler technique. In *Proceedings of the 10th*

- International Symposium on Application of Laser Techniques to Fluid Mechanics*, pages 23.2/1–12, Lisboa, Portugal, 2000.
- I. V. Roisman and C. Tropea. Flux measurements in sprays using phase Doppler techniques. *Atomization and Sprays*, 11(6):667–700, 2001.
- B. Ruck and B. Makiola. Einfluss der Teilchengröße auf die Signalinformation in der Laser-Doppler-Anemometrie. *Technisches Messen*, 57:284–295, 1990.
- P. Saarenrinne and M. Piirto. Turbulent kinetic energy dissipation rate estimation from PIV velocity vector fields. *Experiments in Fluids*, 29(7):300–307, 2000.
- P. G. Saffman and J. S. Turner. On the collision of drops in turbulent clouds. *Journal of Fluid Mechanics*, 1(1):16–30, 1956.
- E. W. Saw, R. A. Shaw, S. Ayyalasomayajula, P. Y. Chuang, and Á. Gylfason. Inertial clustering of particles in high-Reynolds-number turbulence. *Physical Review Letters*, 100(21):214501, 2008.
- F. Scarano. Iterative image deformation methods in PIV. *Measurement Science and Technology*, 13(1):1–19, 2002.
- A. Seifert. On the parameterization of evaporation of raindrops as simulated by a one-dimensional rainshaft model. *Journal of the Atmospheric Sciences*, 65(11):3608–3619, 2008.
- A. Seifert and B. Stevens. Microphysical scaling relations in a kinematic model of isolated shallow cumulus clouds. *Journal of the Atmospheric Sciences*, 67(5):1575–1590, 2010.
- S. Seshadhri, R. Bordás, G. Janiga, M. Skalej, and D. Thévenin. Experimental validation of numerical simulations on a cerebral aneurysm phantom model. *Medical Engineering and Physics*, 2011. submitted.
- R. A. Shaw. Particle-turbulence interactions in atmospheric clouds. *Annual Review of Fluid Mechanics*, 35:183–227, 2003.
- R. A. Shaw, W. C. Reade, L. R. Collins, and J. Verlinde. Preferential concentration of cloud droplets by turbulence: Effects on the early evolution of cumulus cloud droplet spectra. *Journal of the Atmospheric Sciences*, 55(11):1965–1976, 1998.
- H. Siebert, H. Franke, K. Lehmann, R. Maser, E. Wei Saw, D. Schell, R. A. Shaw, and M. Wendisch. Probing finescale dynamics and microphysics of clouds with helicopter-borne measurements. *Bulletin of the American Meteorological Society*, 87(12):1727–1738, 2006.

- H. Siebert, K. Lehmann, and R. A. Shaw. On the use of hot-wire anemometers for turbulence measurements in clouds. *Journal of Atmospheric and Oceanic Technology*, 24(6):980–993, 2007.
- A. P. Siebesma, C. S. Bretherton, A. Brown, A. Chlond, J. Cuxart, P. G. Duynkerke, H. Jiang, M. Khairoutdinov, D. Lewellen, C.-H. Moeng, E. Sanchez, B. Stevens, and D. E. Stevens. A Large Eddy Simulation intercomparison study of shallow cumulus convection. *Journal of the Atmospheric Sciences*, 60(10):1201–1219, 2003.
- L. Skrbek and S. R. Stalp. On the decay of homogeneous isotropic turbulence. *Physics of Fluids*, 12(8):1997–2019, 2000.
- L. Skrbek, J. J. Niemela, and R. J. Donnelly. Four regimes of decaying grid turbulence in a finite channel. *Physical Review Letters*, 85(14):2973–2976, 2000.
- M. Sommerfeld and H. Qiu. Particle concentration measurements by phase-Doppler anemometry in complex dispersed two-phase flows. *Experiments in Fluids*, 18(3):187–198, 1995.
- K. Sreenivasan, S. Tavoularis, R. Henry, and S. Corrsin. Temperature fluctuations and scales in grid-generated turbulence. *Journal of Fluid Mechanics*, 100:597–621, 1980.
- K. R. Sreenivasan. On the universality of the Kolmogorov constant. *Physics of Fluids*, 7(11):2778–2784, 1995.
- S. R. Stalp, L. Skrbek, and R. J. Donnelly. Decay of grid turbulence in a finite channel. *Physical Review Letters*, 82(24):4831–4834, 1999.
- B. Stevens and A. Seifert. Understanding macrophysical outcomes of microphysical choices in simulations of shallow cumulus convection. *Journal of the Meteorological Society of Japan*, 86A:143–162, 2008.
- G. Sultan, G. Schulte, and K. Bauckhage. PDA-Messungen von Tropfen-größenverteilungen in optisch dichten Sprays. In A. Delgado, F. Werner, B. Ruck, A. Leder, and D. Dopheide, editors, *Lasermethoden in der Strömungsmesstechnik, 8. Fachtagung, GALA*, pages 50/1–50/7, München, 2000. Shaker Verlag.
- S. Sundaram and L. R. Collins. Collision statistics in an isotropic particle-laden turbulent suspension. Part 1. Direct numerical simulations. *Journal of Fluid Mechanics*, 335:75–109, 1997.



- D. Tarlet, C. Bendicks, R. Bordás, B. Wunderlich, D. Thévenin, and B. Michaelis. Coloured tracer particles employed for 3-D Particle Tracking Velocimetry (PTV) in gas flows. In *Imaging Measurement Methods for Flow Analysis*, volume 106, pages 93–102. Springer, 2009.
- D. Tarlet, C. Bendicks, C. Roloff, R. Bordás, B. Wunderlich, B. Michaelis, and D. Thévenin. Gas flow measurements by 3-D Particle Tracking Velocimetry using coloured tracer particles. *Flow, Turbulence and Combustion*, 2010. submitted.
- G. I. Taylor. Statistical theory of turbulence. *Proceedings of the Royal Society of London. Series A, Mathematical and Physical Sciences (1934-1990)*, 151 (873):421–444, 1935.
- C. Tchen. *Mean Values and Correlation Problems Connected with the Motion of Small Particles Suspended in a Turbulent Fluid*. Ph.D. Thesis, University of Delft, 1947.
- H. Tennekes and J. L. Lumley. *A First Course in Turbulence*. MIT Press, 1972.
- I. Tokar', V. Sirenko, and N. Yurchenko. Calculation of droplet condensation. *Journal of Engineering Physics and Thermophysics*, 41(1):691–696, 1981.
- C. Tropea, T. Xu, F. Onofri, G. Géhan, P. Haugen, and M. Stieglmeier. Dual-mode phase-Doppler anemometer. *Particle & Particle Systems Characterization*, 13(2):165–170, 1996.
- C. Tropea, L. Yarin, and J. F. Foss. *Handbook of Experimental Fluid Mechanics*. Springer, 2007.
- O. Vohl, S. K. Mitra, S. C. Wurzler, and H. R. Pruppacher. A wind tunnel study of the effects of turbulence on the growth of cloud drops by collision and coalescence. *Journal of the Atmospheric Sciences*, 56(24):4088–4099, 1999.
- T. H. Von Kármán and C. C. Lin. On the statistical theory of isotropic turbulence. *Selected Papers of CC Lin*, page 142, 1987.
- M. von Smoluchowski. Versuch einer mathematischen Theorie der Koagulationskinetik kolloider Lösungen. *Zeitschrift für physikalische Chemie*, 92: 129–168, 1917.
- G. A. Voth, A. La Porte, A. M. Crawford, J. Alexander, and E. Bodenschatz. Measurement of particle accelerations in fully developed turbulence. *Journal of Fluid Mechanics*, 469:121–160, 2002.

- L.-P. Wang and W. W. Grabowski. The role of air turbulence in warm rain initiation. *Atmospheric Science Letters*, 10:1–8, Jan. 2009.
- Z. Warhaft. Passive scalars in turbulent flows. *Annual Reviews in Fluid Mechanics*, 32(1):203–240, 2000.
- Z. Warhaft. Laboratory studies of droplets in turbulence: towards understanding the formation of clouds. *Fluid Dynamics Research*, 41(1):011201 (20pp), 2009.
- J. Warner. The microstructure of cumulus cloud. Part I. General features of the droplet spectrum. *Journal of the Atmospheric Sciences*, 26(5):1049–1059, 1969.
- C. Willert. Stereoscopic digital particle image velocimetry for application in wind tunnel flows. *Measurement Science and Technology*, 8(12):1465–1479, 1997.
- J. J. E. Williams and R. I. Crane. Particle collision rate in turbulent flow. *International Journal of Multiphase Flow*, 9(4):421–435, 1983.
- K. Witte, B. Wunderlich, N. Betzler, D. Thévenin, R. Bordás, and J. Edelmann-Nusser. Examination of a swimming dummy's flow field by using Laser Doppler Velocimetry. In *The Engineering of Sport 6: Developments for Disciplines*, pages 75–80. Springer, New York, 2006.
- E. Woittiez, H. Jonker, and L. Portela. On the combined effects of turbulence and gravity on droplet collisions in clouds: A numerical study. *Journal of the Atmospheric Sciences*, 66(7):1926–1943, 2009.
- B. Wunderlich, T. Hagemeyer, D. Thévenin, and R. Bordás. LDV signals provide more information than used before. In T. Lajos and J. Vad, editors, *Conference on Modelling Fluid Flow (the 13th International Conference on Fluid Flow Technologies)*, pages 730–735, Budapest, Hungary, 2006.
- B. Wunderlich, R. Bordás, S. Seshadri, T. Bölke, D. Thévenin, and M. Skalej. LDA-Messungen in Blutgefäßen mittels Brechungsindex-Anpassung. In A. Leder, M. Brede, F. Hüttmann, B. Ruck, and D. Doppeide, editors, *15. Fachtagung "Lasermethoden in der Strömungsmesstechnik" GALA*, pages 47/1–47/7, Rostock, Germany, 2007.
- B. Wunderlich, R. Bordás, D. Thévenin, and M. Dues. Verfahren zur Bestimmung der Geschwindigkeit und der Größe von Teilchen mittels einer für die Laser-Doppler-Velocimetrie geeigneten Anordnung, 2009. Patent.

- T. Xu, F. Durst, and C. Tropea. The three-parameter log-hyperbolic distribution and its application to particle sizing. *Journal of Porous Media*, 11(4):109–124, 2008.
- Y. Xue, L. P. Wang, and W. W. Grabowski. Growth of cloud droplets by turbulent collision-coalescence. *Journal of the Atmospheric Sciences*, 65(2):331–356, 2008.
- S. Yuu. Collision rate of small particles in a homogeneous and isotropic turbulence. *AIChE Journal*, 30(5):802–807, 1984.
- T. Zhou, R. A. Antonia, L. Danaila, and F. Anselmet. Transport equations for the mean energy and temperature dissipation rates in grid turbulence. *Experiments in Fluids*, 28(2):143–151, 2000.



## Róbert Bordás

---

PERSONAL DATA	Date of birth:	27/01/1981
	Place of birth:	Miskolc (Hungary)
	Citizenship:	Hungarian
	Marital status:	Married, 2 children
RESEARCH INTERESTS	Optical measurements, data acquisition and post-processing in turbulent flows, especially the application to two-phase flows.	
EDUCATION	08/2005 - present <b>University of Magdeburg “Otto von Guericke”, Germany</b> PH.D. DEGREE in Technical Sciences, anticipated 2011 THESIS TOPIC: “Optical measurements in disperse two-phase flows: application to rain formation in cumulus clouds” 09/2000 - 06/2005 <b>Budapest University of Technology and Economics, Hungary</b> DIPLOMA DEGREE in Mechanical Engineering, 2005 THESIS TOPIC: “Separate LDV measurements of simultaneously existing tracer particles and air bubbles in a water flow”	
WORK EXPERIENCE	08/2005 - 01/2006 <b>University of Magdeburg “Otto von Guericke”, Germany</b> PRO3 SCHOLARSHIP “Optical measurements in two-phase flows involving particles and emulsions” 01/2006 - 10/2007 <b>University of Magdeburg “Otto von Guericke”, Germany</b> RESEARCH ASSISTANT “Measurement of section detachments by means of improved Particle Tracking Velocimetry (PTV) using colored tracer particles and developed prediction methods”, part of the priority programme DFG 1147. 10/2007 - present <b>University of Magdeburg “Otto von Guericke”, Germany</b> RESEARCH ASSISTANT “Reference experiments in the multiphase wind tunnel, numerical simulation and validation”, part of the priority programme DFG 1276, “MetStröm”.	
TEACHING EXPERIENCE	<b>Supervision of various B.Sc./M.Sc theses</b> in the field of application of optical measurement techniques in the fluid dynamics. <b>Measurement Technology, lecture:</b> LabView, Constant Temperature Anemometry, Data acquisition, Signal processing. <b>Measurement Technology, supervision of laboratory:</b> Constant Temperature Anemometry, pressure measurements	

## Own publications

---

- JOURNAL PUBLICATIONS
- Bendicks, C., Tarlet, D., Roloff, C., Bordás, R., Wunderlich, B., Michaelis, B., and Thévenin, D. Improved 3-D Particle Tracking Velocimetry with Colored Particles. *Journal of Signal and Information Processing*, 2011 in press.
- Bordás, R., Hagemeyer, T., Wunderlich, B. and Thévenin, D. Droplet collisions and interaction with the turbulent flow within a two-phase wind tunnel. *Physics of Fluids*, 2011 accepted for publication.
- Bordás, R., John, V., Schmeier, E. and Thévenin, D. Measurement and simulation of a droplet population in a turbulent flow field. *Computers and Fluids*, (2011) submitted.
- Seshadhri, S., Bordás, R., Janiga, G., Skalej, M. and Thévenin, D. Experimental validation of numerical simulations on a cerebral aneurysm phantom model. *Medical Engineering and Physics*, (2011) submitted.
- Baranyi, L., Szabó, Sz., Bolló, B. and Bordás, R. Analysis of flow around a heated circular cylinder. *Journal of Mechanical Science and Technology*, **23**, 1829–1834, 2010.
- Öncül, A., Bordás, R., Thévenin, D., Genzel, Y., and Reichl, U. CFD-Modellierung der Zellkultivierung in Wave-Bioreaktoren. *Chemie Ingenieur Technik*, **82(9)**, 1512-1513, 2010.
- Kalmbach, A., Bordás, R., Öncül, A.A., Thévenin, D., Genzel, Y., and Reichl, U. Experimental characterization of flow conditions in 2 L and 20 L bioreactors with wave-induced motion. *Biotechnology Progress*, (2010) in press.
- Tarlet, D., Bendicks, C., Roloff, C., Bordás, R., Wunderlich, B., Michaelis, B. and Thévenin, D. Gas flow measurements by 3-D Particle Tracking Velocimetry using coloured tracer particles. *Flow, Turbulence and Combustion*, (2010) submitted.
- Wunderlich, B., Bordás, R., Thévenin, D. and Dues, M. Verfahren zur Bestimmung der Geschwindigkeit und der Größe von Teilchen mittels einer für die Laser-Doppler-Velocimetrie geeigneten Anordnung. *Patent No. 10 2007 052 795 2-52*, 2009.
- PROCEEDINGS AND CONFERENCE PUBLICATIONS
- Bencs, P., Szabó, S., Bordás, R., Zähringer, K. and Thévenin, D.: Simultaneous measurement of velocity and temperature downstream of a heated cylinder. In: *ASME Pressure Vessels & Piping Conference*, Baltimore, Maryland, PVP2011-57789, 1-6, 2011.
- Bordás, R., Hagemeyer, T. and Thévenin, D.: Experimental quantification of droplet collision rates in turbulent sprays. In: *7th International Symposium on Turbulence and Shear Flow Phenomena*, Ottawa, Canada, accepted for presentation, 2011.
- Bordás, R., Hagemeyer, T. and Thévenin, D.: Experimental investigation of droplet-droplet interactions. In: *ILASS2010, 23rd Annual Conference on Liquid Atomization and Spray Systems*, Brno, Czech Republic, 198.1-6, 2010.

- Bencs, P., Szabó, S., Bordás, R., Thévenin, D., Zähringer, K. and Wunderlich, B.: Investigation of the velocity (PIV) and temperature field (BOS) of a heated cylinder in a low Re-number flow. In: *14th International Symposium on Flow Visualization, Daegu, Korea*, 1-8, 2010.
- Mátrai, Z., Bordás, R., Janiga, G. and Thévenin, D.: Laser-Doppler-Velocimetry measurements in artificial medical models. In: *microCAD'10 International Scientific Conference*, (Bikfalvi, P., Ed.), Miskolc, Hungary, ISBN 978-963-661-910-7, 45-50, 2010.
- Öncül, A., Bordás, R., Thévenin, D., Genzel, Y. and Reichl, U.: CFD modeling and validation of cell cultivation in wave bioreactors. In: *28. DECHEMA-Jahrestagung der Biotechnologen*, paper 5042, Aachen, Germany, 2010.
- Bordás, R. and Thévenin, D.: Modeling cumulus clouds in a two-phase wind tunnel. In: *European Geosciences Union General Assembly EGU*, Vienna, Austria, poster session, 2009.
- Bencs, P., Bordás, R., Zähringer, K., Szabó, S. and Thévenin, D.: Towards the application of a Schlieren measurement technique in a wind-tunnel. In: *microCAD'09 International Scientific Conference*, (Lehoczky, L., and Kalmár, L., Eds.), Miskolc, Hungary, ISBN 978-963-661-866-7, 13-20, 2009.
- Bordás, R., Hanke, K., Bencs, P. and Thévenin, D.: 2D-PIV measurements in a two-phase wind-tunnel normal to the main flow. In: *microCAD'09 International Scientific Conference*, (Lehoczky, L., and Kalmár, L., Eds.), Miskolc, Hungary, ISBN 978-963-661-866-7, 39-46, 2009.
- Pap, E., Janiga, G. and Bordás, R.: Möglichkeiten zur rechnerischen Korrektur der optischen Abbildungsverzerrungen bei PIV. In: *microCAD'09 International Scientific Conference*, (Lehoczky, L., and Kalmár, L., Eds.), Miskolc, Hungary, ISBN 978-963-661-866-7, 77-86, 2009.
- Tarlet, D., Bendicks, C., Bordás, R., Wunderlich, B., Thévenin, D. and Michaelis, B.: Mesures par "Particle Tracking Velocimetry" (3-D PTV) gazeuse avec traceurs multicolores. In: *13ème Congrès Français de Visualisation et de Traitement d'Images en Mécanique des Fluides*, (Polidori, G. and Smigielski, P., Eds.), Reims, France, ISBN 978-2-918241-01-0, 1-8, 2009.
- Tarlet, D., Bendicks, C., Bordás, R., Wunderlich, B., Thévenin, D. and Michaelis, B.: Coloured tracer particles employed for 3-D Particle Tracking Velocimetry (PTV) in gas flows, in *Imaging measurement methods for flow analysis*, (Nitsche, W. and Dobriloff, C., Eds.), Notes on Numerical Fluid Mechanics and Multidisciplinary Design, Vol. 106, Springer, 93-102 (2009).
- Tarlet, D., Bendicks, C., Bordás, R., Wunderlich, B., Thévenin, D. and Michaelis, B.: 3-D Particle Tracking Velocimetry (PTV) in gas flows using coloured tracer particles, in *Advances in Turbulence XII*, (Eckhardt, B., Ed.), Springer Proceedings in Physics 132, 43-46 (2009).
- Bolló, B., Baranyi, L., Bordás, R., Tolvaj, B., Bencs, P., Daróczy, L. and Szabó, S.: Numerical and experimental investigation of momentum and

- heat transfer from a heated circular cylinder. In: *microCAD'08 International Scientific Conference*, (Lehoczky, L., and Kalmár, L., Eds.), Miskolc, Hungary, ISBN 978-963-661-816-2, 1-8, 2008.
- Hagemeier, T., Bordás, R. and Janiga, G.: Numerical modeling of aerodynamics around a half cylinder. In: *microCAD'08 International Scientific Conference*, (Lehoczky, L., and Kalmár, L., Eds.), Miskolc, Hungary, ISBN 978-963-661-816-2, 9-14, 2008.
- Seshadhri, S., Janiga, G., Bordás, R., Preim, B., Rose, G., Skalej, M. and Thévenin, D.: Internal flow dynamics of aneurysms: validation of numerical simulations and impact of stent. In: *EUROMECH Fluid Mechanics Conference EFMCF*, Manchester, U.K., 302, 2008.
- Bordás, R., Bendicks, C., Kuhn, R., Wunderlich, B., Thévenin, D. and Michaelis, B.: Coloured tracer particles employed for 3D-PTV in gas flows. In: *13th International Symposium on Flow Visualization*, (Prenel, J.P. and Bailly, Y., Eds.), Nice, France, 093/1-12, 2008.
- Hagemeier, T., Bordás, R., Bencs, P., Wunderlich, B. and Thévenin, D.: Determination of droplet size and velocity distributions in a two-phase wind tunnel. In: *13th International Symposium on Flow Visualization*, (Prenel, J.P. and Bailly, Y., Eds.), Nice, France, 094/1-10, 2008.
- Bordás, R., Fellegi, G., Wunderlich, B., Kuhn, R., Thévenin, D. and Michaelis, B.: Appropriate tracers to measure velocities in particle-laden gas flows using optical techniques. In: *International Conference on Multiphase Flow*, (Sommerfeld, M., Ed.), Leipzig, Germany, B66/1-7, 2007.
- Bordás, R. and Janiga, G.: Numerical simulation of flow instabilities in an axial-flow compressor. In: *microCAD'07 International Scientific Conference*, (Lehoczky, L. and Kalmár, L., Eds.), Miskolc, Hungary, ISBN 978-963-661-746-2, 21-28, 2007.
- Janiga, G., Seshadhri, S., Bordás, R., Bade, R., Preim, B., Bölke, T., Gürvit, Ö., Skalej, M. and Thévenin, D.: Experimental validation of CFD results in the model of an artificial aortic aneurysm. In: *ANSYS Conference*, Dresden, Germany, 2.2.8, 2007.
- Wunderlich, B., Bordás, R., Santhosh, S., Bölke, T., Thévenin, D. and Skalej, M.: LDA-Messungen in Blutgefäßen mittels Brechungsindexanpassung. In: *Lasermethoden in der Strömungsmesstechnik*, (Leder, A., Brede, M., Hüttmann, F., Ruck, B. and Dopheide, D., Eds.), Rostock, Germany, GALA, 47/1-7, 2007.
- Kuhn, R., Bordás, R., Wunderlich, B., Michaelis, B. and Thévenin, D.: Colour class identification of tracers using artificial neural networks. In: *10th International Conference on Engineering Applications of Neural Networks*, Thessaloniki, Greece, 13/2/1-8, 2007.
- Wunderlich, B., Bordás, R., Thévenin, D., Michaelis, B. and Kuhn, R.: Suitable tracer particles for optical velocity measurements in gas flows. In: *8th International Conference on Optical Particle Characterization*, Graz, Austria, poster session, 2007.



- Bordás, R., Kuhn, R., Michaelis, B., Thévenin, D. and Wunderlich, B.: Towards the investigation of vortex structures in gas flows with 3D-highspeed Particle Tracking using coloured tracers. In: *12th International Symposium on Flow Visualization*, (Kompenhans, G. and Schröder, A., Eds), Göttingen, Germany, ISBN 0-9533991-8-4, 251/1-9, 2006.
- Bordás, R., Hagemeyer, T., Thévenin, D. and Wunderlich, B.: LDV-Signale beinhalten mehr Informationen als nur die Geschwindigkeit. In: *Lasermethoden in der Strömungsmesstechnik*, (Dopheide, D., Müller, H., Strunck, V., Ruck, B. and Leder, A., Eds.), Braunschweig, Germany, GALA , ISBN 3-9805613-3-X, 23/1-23/7, 2006.
- Bordás, R., Öncül, A., Zähringer, K. and Thévenin, D.: Optical measurements in two-phase flows involving particles. In: *12th International Symposium on Flow Visualization*, (Kompenhans, G. and Schröder, A., Eds), Göttingen, Germany, ISBN 0-9533991-8-4, 025/1-10, 2006.